Mon. Not. R. Astron. Soc. **319**, 902–932 (2000)

Deformations of accreting neutron star crusts and gravitational wave emission

Greg Ushomirsky,[1★†] Curt Cutler[2★] and Lars Bildsten[3★]

[1]*Department of Physics and Department of Astronomy, 601 Campbell Hall, University of California, Berkeley, CA 94720, USA*
[2]*Max-Planck-Institut für Gravitationsphysik, Albert-Einstein-Institut, Am Muehlenberg 1, D-14476 Golm bei Potsdam, Germany*
[3]*Institute for Theoretical Physics and Department of Physics, Kohn Hall, University of California, Santa Barbara, CA 93106, USA*

Accepted 2000 July 25. Received 2000 June 7; in original form 2000 January 4

ABSTRACT

Motivated by the remarkably narrow range of measured spin frequencies of ~20 accreting (and weakly magnetic) neutron stars in the Galaxy, Bildsten conjectured that their spin-up had been halted by the emission of gravitational waves. If so, then the brightest persistent X-ray source on the sky, Scorpius X-1, should be detected by gravitational wave interferometers within 10 years. Bildsten pointed out that small non-axisymmetric temperature variations in the accreted crust will lead to 'wavy' electron capture layers, and the resulting horizontal density variations near e^- capture layers create a mass quadrupole moment. Neglecting the elastic response of the crust, Bildsten estimated that even e^- capture layers in the thin outer crust can develop the quadrupole necessary to balance accretion torque with gravitational waves, $Q_{22} \sim 10^{37}$–$10^{38}\,\mathrm{g\,cm^{-2}}$ for accretion rates $\dot{M} \sim 10^{-10}$–$2\times10^{-8}\,\mathrm{M_\odot\,yr^{-1}}$.

We present a full calculation of the crust's elastic adjustment to the density perturbations induced by the temperature-sensitive e^- capture reactions. We find that, due to the tendency of the denser material to sink rather than spread sideways, neglecting the elastic response of the crust overestimates, by a factor of 20–50, the Q_{22} that results from a wavy capture layer in the thin outer crust. However, we find that this basic picture, when applied to capture layers in the deep inner crust, can still generate Q_{22} in the necessary range, as long as there are $\lesssim$5 per cent lateral temperature variations at densities in excess of $10^{12}\,\mathrm{g\,cm^{-3}}$, and as long as the crustal breaking strain is high enough. By calculating the thermal flow throughout the core and the crust, we find that temperature gradients this large are easily maintained by asymmetric heat sources or lateral composition gradients in the crust. If the composition or heating asymmetries are independent of the accretion rate, then for $\dot{M} \lesssim 5\times10^{-9}\,\mathrm{M_\odot\,yr^{-1}}$ the induced quadrupole moments have approximately the same scaling, $\propto\dot{M}^{1/2}$, as that necessary to balance the accretion torque at the same spin frequency for all $\dot{M}$. Temperature gradients in the deep crust lead to a modulation in the thermal emission from the surface of the star that is correlated with Q_{22}. In addition, a ~0.5 per cent lateral variation in the nuclear charge-to-mass ratio in the crust will also result in a Q_{22} sufficient to halt spin-up from accretion even in the absence of a lateral temperature gradient.

We also derive a general relation between the stresses and strains in the crust and the maximum quadrupole moment they can generate. We show, under quite general conditions, that maintaining a Q_{22} of the magnitude necessary to balance the accretion torque requires a dimensionless strain $\sigma \sim 10^{-2}$ at near-Eddington accretion rates, of order the breaking strain of conventional materials. This leads us to speculate that accreting neutron stars reach the same equilibrium spin because they all are driven to the maximum Q_{22} that the crust can sustain.

Key words: accretion, accretion discs – dense matter – radiation mechanisms: non-thermal – stars: neutron – stars: rotation.

★ E-mail: gregus@tapir.caltech.edu (GU); cutler@aei-potsdam.mpg.de (CC); bildsten@itp.ucsb.edu (LB)
† Present address: Theoretical Astrophysics, Mail Code 130-33, California Institute of Technology, Pasadena, CA 91125, USA.

© 2000 RAS

Downloaded from https://academic.oup.com/mnras/article-abstract/319/3/902/1075833 by California Institute of Technology user on 19 May 2020

1 INTRODUCTION

Recent discoveries by the *Rossi X-Ray Timing Explorer* indicate that most of the rapidly accreting ($\dot{M} \gtrsim 10^{-11}\,\mathrm{M_\odot\,yr^{-1}}$) and weakly magnetic ($B \ll 10^{11}$ G) neutron stars in our Galaxy are rotating in a narrow range of frequencies around $\nu_s \approx 300$ Hz (van der Klis 1998). From both evolutionary considerations and their Galactic distribution, we know that the neutron stars in these low-mass X-ray binaries (LMXBs) are relatively old systems (see Bhattacharya & van den Heuvel 1991) that have accreted enough angular momentum to reach rotation rates closer to the breakup frequency of ≈1.5 kHz. Hence, some mechanism must be found to halt the spin-up. One possible explanation is that the neutron stars have reached the magnetic spin equilibrium (where the spin frequency matches the Keplerian frequency at the magnetosphere) at nearly identical spin frequencies. This requires that the neutron star's dipolar magnetic field strength correlates very well with $\dot{M}$ (White & Zhang 1997; Miller, Lamb & Psaltis 1998). In an alternate scenario, Bildsten (1998a) suggested that these stars are rotating fast enough so that appreciable angular momentum is radiated away as gravitational waves (GW), allowing an equilibrium where the angular momentum added by accretion is lost to gravitational radiation. Equilibria via gravitational wave emission from rotational instabilities at much more rapid rotation rates had been postulated earlier by Papaloizou & Pringle (1978) and Wagoner (1984).

The angular momentum loss rate from quadrupolar GW emission scales as ν_s^5, so that gravitational radiation effectively provides a 'wall' beyond which accretion can no longer spin the star up. Bildsten (1998a) estimated that 'wavy' electron capture layers in the neutron star's crust, caused by a large-scale temperature asymmetry misaligned from the spin axis, can provide the quadrupole needed ($Q_{22} \sim 2\times10^{38}\,\mathrm{g\,cm^2}$ at the Eddington accretion rate, $\dot{M}_{\rm Edd} \equiv 2\times10^{-8}\,\mathrm{M_\odot\,yr^{-1}}$) to reach this limiting situation at $\nu_s \approx 300$ Hz. Another possibility is GW emission from a continuously excited r-mode (i.e., a Rossby wave) in the neutron star core (Bildsten 1998a; Andersson, Kokkotas & Stergioulas 1999), although Levin (1999) has shown that such steady-state r-mode can potentially be thermally unstable. More recently, Brown & Ushomirsky (2000) have shown that *steady-state* equilibrium between the accretion torque and r-mode gravitational wave emission is incompatible with observations of the quiescent luminosities of neutron star transients. Finally, Bildsten & Ushomirsky (2000) have shown that the dissipation due to a viscous boundary layer between the crust and the core is many orders of magnitude stronger that the viscous mechanisms previously considered, but Levin & Ushomirsky (2000) recently demonstrated that the smallness of the crust's shear modulus makes this damping less effective and complicates the picture for excitation of r-modes accreting neutron stars. We will not consider the r-mode hypothesis further here, but will instead concentrate on a self-consistent calculation of the mass quadrupole moment generated in the crust.

1.1 Equilibrium quadrupolar gravitational wave emission

We start by calculating the quadrupole moment that the neutron star (NS) must have so that the spin-up torque from accretion, N_a, is balanced by emission of quadrupolar gravitational radiation. Consider an NS that is perturbed from sphericity by a density perturbation $\delta\rho \equiv \mathrm{Re}\{\delta\rho_{lm}(r)Y_{lm}(\theta,\phi)\}$. Let Q_{lm} be the perturbation's multipole moment, defined by

$$Q_{lm} \equiv \int \delta\rho_{lm}(r) r^{l+2}\,\mathrm{d}r. \tag{1}$$

We concentrate on perturbations Q_{22} with $l=m=2$; these perturbations radiate at a frequency $\nu_{\rm gw} = 2\nu_s$. The resulting rate of loss of angular momentum $N_{\rm gw}$ is

$$N_{\rm gw} = \frac{\dot{E}_{\rm gw}}{\Omega} = \frac{G}{c^5}\frac{1}{5\Omega}\langle \dddot{I}_{ab}\ddot{I}^{ab}\rangle, \tag{2}$$

where $I_{ab} \equiv \int \delta\rho r_a r_b\,\mathrm{d}^3V$, $\Omega = 2\pi\nu_s$, and '$\langle\ldots\rangle$' means 'time-averaged over one period.' A little algebra shows that $\langle \dddot{I}_{ab}\ddot{I}^{ab}\rangle = (256\pi/15)\,\Omega^6 Q_{22}^2$, so equation (2) becomes

$$N_{\rm gw} = \frac{256\pi}{75}\frac{G\Omega^5 Q_{22}^2}{c^5}. \tag{3}$$

For simplicity, we assume that the accreted angular momentum is that of particles arriving from the inner edge of the accretion disc (placed at the NS radius), so that $N_a = \dot{M}(GMR)^{1/2}$, where M and R are the mass and radius of the NS. The required quadrupole moment $Q_{\rm eq}$ such that gravitational wave emission is in equilibrium with the accretion torque, N_a, is then

$$Q_{\rm eq} = 3.5\times10^{37}\,\mathrm{g\,cm^2}\,M_{1.4}^{1/4}R_6^{1/4} \times\left(\frac{\dot{M}}{10^{-9}\,\mathrm{M_\odot\,yr^{-1}}}\right)^{1/2}\left(\frac{300\,\mathrm{Hz}}{\nu_s}\right)^{5/2}, \tag{4}$$

where $M_{1.4} = M/1.4\,\mathrm{M_\odot}$ and $R_6 = R/10\,\mathrm{km}$. The range of $\dot{M}$s typically encountered in the LMXBs is 10^{-10}–$2\times10^{-8}\,\mathrm{M_\odot\,yr^{-1}}$, requiring $Q_{22} \approx 10^{37}$–$10^{38}\,\mathrm{g\,cm^2}$ for $\nu_s = 300$ Hz (Bildsten 1998a).

This paper is devoted to learning whether such a large quadrupole can be generated from deformed capture layers in the crust (Bildsten 1998a), and to finding the magnitude and distribution of the elastic strain required to sustain it. We answer the latter question in some detail in Section 6, where we show that Q_{22} is related to the typical strain, $\bar{\sigma}$, via

$$Q_{22} \approx 1.2\times10^{38}\,\mathrm{g\,cm^2}\left(\frac{\bar{\sigma}}{10^{-2}}\right)\frac{R_6^{6.3}}{M_{1.4}^{1.2}}. \tag{5}$$

A more complete version of this relation that includes the dependences on the density at the crust–core transition and the composition of the crust is given in equation (69). If we presume that the crust is pushed to some yielding strain $\bar{\sigma}_{\rm max}$ by the physical effects calculated here, we find

$$\nu_{s,\rm eq} \approx 295\,\mathrm{Hz}\left(\frac{10^{-2}}{\bar{\sigma}_{\rm max}}\right)^{2/5}\frac{M_{1.4}^{0.6}}{R_6^{2.4}}\left(\frac{\dot{M}}{10^{-8}\,\mathrm{M_\odot\,yr^{-1}}}\right)^{1/5}, \tag{6}$$

a rather suggestive relation that points to a possible answer as to why so many LMXBs are in a narrow spin frequency range, namely that accretion always drives the crustal strain to the breaking point.

Before we launch into the detailed discussion of how the crust is stressed and how it responds, we calculate the strength of the GW signal from such an equilibrium radiator. Consider an NS at a distance d with an energy flux in gravitational waves, $\dot{E}_{\rm gw}$, but with an unknown spin orientation to the observer. We define the source's 'angle-averaged' field strength h_a (at Earth) by

$$h_a^2 \equiv \frac{1}{4\pi}\int (h_+^2 + h_\times^2)\,\mathrm{d}\Omega, \tag{7}$$

where the integral is over source orientations.[1] The standard formula for the effective stress-energy of gravitational waves

[1] A common measure of GW source strength is the characteristic amplitude h_c. It is related to h_a by $h_c \approx 1.15 h_a$.

Downloaded from https://academic.oup.com/mnras/article-abstract/319/3/902/1075833 by California Institute of Technology user on 19 May 2020

yields

$$N_{\rm gw} = \frac{c^3 \Omega d^2 h_a^2}{G}, \tag{8}$$

which, when we write it in terms of Q_{22} (using equation 3) gives

$$h_{\rm a} = \frac{16}{5}\left(\frac{\pi}{3}\right)^{1/2} \frac{G Q_{22} \Omega^2}{d c^4}. \tag{9}$$

When the angular momentum loss by gravitational radiation balances angular momentum gain by accretion,

$$h_{\rm a} = 3.5 \times 10^{-27} \frac{R_6^{3/4}}{M_{1.4}^{1/4}} \left(\frac{300\,{\rm Hz}}{\nu_{\rm s}}\right)^{1/2} \left(\frac{F_{\rm x}}{10^{-8}\,{\rm erg\,cm^{-2}\,s^{-1}}}\right)^{1/2} \tag{10}$$

(Wagoner 1984; Bildsten 1998a). Here we have replaced $\dot{M}$ and d with the observed X-ray flux, $F_{\rm x} = G\dot{M}M/4\pi R d^2$. The gravitational wave strength for an NS accreting at the Eddington limit at the Galactic Centre is then $h_{\rm a} \approx 5 \times 10^{-27}$. Prior accurate knowledge of the position on the sky and orbital periods of many of these X-ray binaries will allow for deep searches with the suite of laser-interferometric gravitational wave detectors currently under construction (LIGO, VIRGO, GEO-600 and TAMA-300; see Brady et al. 1998 and Brady & Creighton 2000). The nearby source Scorpius X-1 is the obvious first target. Its X-ray flux is $F_{\rm x} \approx 2 \times 10^{-7}\,{\rm erg\,cm^{-2}\,s^{-1}}$ and the spin period is still unknown, but probably in the range of 300 Hz (van der Klis 1998), giving $h_{\rm a} \approx 1.6 \times 10^{-26}$. Bradshaw, Fomalont & Geldzahler (1999) recently determined that Sco X-1 is at a distance $d = 2.8 \pm 0.3$ kpc, giving a luminosity close to the Eddington value for cosmic abundances, $2 \times 10^{38}\,{\rm erg\,s^{-1}}$, and implying $\dot{M} \approx 2 \times 10^{-8}\,{\rm M_\odot\,yr^{-1}}$ and a required quadrupole $Q_{22} \approx 1.6 \times 10^{38}\,{\rm g\,cm^2}\ (300\,{\rm Hz}/\nu_{\rm s})^{5/2}$ for equilibrium GW emission.

1.2 Origin of the crustal quadrupole moment

The crust of an NS is a thin ($\approx$1 km) layer of crystalline 'ordinary' (albeit neutron-rich) matter that overlies the liquid core composed of neutrons, protons and electrons (see Fig. 1). The composition of the crust, i.e., the mass number A and the charge Z of the nuclei, varies with depth. As an accreted nucleus gets buried under an increasingly thick layer of more recently accreted material, it undergoes a series of nuclear reactions, including electron captures, neutron emissions, and pycnonuclear reactions (Sato 1979; Blaes et al. 1990; Haensel & Zdunik 1990b). The crust therefore consists of layers of different nuclear composition, as indicated schematically in Fig. 1.

Essentially all the pressure in the outer crust, and an appreciable fraction of the pressure in the inner crust, is supplied by degenerate relativistic electrons. The pressure must be continuous across the boundaries of the compositional layers. However, electron-capture reactions reduce the number of electrons per nucleon, and hence require density jumps between the compositional layers depicted in Fig. 1. In the outer crust, these density jumps are as large as $\approx$10 per cent, while in the inner crust the density contrast is smaller, $\lesssim$1 per cent.

Bildsten & Cumming (1998) showed that at the typical crustal temperatures of accreting neutron stars, $\gtrsim 2 \times 10^8$ K, the electron-capture rates are sensitive to the local temperature (see discussion in Section 2.1). In this case, regions of the crust that are hotter undergo electron-capture transitions at a lower density (and thus

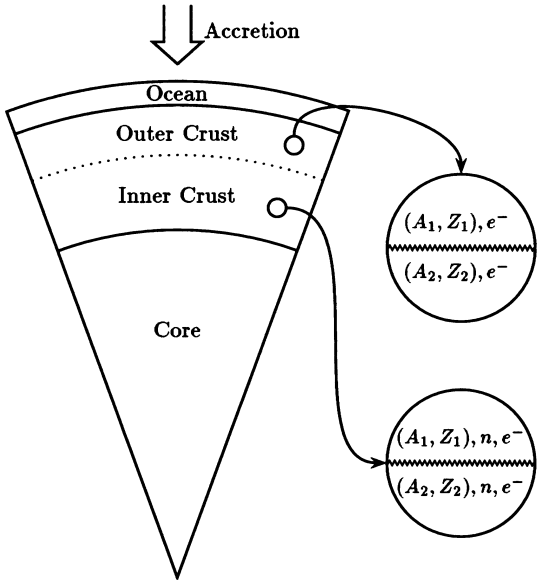

Figure 1. The schematic structure of the neutron star, displaying the inner and outer crust lying on the liquid core. The ocean on top of the crust ends when the material is dense enough to crystallize. The outer crust consists of nuclei in a lattice and a background of degenerate, relativistic electrons, whereas the inner crust [at densities $\gtrsim (4\text{–}6) \times 10^{11}\,{\rm g\,cm^{-3}}$] has free neutrons in addition to the nuclear lattice.

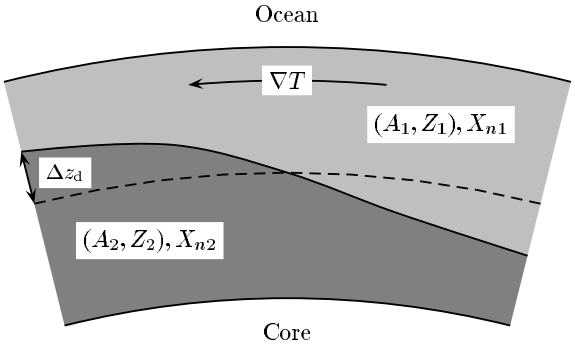

Figure 2. A cartoon description of how a transverse temperature gradient in the crust will lead to a varying altitude for the electron captures. The dashed line denotes the unperturbed location of the e^- capture boundary between the layer of material composed of nuclei (A_1, Z_1), a mass fraction $X_{\rm n1}$ of free neutrons, and free electrons, and a layer with nuclei (A_2, Z_2), $X_{\rm n2}$ fraction of free neutrons, and free electrons. When a lateral temperature gradient ∇T is introduced, the capture boundary shifts to a new location shown by the solid line. Note that this cartoon presumes that the crust is infinitely rigid and therefore does not adjust elastically to the shift $\Delta z_{\rm d}$ of the capture boundary.

larger radius) than the colder regions. This effect is illustrated schematically in Fig. 2, which shows a patch of the crust near a capture layer where nucleus (A_1, Z_1) is transformed into (A_2, Z_2). If there is no lateral temperature gradient, then the capture layer is spherically symmetric, as indicated by the dashed line. The lateral temperature gradient (shown by the arrow) induces some extra captures on the left (hotter) side, and reverses some captures on the right (cooler) side. If the lateral temperature contrast is δT, then e^- captures on the hot side of the star happen at the Fermi energy that is roughly $\Upsilon k_{\rm B} \delta T$ lower, and captures on the cold side proceed at the Fermi energy about $\Upsilon k_{\rm B} \delta T$ higher than in the unperturbed case (Bildsten 1998a). Typical values of Υ are 10–20

Downloaded from https://academic.oup.com/mnras/article-abstract/319/3/902/1075833 by California Institute of Technology user on 19 May 2020

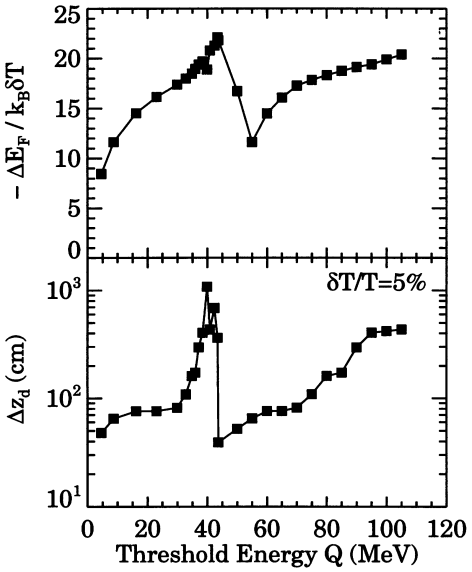

Figure 3. Top: Sensitivity $\Upsilon = -\Delta E_F/k_B\delta T$ of the location of e^- capture layers to local temperature perturbations as a function of the capture layer threshold Q. Bottom: Vertical shift of a capture layer Δz_d for a fiducial temperature perturbation $\delta T/T = 0.05$, disallowing elastic readjustment of the crust, plotted as function of the capture layer threshold energy Q. These plots are generated using the formalism described in Appendix A (see equations A18 and A20). The complicated dependence of Δz_d and Υ on the capture layer depth stems from the differences in the number of electrons captured and number of neutrons emitted in each capture layer.

(see the top panel in Fig. 3). Since the Fermi energy increases with depth, captures occur a distance Δz_d higher in the crust on the hot side, and a distance Δz_d lower on the cold side. The resulting capture layer is indicated by the solid line in Fig. 2.

Therefore, a large-scale temperature asymmetry deforms the capture layers. Such a temperature gradient, if misaligned from the spin axis, will give rise to a non-axisymmetric density variation and a non-zero quadrupole moment Q_{22} *even if the composition of the crust has no lateral variation.* Of course, a lateral composition gradient in the NS crust can exist without a temperature gradient, and would also create a quadrupole moment.

On dimensional grounds, the quadrupole moment generated by a temperature-dependent capture boundary is $Q_{22} \sim Q_{\rm fid} \equiv \Delta\rho\Delta z_d R^4$, where $\Delta\rho$ is the density jump at the electron capture interface. This fiducial value, $Q_{\rm fid}$, is the quadrupole moment that would result if crustal matter just moved horizontally to regain horizontal pressure balance. Using this estimate, Bildsten (1998a) argued that a single wavy capture boundary in the outer crust could generate Q_{22} sufficient to buffer the spin-up due to accretion, provided that temperature variations of $\sim$20 per cent are present in the crust.

However an important piece of physics is missing from this fiducial estimate: the shear modulus of the crust μ. This must be important to the estimate, since if μ vanishes, the crust becomes a liquid and cannot support a non-zero Q_{22}. In addition, an NS crust is thought to have a small shear modulus relative to the pressure, $\mu/p \sim 10^{-2}$–10^{-3} typically. Much of this paper is concerned with improving upon the above fiducial estimate. Treating the crust as an elastic solid, we assume the existence of a horizontal temperature or composition gradient, and then solve for the displacement field that brings the crust into equilibrium, with the gravitational, pressure, and shear-stress forces all in balance. From the density perturbation $\delta\rho$ we calculate Q_{22} for a single electron capture layer and find that it is typically 5–50 times smaller than the fiducial estimate, depending on the capture layer depth (see Section 5.1). Hence, in order to generate a Q_{22} large enough for substantial GW emission, we must include capture layers in the more massive neutron-rich part of the crust.

Before launching into detailed calculations, we now describe why it is plausible to assume that lateral temperature and composition gradients are present in the crusts of accreting neutron stars. We present a detailed model of thermal gradients in the crust in Section 3.

1.3 Possible causes of temperature asymmetries

In LMXBs, accretion will replace the primordial crust after about $\sim 5\times10^7$ yr ($\dot{M}/10^{-9}\,{\rm M}_\odot\,{\rm yr}^{-1}$). This is much shorter than the lifetime of such systems. While it is plausible that the primordial crust is spherically symmetric in composition, we suggest that the accreted crust need not be.

The accreted crust is composed of the compressed products of nuclear burning of the accreted hydrogen and helium in the NS's upper atmosphere. The nuclear mix entering the top of the crust depends sensitively on the burning conditions, and is still not well known. Schatz et al. (1999) showed that the products of *steady-state* burning in the upper atmosphere are a complicated mix of elements far beyond the iron peak. The exact composition (and the average A) depends on the local accretion rate, which could have a significant non-axisymmetric piece in the presence of a weak magnetic field.

However, except in the highest accretion rate LMXBs, nearly all of the nuclear burning occurs in Type I X-ray bursts, sudden consumption of fuel accumulated for hours to days prior to ignition. The rotational modulation observed during type I X-ray bursts in several LMXBs (first detected in 4U 1728 − 34 by Strohmayer et al. 1996; see van der Klis 2000 for a review) provides conclusive evidence that bursts themselves are not axisymmetric. Until the origin of this symmetry breaking is clearly understood, it is plausible to postulate that these burst asymmetries get imprinted into the crustal composition or result from them. Finally, it is possible that there is a feedback mechanism that causes composition asymmetries to grow: lateral composition variations lead to temperature asymmetries (as shown below), which, in turn, affect the burning conditions of the elements entering the crust.

Clearly, it is almost impossible to compute the magnitude of the composition asymmetry from first principles, and we shall not attempt to do so here. Instead, we postulate that such asymmetry exists at some level, and explore its consequences. In particular, we show that a composition asymmetry in the crust will modulate the heat flux through it. Thus, one of our predictions is a relation between the modulation in the persistent thermal emission of accreting neutron stars and their quadrupole moments. In other words, the lateral temperature gradient in the deep crust that generates a Q_{22} sufficient to halt accretional spin-up also gives rise to a certain thermal flux modulation, which we quantify in Sections 3.3 and 5.2.

The consequences of the lateral composition asymmetry of the crust are two-fold. First, different elements have different charge-to-mass ratio, and hence different thermal conductivity and neutrino emissivity, both of which scale as Z^2/A. This lateral variation of the transport properties modulates the heat flux in the

Downloaded from https://academic.oup.com/mnras/article-abstract/319/3/902/1075833 by California Institute of Technology user on 19 May 2020

NS crust, leading to lateral temperature variations δT. Secondly, the nuclear reactions in the deep crust release energy and heat it locally. The heat release is again dependent on the particular element, and hence varies laterally if the crust is compositionally asymmetric, also giving rise to a temperature gradient. We quantify both of these thermal effects in Section 3. In addition to these thermal effects, a composition gradient generates a quadrupole moment directly, because elements with different Z/A have different characteristic electron pressures, and the resulting transverse pressure gradient elastically deforms the crust.

1.4 Outline of the paper

The purpose of this paper is three-fold. In the first part (Sections 2 and 3) we calculate the temperature asymmetry in the crust that can arise from asymmetric conductivities and/or heating. As stressed in Section 1.3, at this point it is just a (testable!) conjecture that there are large-scale temperature asymmetries misaligned with the spin of the neutron star. We show how these can arise due to composition gradients, despite the large thermal conductivity of the core. In Section 2 we discuss the structure of the NS crust; in particular, we extend the work of Bildsten (1998a) and Bildsten & Cumming (1998) on the structure of electron capture layers by considering regions where there is a large density of free neutrons. In Section 3 we calculate the magnitude of the temperature variations induced by the composition variations, through their effect both on the conductivity and on the local heating rate in the crust. We find that 10 per cent lateral variations in the heating rate or conductivity result in $\lesssim$5 per cent temperature asymmetry in the deep crust at accretion rates of order the Eddington rate, and $\lesssim$1 per cent lateral temperature variations at $10^{-2}\dot{M}_{\rm Edd}$.

In the second part of our paper (Sections 4 and 5) we calculate the elastic adjustment of the crust induced by a deformed electron capture layer or a smooth composition gradient, and determine the resulting mass quadrupole moment, Q_{22}. If we consider the Q_{22} generated by a single deformed capture layer in the outer crust (which contains only $\sim 10^{-5}\,{\rm M}_\odot$), we find that Q_{22} is smaller than the fiducial estimate of Bildsten (1998a) by a factor of 20–50. However, deformed capture boundaries in the deep, inner crust *can* generate sufficient Q_{22} to halt the spin-up of neutron stars at 300 Hz, provided there are $\sim$1 per cent lateral temperature variations, and provided the induced strains do not crack the crust. Quadrupole moments due to multiple capture layers add linearly, and hence the required temperature asymmetry is even smaller. Moreover, a smooth 0.5 per cent composition gradient results in a similar quadrupole moment even in the absence of a lateral temperature gradient. Our solutions exhibit typical strains $\sigma \gtrsim 10^{-2}$ at near-Eddington accretion rates, and $\sigma \sim 10^{-3}$ at $10^{-2}\dot{M}_{\rm Edd}$ (see Section 6.3). The former is larger than the breaking strain for terrestrial rocks under atmospheric pressure, but is perhaps possible for highly compressed NS crusts. The level of crustal strain required to sustain the large quadrupole moments is perhaps the most problematic feature of our model.

The third part of this paper (Section 6) is an investigation of the relation between Q_{22} and crustal shear stresses. Specifically, we derive a relation, equation (64), that expresses Q_{22} as an integral over shear stress terms in the crust. Equation (64) holds independent of any detailed model of how those stresses are generated, and it immediately gives us an upper limit on Q_{22} for a given crustal breaking strain. In Section 6.5 we estimate the correction to the results due to the neglect of the gravitational potential perturbation (the Cowling approximation).

Finally, we close in Section 7 with a summary of our efforts, and a discussion of what is still missing from the theoretical picture. Appendix A contains the expressions for evaluating the source terms of the crustal deformation equations, and definitions of all variables used in this paper.

2 STRUCTURE OF THE ACCRETED NS CRUST

Bildsten (1998a) confined his discussion to the outer crust [before neutron drip at $\rho < \rho_{\rm nd} \approx (4\text{–}6)\times 10^{11}\,{\rm g\,cm^{-3}}$; Haensel & Zdunik 1990b], which is held up by relativistic degenerate electrons. However, as we found in the course of our work, the capture layers that produce the largest quadrupole moments are at densities much greater than neutron drip, and so we need to model the entire crust. Our modelling of the thermal structure of the crust and core mostly follows Brown (2000).

The nuclear mix entering the top of the crust is not well known. This mix depends sensitively on the conditions of hydrogen and helium burning in the upper atmosphere. For steady burning, Schatz et al. (1999) showed that the products are a complicated mix of elements far beyond the iron peak. The more relevant case of time-dependent nucleosynthesis in X-ray bursts is still unresolved (Rembges et al. 1997, 1998; Thielemann et al. 1998). What eventually needs to be done is a calculation of the nuclear evolution of these complicated mixes throughout the deep crust. Lacking these inputs, we take for our model of the crustal composition the tabulation given by Haensel & Zdunik (1990a,b). These authors start by assuming that pure iron enters the top of the crust, and that at each pressure the crust is composed of a single nuclear species, with the transitions between species being abrupt. Starting with ^{56}Fe, their calculations produce the sequence of the most energetically favourable nuclei (and the range of densities and pressures for each one) under the constraint that only electron captures, neutron emissions, and pycnonuclear reactions are allowed (i.e., the crust is too cold for a thermal reshuffling of nucleons to occur).

Taking the composition to be pure instead of mixed has a negligible effect on the hydrostatic composition of the crust. However, the composition does have a large effect on the crust's thermal conductivity, K; we use an estimate of K that is appropriate for a lattice of mixed composition (Schatz et al. 1999). Also, while Haensel & Zdunik (1990a,b) approximate the capture transitions as infinitely sharp, we resolve the actual, finite-thickness capture layers by integrating the capture rate equation, following Bildsten & Cumming (1998). We extend their work by including the presence of free neutrons, which allows us to resolve capture layers at $\rho > \rho_{\rm nd}$.

2.1 Temperature sensitivity of electron capture rates

In accreting neutron stars, the nuclear transformations of the crustal material are driven by increasing compression from the weight of the overlying matter. The location and thickness of the reaction layers are determined by the competition between the corresponding reaction rate (at a given ρ and T) and the local compression time-scale, i.e., the rate at which the local conditions are changing. The compression time-scale at a given depth is $t_{\rm comp} = p/\dot{m}g$, where $\dot{m} = \dot{M}/4\pi r^2$ is the local accretion rate, $g = GM_r/r^2$ is the local gravitational acceleration, and p/g is approximately the

Downloaded from https://academic.oup.com/mnras/article-abstract/319/3/902/1075833 by California Institute of Technology user on 19 May 2020

column density, $\int_r^R \rho \, \mathrm{d}r$. This is just the time it takes for the pressure on a fluid element to double due to the extra hydrostatic pressure of new material added at the top.

Consider the transformation of a region of the crust where the predominant nucleus has charge Ze and mass Am_b. (For simplicity, consider a region where $\rho < \rho_\mathrm{nd}$.) As it is compressed, the electron Fermi energy, E_F, rises to the point where an electron capture on the nucleus is energetically allowed. The reaction transforms an element (A, Z) into $(A, Z-1)$. In practice, the mass difference between $(A, Z-1)$ and $(A, Z-2)$ is always greater than that between (A, Z) and $(A, Z-1)$, so the subsequent reaction $(A, Z-1) + \mathrm{e}^- \rightarrow (A, Z-2) + \nu_\mathrm{e}$ is very fast, and typically proceeds immediately (Blaes et al. 1990; Haensel & Zdunik 1990b). The second capture releases of order 1 MeV, making the process effectively irreversible. The two successive electron captures can often be treated as one reaction, with the rate-limiting step being the first capture. At densities greater than neutron drip, the captures are accompanied by neutron emission (typically six neutrons are emitted), and sometimes also by a pycnonuclear reaction.

What is the exact place where the reaction becomes fast enough to compete with compression? At $T = 0$, in order for electron captures to proceed, the fluid element must be compressed until the electron Fermi energy E_F exceeds the threshold energy Q (roughly the mass difference between the e^- capturer and the product; Blaes et al. 1990). Hence, at low T the electron capture rate is not very temperature-sensitive, and the location of the capture layers does not depend on the local temperature. The thickness of the electron capture layers in this case is set by the need to have enough phase-space (determined by $E_\mathrm{F} - Q$) so that the electron captures proceed at a rate comparable to that of the compression (Blaes et al. 1990).

However, Bildsten & Cumming (1998) showed that when the temperature is in excess of 2×10^8 K (conditions typical for crusts of neutron stars in LMXBs), there are enough electrons on the thermal tail of the Fermi–Dirac distribution so that captures can proceed even when $E_\mathrm{F} < Q$. The capture rate R_ec is approximately given by

$$R_\mathrm{ec} = \left(\frac{\ln 2}{ft}\right) \frac{2Q^2 (k_\mathrm{B}T)^3}{(m_\mathrm{e}c^2)^5} \exp\left(\frac{E_\mathrm{F} - Q}{k_\mathrm{B}T}\right) \tag{11}$$

(equations 2 and 5 of Bildsten & Cumming 1998). The ft value is for the first e^- capture transition, and depends on the degree of forbiddenness of the reaction. Typical ft values range anywhere from 10^3 to 10^8 s for the transitions that are relevant. In this paper we use $ft = 10^4$ s for all reactions. As we show below, the dependence of the location of the capture layer on ft is only logarithmic, so even an error of a few orders of magnitude is not important to our work. On the other hand, the sensitivity to the local temperature is exponential, which is why even modest lateral temperature gradients can generate sizeable quadrupole moments.

How does the location of the capture layer change with the local temperature? Most electron captures happen when the lifetime of an element to electron capture, $t_\mathrm{ec} = 1/R_\mathrm{ec}$, becomes comparable to the local compression time-scale t_comp (Bildsten 1998a; Bildsten & Cumming 1998). Pre-threshold captures then proceed at $E_\mathrm{F} \approx Q - \Upsilon k_\mathrm{B}T$ (Bildsten 1998a), where

$$\Upsilon = \ln\left[\frac{p_\mathrm{c}(E_\mathrm{F})}{\dot{m}g} \frac{\ln 2}{ft} \frac{2Q^2 (k_\mathrm{B}T)^3}{(m_\mathrm{e}c^2)^5}\right] \sim 10\text{–}20, \tag{12}$$

depending on the capture layer pressure p_c and other parameters. The procedure for solving this equation is described in Appendix A. The function Υ is plotted in the top panel of Fig. 3.

We define Δz_d to be the distance that the capture layer *would* shift vertically if the crust were absolutely rigid; i.e., if there were no elastic readjustment. Then Δz_d is approximately given by

$$\frac{\Delta z_\mathrm{d}}{h} \approx \Upsilon \frac{\mathrm{d}\ln p}{\mathrm{d}\ln E_\mathrm{F}} \frac{k_\mathrm{B}T}{Q} \frac{\delta T}{T}, \tag{13}$$

where h is the local scale height. At densities lower than neutron drip, $p \propto E_\mathrm{F}^4$, while for $\rho > \rho_\mathrm{nd}$ the dependence of p on E_F is even steeper, as electrons supply only a fraction of the total pressure. This relation is formulated more precisely in Appendix A, and Δz_d for a fiducial 5 per cent temperature perturbation $\delta T/T$ is shown in the bottom panel of Fig. 3.

2.2 Capture layers at densities higher than neutron drip

An exact calculation of the crust's composition would require a reaction network large enough to allow for the possibility of several elements undergoing captures at the same time. This is beyond the scope of our paper. For simplicity, we assume that between the capture layers, the crust is composed of a single species of nucleus (A, Z), electrons, and neutrons (once $\rho > \rho_\mathrm{nd}$). Capture layers, however, contain a mix of elements: a mass fraction X_1 of element (A_1, Z_1) that is abundant above the capture layer (see Fig. 2), a mass fraction X_n of free neutrons, a mass fraction $X_2 = 1 - X_1 - X_\mathrm{n}$ of element (A_2, Z_2) [the end-product of electron captures on to (A_1, Z_1)], and electron density $n_\mathrm{e} = \rho/\mu_\mathrm{e} m_\mathrm{b}$. With this simplification, we need to integrate only one rate equation at a time.

We consider a capture layer, where elements (A_1, Z_1) are transformed into (A_2, Z_2), and, at the top of the layer, where the mass fraction of (A_2, Z_2) is zero, the neutron mass fraction is X_n1. Suppose that the reaction is a simple one, i.e., it consists of capturing $Z_1 - Z_2$ electrons, and emitting $A_1 - A_2$ neutrons. Then, at the bottom of the layer, where the reaction is complete and the mass fraction of (A_1, Z_1) is zero, the mass fraction of free neutrons X_n2 is such that $A_1/(1 - X_\mathrm{n1}) = A_2/(1 - X_\mathrm{n2})$. Similarly, if electron captures and neutron emissions in the layer are accompanied by a pycnonuclear reaction [i.e., fusing of two nuclei (A, Z) into a single $(2A, 2Z)$ nucleus], then simple bookkeeping shows that $A_1/(1 - X_\mathrm{n1}) = (1/2)A_2/(1 - X_\mathrm{n2})$.

Now consider some point in the capture layer where both reactants (A_1, Z_1) and products (A_2, Z_2) are present. In practice, neutron emissions are triggered by electron captures, and the time-scale for neutron emission is always much shorter than the electron capture time-scale (Sato 1979; Haensel & Zdunik 1990b). We therefore assume that these steps proceed simultaneously, so the proportion of neutrons per nucleus of each type stays fixed; e.g., if only $(Z_1 - Z_2)/2$ electrons have been captured, then exactly $(A_1 - A_2)/2$ neutrons have been emitted. This gives

$$X_\mathrm{n} = \frac{X_1 X_\mathrm{n1} + (1 - X_\mathrm{n1} - X_1) X_\mathrm{n2}}{1 - X_\mathrm{n1}}. \tag{14}$$

The electron mean molecular weight is

$$\frac{1}{\mu_\mathrm{e}} = \frac{X_1 Z_1}{A_1} + \frac{(1 - X_\mathrm{n} - X_1) Z_2}{A_2}. \tag{15}$$

The change in mass fraction X_1 is computed from the continuity

Downloaded from https://academic.oup.com/mnras/article-abstract/319/3/902/1075833 by California Institute of Technology user on 19 May 2020

equation for species (A_1, Z_1),

$$\frac{\partial(nX_1)}{\partial t} + \nabla \cdot (nX_1 \boldsymbol{v}) = -nX_1 R_{\rm ec}(p, X_1, T), \tag{16}$$

where n is the baryon number density, $R_{\rm ec}$ is the electron capture rate (11), and $\boldsymbol{v} = -\hat{r}\dot{M}/4\pi r^2\rho$ is the very slow downward motion of the fluid element. We assume that the accretion flow is predominantly radial and time-independent, so equation (16) becomes

$$\frac{{\rm d}\ln X_1}{{\rm d}r} = \left(\frac{4\pi r^2}{\dot{M}}\right)\rho R_{\rm ec}(p, X_1, T), \tag{17}$$

making clear the competition between the capture rate and the compression time-scale, $t_{\rm comp}$, defined earlier.

We use the sequence of reactions shown in tables 1 and 2 of Haensel & Zdunik (1990b) to describe the crust's composition. Their sequence starts with ^{56}Fe with $X_{\rm n} = 0$ for densities $\rho < 1.5 \times 10^9\,{\rm g\,cm^{-3}}$ and ends with ^{88}Ti with $X_{\rm n} = 0.8$ at densities $\rho > 1.61 \times 10^{13}\,{\rm g\,cm^{-3}}$. For the threshold energy Q, we use the value of the electron chemical potential at the (abrupt) transitions between nuclei in the calculation of Haensel & Zdunik (1990a), as shown in their table 2. Haensel & Zdunik (1990b) stop their calculations at $\rho > 10^{13}\,{\rm g\,cm^{-3}}$, where their equation of state (EOS) for accreted matter approaches the standard Baym, Bethe & Pethick (1971) EOS for cold catalyzed matter, and so the authors stop their tabulation. At these densities the EOS is dominated by neutron pressure, and the exact A and Z of the nuclei have little effect on the EOS. However, an important difference emphasized by Haensel (1997) is that $Z \gtrsim 50$ at the bottom of a cold catalyzed crust, while the accreted model has $Z \sim 20$. While this has little effect on the EOS, the difference in Z does affect the shear modulus (Sato 1979; Haensel 1997).

The crust extends to densities $\rho \approx 2 \times 10^{14}\,{\rm g\,cm^{-3}}$, and there are many more capture layers in the deep crust, each of which contributes to the NS quadrupole moment. Because the tables in Haensel & Zdunik (1990b) extend only to $\rho = 1.61 \times 10^{13}\,{\rm g\,cm^{-3}}$, in all our calculations we insert an extra, ad hoc, movable capture layer in the bottom part of the crust, and study the quadrupole moment induced by this layer as function of its position. We take the crust to be made up of $(A, Z) = (88, 22)$ above the capture layer and $(A, Z) = (82, 20)$ below. We selected these values because in most of the capture reactions listed by Haensel & Zdunik (1990b), two electrons are captured and six neutrons are released.

Figs 4 and 5 show the structure of the capture layers at densities below and above $\rho_{\rm nd}$. The top panel of each figure shows the run of density with pressure (downward direction is to the right). At $\rho < \rho_{\rm nd}$ (Fig. 4), the pressure is supplied entirely by degenerate electrons. In this particular capture layer, Z changes from 20 to 18, so the density jump is $\Delta\rho/\rho = \Delta\mu_{\rm e}/\mu_{\rm e} \approx 2/Z = 10$ per cent. The density change in a capture layer at $\rho > \rho_{\rm nd}$ (Fig. 5) is much smaller, as electrons provide a much smaller fraction of the pressure.

For $\rho > \rho_{\rm nd}$, the capture layers become much thicker, both in pressure coordinates and in physical coordinates. We understand this as follows. Since the reaction rate (11) is exponentially

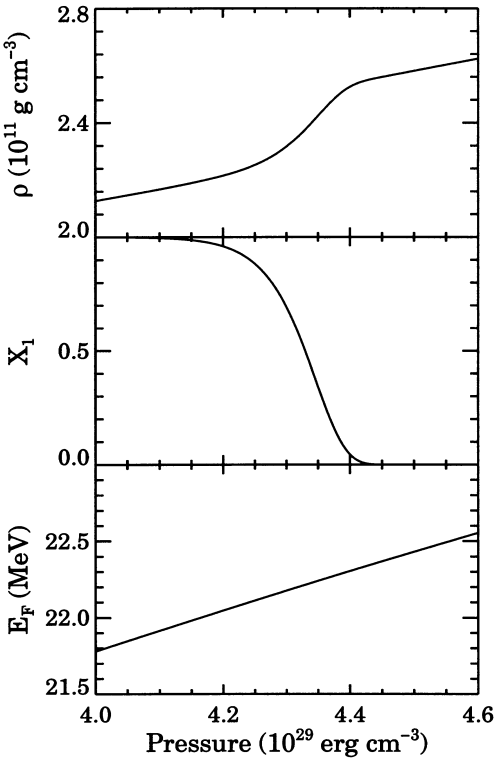

Figure 4. Structure of an electron capture layer in the outer crust, at threshold energy $Q = 23$ MeV. The reaction is $^{56}{\rm Ca} + 2{\rm e}^- \rightarrow {}^{56}{\rm Ar} + 2\nu_{\rm e}$. The top panel shows the run of density with pressure, with the density jump $\Delta\rho/\rho \approx 10$ per cent clearly evident. The middle panel shows the abundance X_1 of ^{56}Ca. The bottom panel shows the electron Fermi energy $E_{\rm F}$. Note that the slope of $E_{\rm F}$ does not change in the capture region, and is always ${\rm d}\ln E_{\rm F}/{\rm d}\ln p = 1/4$.

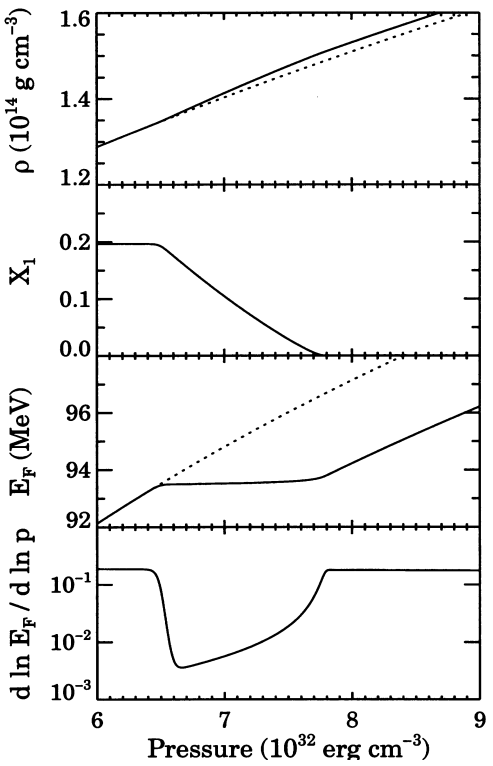

Figure 5. The top three panels are the same as in Fig. 4, but for a capture layer in the inner crust, with threshold $Q = 95$ MeV. For comparison, dotted lines show what the run of ρ (top panel) and $E_{\rm F}$ (third panel) would be if the capture layer was not present. The fourth (bottom) panel shows the slope ${\rm d}\ln E_{\rm F}/{\rm d}\ln p$, computed using equation (A17).

Downloaded from https://academic.oup.com/mnras/article-abstract/319/3/902/1075833 by California Institute of Technology user on 19 May 2020

sensitive to $E_F - Q$, the transition is always sharp in E_F coordinates (see bottom panel of Figs 4 and 5). However, in pressure coordinates, the width of the capture layer is set by $\Delta p/p = (\mathrm{d}\ln E_F/\mathrm{d}\ln p)^{-1}(\Delta E_F/E_F)$, where $\mathrm{d}\ln E_F/\mathrm{d}\ln p$ is given by equation (A17) in Appendix A. Exponential sensitivity of the reaction rate ensures that $\Delta E_F/E_F$ remains approximately constant. At $\rho < \rho_{nd}$, $\mathrm{d}\ln E_F/\mathrm{d}\ln p = 1/4$. However, for $\rho > \rho_{nd}$, it becomes smaller, and within the capture layer itself, extremely small, and the capture layer becomes correspondingly thick (see bottom panel of Fig. 5). In fact, around neutron drip, the increased width of capture layers, coupled with the increasing number of capture layers per unit depth, makes the capture layers overlap.

Because we integrate only one capture reaction at a time, our code cannot deal with overlapping layers, and so we artificially disregard several reactions indicated in Haensel & Zdunik (1990b). This should not lead to any serious problems, as our EOS at these depths is insensitive to the exact (A, Z). Second, as shown in Section 4.1, the quadrupole moments due to different capture layers add linearly, so overlapping capture layers can in principle be dealt with using superposition.

2.3 Hydrostatic structure of the accreted crust

With the composition set, we now discuss the EOS. The electron pressure is that of fully degenerate relativistic $T = 0$ particles, $p_e = 5.77 \times 10^{29}\,\mathrm{erg\,cm^{-3}}\ \ (\rho_{11}/\mu_e)^{4/3}$, where $\rho_{11} = \rho/10^{11}\,\mathrm{g\,cm^{-3}}$. Free neutron pressure is given by the $p_n(n_n)$ fit of Negele & Vautherin (1973), where $n_n = X_n\rho/m_b$. We neglect the ion pressure and the non-ideal and thermal electron effects on the EOS. The total pressure is then $p(\rho) = p_e(\rho) + p_n(\rho)$. The resulting p–ρ relation is shown in Fig. 6, where we have plotted it in such a way as to exhibit the changing balance between electron pressure and neutron pressure. It agrees quite well with the more sophisticated treatments of Haensel & Zdunik (1990a) and Brown (2000).

In order to construct the crust, we pick a starting radius, pressure and mass, and integrate the Newtonian equations of hydrostatic balance and mass conservation,

$$\frac{\mathrm{d}p}{\mathrm{d}r} = -\rho g, \qquad \frac{\mathrm{d}M_r}{\mathrm{d}r} = 4\pi r^2\rho, \tag{18}$$

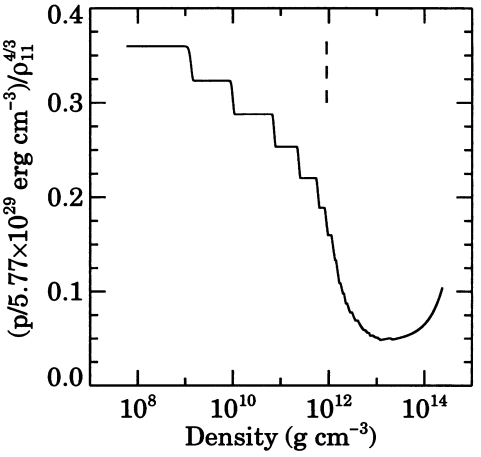

Figure 6. Equation of state used in this work. For densities below neutron drip, the EOS is just that of relativistic electrons. Neutron drip is indicated by a dashed vertical line. We have plotted the EOS in a manner such that the y-axis is ${\mu_e}^{-4/3}$ for $\rho < \rho_{nd}$. The large steps at $\rho < \rho_{nd}$ are from the electron captures, whereas at densities above neutron drip, the density contrasts weaken.

(where M_r is the mass enclosed inside r, and $g = GM_r/r^2$) together with the rate equation (17) for the appropriate species, down towards the core of the star.[2] Following Brown (2000), we decouple the calculation of the thermal structure from the hydrostatic calculation. This is justified since the EOS is nearly independent of temperature. Only the electron capture rate is temperature-sensitive, and so the absolute locations of the capture layers that we find could be in error by a few metres. However, since the effect we are studying depends only on relative motion of the layers, this inaccuracy is of no concern. We start the integration well above the crust, at $p \sim 10^{21}\,\mathrm{erg\,cm^{-3}}$, in order to later apply the thermal boundary condition. The crust begins where the ratio of Coulomb energy to thermal energy,

$$\Gamma_{\mathrm{Coul}} \equiv \frac{Z^2e^2}{akT} \tag{19}$$

[where $a = (3/4\pi n)^{1/3}$ is the internuclear spacing], exceeds 170. We stop the integration when we have reached the fiducial density $\rho \approx 2 \times 10^{14}\,\mathrm{g\,cm^{-3}}$ at the crust–core boundary (for a review and recent results see Pethick et al. 1995). Our (purely Newtonian) fiducial crust is 1.1 km thick and has a mass of $0.06\,\mathrm{M_\odot}$, with a mass of $10^{-4}\,\mathrm{M_\odot}$ in the outer crust. Brown (2000) points out that at high enough accretion rates, the combination of the low nuclear charge Z characteristic of the accreted crust and high temperatures may melt the crust (i.e., make $\Gamma_{\mathrm{Coul}} \leq 170$) around neutron drip. We take this possibility into account by rerunning our Q_{22} calculations with the top of the crust at neutron drip.

2.4 Steady-state thermal structure of the crust

With the hydrostatic structure in hand, we compute the steady-state thermal profile of the crust by solving the heat equation (without GR correction terms)

$$\nabla \cdot \boldsymbol{F} = \rho\epsilon = \rho(\epsilon_{\mathrm{nuc}} - \epsilon_\nu), \tag{20}$$

where the thermal flux $\boldsymbol{F}$ obeys

$$\boldsymbol{F} = -K\nabla T. \tag{21}$$

Here ϵ_{nuc} is the local energy deposited by nuclear reactions, ϵ_ν is the local energy loss due to neutrino emission, and K is the thermal conductivity. We neglect the compressional heating, which is negligible compared to the nuclear energy release (Brown 2000). In our calculation we mostly follow Brown & Bildsten (1998) and Brown (2000) as far as the microphysics is concerned, except for our treatment of nuclear energy release due to reactions in the crust. In particular, for ϵ_ν we adopt a formula based on liquid phase electron $\nu\bar{\nu}$ bremsstrahlung (Haensel, Kaminker & Yakovlev 1996, equation 8), because we expect the crust to be quite impure, and hence neutrino emission due to electron–ion and electron–impurity scattering will dominate over phonon scattering. For the same reason we use the electron–ion scattering conductivity (Schatz et al. 1999, Appendix A, generalization of Yakovlev & Urpin 1980

[2] We initially used a Runge–Kutta integrator with adaptive step-size control. However, the step-size adjustment algorithm tended to take steps that proved too large when we used them to solve the thermal structure and elastic perturbation equations. Namely, the very uneven mesh generated by the integrator led to large round-off errors and convergence difficulties. Our practical solution was to limit the maximum step size to a small fraction (10^{-6}) of the radius. This generates a mesh that is mostly even and has extra resolution near capture layers as necessary.

Downloaded from https://academic.oup.com/mnras/article-abstract/319/3/902/1075833 by California Institute of Technology user on 19 May 2020

results) when computing K, rather than phonon-mediated scattering.

Brown & Bildsten (1998) and Brown (2000) approximated the heat deposition due to nuclear reactions as being uniform in the region around neutron drip. In this paper, since we are resolving individual capture layers, we also resolve the heat release from them (although we find that this more accurate treatment does not lead to significant differences). Let $E_{\rm nuc}$ be the energy (ergs/nucleon) deposited in the transition layer by a single reaction (usually a pair of e^- captures, accompanied by neutron emission at $\rho > \rho_{\rm nd}$). The energy generation rate in the transition layer is then

$$\rho\epsilon_{\rm nuc} = \frac{1}{X_{\rm t}}\frac{{\rm d}X}{{\rm d}r}\left(\frac{E_{\rm nuc}}{4\pi r^2}\right)\left(\frac{\dot{M}}{m_{\rm b}}\right), \quad (22)$$

where $X_{\rm t}$ is the mass fraction of the source nucleus at the top of the layer. The total energy (erg s^{-1}) deposited in the transition layer is $E_{\rm nuc}\dot{M}/m_{\rm b}$. Equation (20) requires two boundary conditions. The boundary condition at the bottom of the crust is set by the ability of the core to radiate the heat flux from the crust as neutrinos. For the bottom boundary condition we consider two cases: a normal core and a superfluid core. For the normal core we use modified Urca neutrino emissivity (Shapiro & Teukolsky 1983, equation 11.5.24). If the core is in a superfluid state, neutrino emissivity is suppressed[3] by a factor $\exp(-\Delta/k_{\rm B}T)$, where Δ is the superfluid gap energy. In general, the gap energy will vary with the density in the core. However, we approximate superfluid effects by just including an overall exponentional factor in the modified Urca formula,

$$L_{\rm core} = 5.3\times10^{39}\,{\rm erg\,s^{-1}}\,\frac{M}{{\rm M}_\odot}\left(\frac{\rho_{\rm nuc}}{\rho}\right)^{1/3} T_9^8\exp\left(-\frac{\Delta}{k_{\rm B}T}\right), \quad (23)$$

where $\rho_{\rm nuc}$ is the nuclear density. If the core is composed solely of normal particles, then $\Delta = 0$, while the typical values of gap energy for superfluid cores is $\Delta \approx 1$ MeV. The boundary condition at the bottom of the crust is just that all heat going into the core comes out as neutrinos, $F + L_{\rm core}/4\pi r^2 = 0$, where F is the radial heat flux; $\boldsymbol{F} = F\hat{\boldsymbol{r}}$.

When nuclear burning in the upper atmosphere is steady, the outer boundary condition is set by the temperature at the hydrogen/helium burning layer, roughly

$$T_{\rm burn} \approx 5.3\times10^8\,{\rm K}\left(\frac{\dot{m}}{\dot{m}_{\rm Edd}}\right)^{2/7}, \quad (24)$$

where $\dot{m}$ is the local accretion rate (Schatz et al. 1999). At sub-Eddington accretion rates [$\dot{m} \lesssim (0.1\text{–}1)\dot{m}_{\rm Edd}$; the exact boundary is not known] the burning in the upper atmosphere is not stable, leading to type I X-ray bursts (see Bildsten 1998b for a recent review). In that case the outer boundary condition is more complicated. However, Brown (2000) found that for high accretion rates, the local heating in the deep crust makes the temperature there very insensitive to the outer boundary temperature. That is no longer true for low accretion rates, where the temperature in the inner crust is much more sensitive to the outer boundary temperature. While the thermal time at the burning layer is quite short, the thermal time in the majority of the crust is on the order of years, much longer than either the burst duration ($\sim$10 s) or the burst recurrence time (hours to days). Hence we expect that in the time-averaged sense, the outer boundary temperature approaches that given by the steady calculation. Thus we adopt a very simple boundary condition by setting $T = T_{\rm burn}$ at $p = 10^{21}$ erg cm^{-3} (the approximate location of the hydrogen/helium burning layer).

Because superfluidity of the core changes the flux profile in the crust, we ran our calculations for two models. Both have the same accretion rate $\dot{M} = 0.5\dot{M}_{\rm Edd}$, use identical microphysics, and share the same hydrostatic structure. However, model S (Fig. 7a) has a superfluid core, with gap energy $\Delta = 1$ MeV, while model N (Fig. 7b) has a normal core (i.e., $\Delta = 0$). These models are very similar to those obtained by Brown (2000), and we refer the reader to that paper for an in-depth review and discussion of their overall thermal properties.

3 TEMPERATURE PERTURBATIONS DUE TO PHYSICAL ASYMMETRIES

As discussed in Section 1.3, there are several possible causes of spin-misaligned lateral temperature variations in the crust. Rather than simply assume a given temperature contrast δT (from which we can calculate Q_{22}), in this section we calculate just how large either the composition variations or nuclear heating variations must be to imprint a given δT. This tells us how large either of these effects must be to generate a sufficient Q_{22} for gravitational radiation to balance the accretion torque.

3.1 Possible sources for the temperature variations

Lateral differences in the crustal composition will have two effects. The first is lateral variations in the amount of energy deposited in the crust by nuclear reactions (since nuclear transmutations of different elements deposit different amounts of energy). We denote lateral variations of this type as $f_{\rm nuc} = \delta E_{\rm nuc}/E_{\rm nuc}$, so that a non-zero $f_{\rm nuc}$ means that more energy is released on one side of the crust than the other.[4] Second, the charge-to-mass ratio Z^2/A is likely to differ if burning proceeds to different A on different sides of the star. The conductivity in the crust scales as $K \propto (Z^2/A)^{-1}\rho T^{n_{\rm k}}$ (Schatz et al. 1999), while neutrino emissivity is $\epsilon_\nu \propto (Z^2/A)\rho T^{n_{\rm e}}$ (Haensel et al. 1996). For the microphysics employed here, $n_{\rm k} \approx 1$ and $n_{\rm e} \approx 6$, so that the conductivity and neutrino emissivity will vary laterally with the composition variation. We denote the Eulerian perturbation in the charge-to-mass ratio as $f_{\rm comp} = \delta(Z^2/A)/(Z^2/A)$. Regions with $f_{\rm comp} > 0$ are more opaque and radiate neutrinos more efficiently. The hydrostatic structure is hardly affected however, as the dependence of the EOS on A and Z is very weak.

Both $f_{\rm nuc}$ and $f_{\rm comp}$ will lead to a calculable lateral temperature variation, δT. An important issue to clarify is the role of the core, which has high thermal conductivity and hence is nearly isothermal. Although the core tends to smooth out temperature variations (i.e., decrease δT), we show that it does not force them to zero in the crust. Because the core's thermal conductivity is much higher than the crust's, δT in the core is much smaller than in the crust. Hence we approximate the core as perfectly

[3] We neglect neutrino emission via e–e bremsstrahlung, which is not exponentially suppressed by nucleon superfluidity and dominates neutrino emission from superfluid NS cores at $T \lesssim 10^8$ K (Kaminker & Haensel 1999).

[4] Since the rate at which the energy released in the crustal nuclear reactions depends on the local accretion rate (see equation 22), a similar effect would occur if the crust had laterally uniform composition entering at the top, but different local compression rates.

Downloaded from https://academic.oup.com/mnras/article-abstract/319/3/902/1075833 by California Institute of Technology user on 19 May 2020

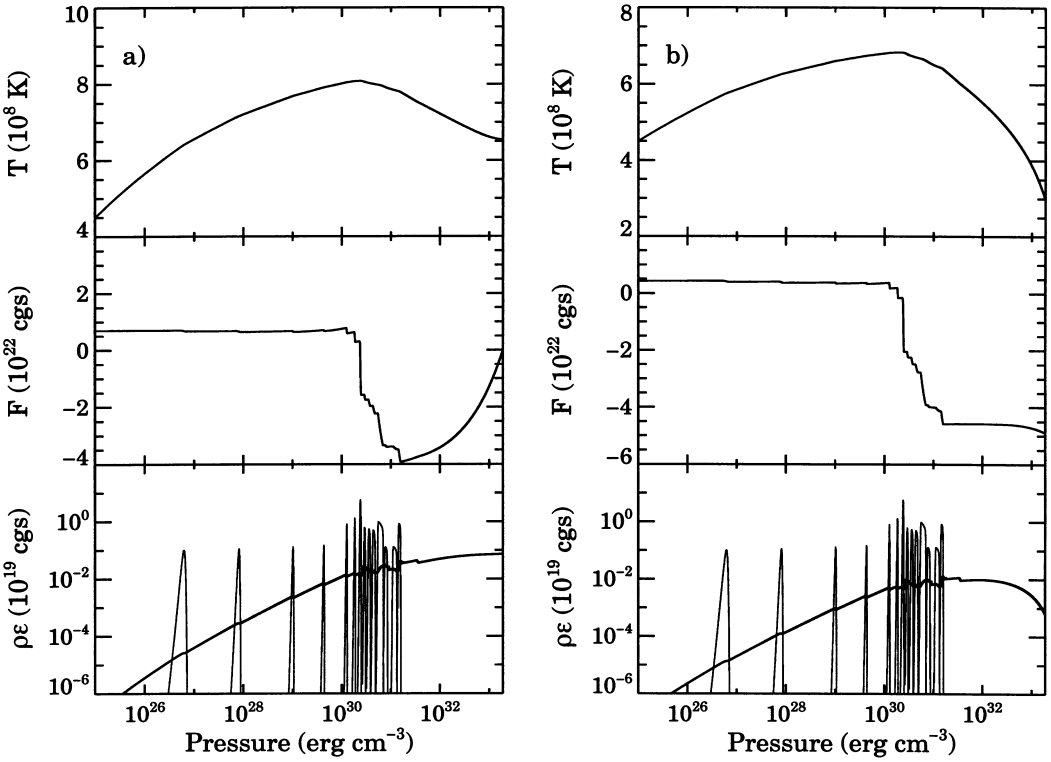

Figure 7. Left (a): Thermal structure of model S ($0.5\dot{M}_{\rm Edd}$ accretion rate, superfluid gap $\Delta = 1$ MeV). The top panel shows the temperature of the crust. The middle panel shows the heat flux F_r in the crust ($F_r < 0$ means the heat is flowing toward the core). The bottom panel shows the local energy release $\rho\epsilon_{\rm nuc}$ (in erg cm^{-3} s^{-1}) due to reactions in the crust (sharp spikes) and the local rate of neutrino cooling $\rho\epsilon_\nu$ (also in erg cm^{-3} s^{-1}). Right (b): Same as (a), but for model N ($0.5\dot{M}_{\rm Edd}$ accretion rate, superfluid gap $\Delta = 0$ MeV, i.e., normal fluid in the core).

conducting and isothermal. The crust is internally heated by nuclear reactions near neutron drip, and therefore is not at the same temperature as the core. The crustal thermal equilibrium is set mostly by the heat flux in the radial direction, implying that the radial temperature gradient on the side with positive $f_{\rm nuc}$ or $f_{\rm comp}$ must be steeper in order to connect to the same core temperature. We now calculate this δT.

3.2 The thermal perturbation equations and boundary conditions

While the ultimate effect of $f_{\rm nuc}$ and $f_{\rm comp}$ is to shift the location of capture layers, to first order we can calculate δT by considering the effects of $f_{\rm nuc}$ and $f_{\rm comp}$ on a spherically symmetric background. After computing δT, we will find in Section 4 how the crust hydrostatically readjusts. To first order, we then set $\delta\rho = 0$, and the conductivity perturbation equation is simply

$$\frac{\delta K}{K} = -f_{\rm comp} + n_{\rm k}\frac{\delta T}{T}, \tag{25}$$

while the neutrino emissivity perturbation is $\delta\epsilon_\nu/\epsilon_\nu = f_{\rm comp} + n_{\rm e}\delta T/T$.

The nuclear energy generation rate perturbation requires special attention. Nuclear reactions are generally quite temperature-sensitive. However, despite the temperature perturbation, the total energy release of a complete capture layer depends only on the local accretion rate and the total $E_{\rm nuc}$ of the element. A temperature perturbation shifts the capture layer and hence leads to a local change in $\epsilon_{\rm nuc}$ on scales smaller than the distance over which the layers shift. However, it cannot change the total amount of energy released. Since we neglect the shifts of capture layers at this stage, we simply have $\delta\epsilon_{\rm nuc}/\epsilon_{\rm nuc} = f_{\rm nuc}$. In some sense, we average the energy generation rate over the scale of the entire capture layer. This approximation simplifies the calculation considerably. The Eulerian perturbation to $\epsilon \equiv \epsilon_{\rm nuc} - \epsilon_\nu$ (the local nuclear heating rate minus the neutrino cooling rate) is therefore

$$\frac{\delta\epsilon}{\epsilon} = f_{\rm nuc}\frac{\epsilon_{\rm nuc}}{\epsilon} - \left(f_{\rm comp} + n_{\rm e}\frac{\delta T}{T}\right)\frac{\epsilon_\nu}{\epsilon}. \tag{26}$$

We assume that the angular dependence of all perturbed quantities is $\propto Y_{lm}$, i.e., $\delta T(r,\theta,\phi) = \delta T(r)Y_{lm}(\theta,\phi)$. Perturbing the heat equation (20) and the flux equation (21), and keeping only first-order terms, gives

$$\delta F^a = \left(\frac{\delta K}{K}F - K\frac{{\rm d}\delta T}{{\rm d}r}\right)Y_{lm}\hat{r}^a - \frac{K\delta T}{r}\nabla^a Y_{lm} \tag{27}$$

and

$$\frac{1}{r^2}\frac{\rm d}{{\rm d}r}\left(r^2K\frac{{\rm d}\delta T}{{\rm d}r}\right) - l(l+1)\frac{K\delta T}{r^2} = \rho\epsilon\left(\frac{\delta K}{K} - \frac{\delta\epsilon}{\epsilon}\right) + F\frac{\rm d}{{\rm d}r}\left(\frac{\delta K}{K}\right). \tag{28}$$

Substituting for $\delta K/K$ and $\delta\epsilon/\epsilon$, and using equation (21), equation (28) becomes

$$\frac{1}{r^2}\frac{\rm d}{{\rm d}r}\left(r^2K\frac{{\rm d}\delta T}{{\rm d}r}\right) - n_{\rm k}\frac{F}{KT}K\frac{{\rm d}\delta T}{{\rm d}r} - l(l+1)\frac{K\delta T}{r^2} - \left\{n_{\rm k}\frac{F^2}{KT} + \rho[n_{\rm k}(\epsilon_{\rm nuc} - \epsilon_\nu) + n_{\rm e}\epsilon_\nu]\right\}\frac{\delta T}{T} = \rho[f_{\rm comp}(2\epsilon_\nu - \epsilon_{\rm nuc}) - f_{\rm nuc}\epsilon_{\rm nuc}], \tag{29}$$

Downloaded from https://academic.oup.com/mnras/article-abstract/319/3/902/1075833 by California Institute of Technology user on 19 May 2020

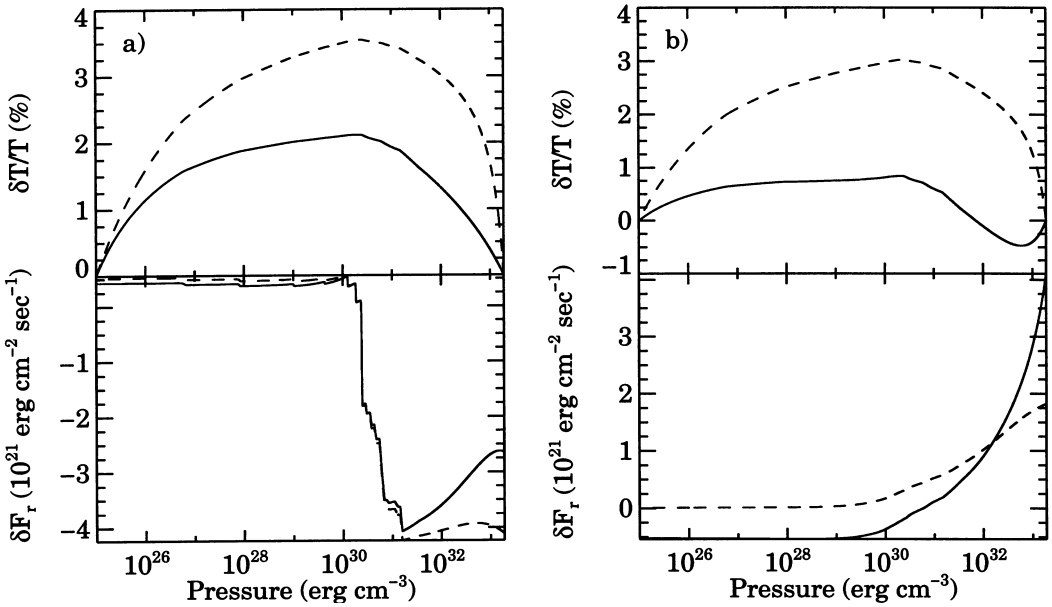

Figure 8. Left (a): Temperature and flux perturbations in the crust resulting from laterally varying energy release, $f_{\rm nuc} = 0.1$, but unperturbed conductivity, $f_{\rm comp} = 0$. Angular dependence of the perturbation is $l = 2$, i.e., a quadrupole. The top panel shows the temperature perturbation $\delta T/T$, while the bottom panel displays the radial flux perturbation δF_r. Solid lines correspond to model S (superfluid core, $\dot{M} = 0.5\dot{M}_{\rm Edd}$), while dashed lines represent model N (normal core, same accretion rate). Transverse heat flux $\delta F_\perp$ is not shown, as it is much smaller than δF_r in the crust. Right (b): same as (a), but the energy release is not perturbed, $f_{\rm nuc} = 0$, while the charge to mass ratio Z^2/A is varied laterally, $f_{\rm comp} = 0.1$.

where we have neglected $\mathrm{d}n_{\rm k}/\mathrm{d}r$, and for simplicity have taken the composition perturbation to be radially uniform, so $\mathrm{d}f_{\rm comp}/\mathrm{d}r = 0$.

The thermal perturbation problem, equation (29), requires two boundary conditions. At the top of the crust, the exact boundary condition can be obtained by matching to a flux–temperature relation in the ocean, where the thermal profile is set by compressional heating and that portion of the nuclear energy released in the deep crust that flows upward through the ocean, rather than down into the core (Bildsten & Cutler 1995; Brown & Bildsten 1998). However, since the ocean's thermal conductivity is much higher than the crust's, we simplify our calculation by adopting the boundary condition, $\delta T(\mathrm{top}) = 0$. The variation in the *flux* coming out of the crust is *not* zero; in fact, it is potentially observable.

Now consider the boundary condition at the crust–core interface. The thermal conductivity in the core is at least several orders of magnitude higher than in the crust. Hence any extra flux into the core can be carried with a very small temperature perturbation, as we now show. First, consider a superfluid core. The boundary condition for the spherically symmetric calculation is $F_{\rm core} = 0$, since neutrino emission is suppressed and the core cannot radiate away any significant heat flowing into it (Section 2). However, we are now lifting the restriction of spherical symmetry, so heat can flow into the core on one side and out the other. The size of δT in the core is then related to the magnitude of the radial flux perturbation by $\delta F_{\rm r,core} \sim (K_{\rm core}T/R)(\delta T/T)|_{\rm core}$. The magnitude of the transverse flux $\delta F_{\perp,\rm core}$ is of the same order, contrary to the situation in the crust, where the transverse heat flux is much smaller. The radial flux perturbation in the crust is $\delta F_{\rm r,crust} \sim (K_{\rm crust}T/\Delta R)(\delta T/T)|_{\rm crust}$, where $(\delta T/T)|_{\rm crust}$ is the typical magnitude of the temperature perturbation in the crust, and ΔR is the thickness of the crust. Continuity of the radial flux at the crust–core boundary then gives

$$\left.\frac{\delta T}{T}\right|_{\rm core} \sim \frac{K_{\rm crust}}{K_{\rm core}}\frac{R}{\Delta R}\left.\frac{\delta T}{T}\right|_{\rm crust} \ll \left.\frac{\delta T}{T}\right|_{\rm crust}. \qquad (30)$$

When the NS core is not a superfluid, it can emit neutrinos and the equilibrium model has a non-zero flux $F_{\rm core}$ going into the core (see Fig. 7). The radial flux perturbation in the core is then determined by the competition of two terms in equation (27), $(\delta K/K)F_{\rm core}$ and $K\mathrm{d}\delta T/\mathrm{d}r \sim (K_{\rm core}T/R)(\delta T/T)$. The core is nearly isothermal, so $K_{\rm core}T/R \gg F_{\rm core}$ (i.e., the proper estimate of $F_{\rm core}$ is $K_{\rm core}\Delta T/R$, where $\Delta T \ll T$ is the difference in temperature between, say, the centre and the crust–core boundary). Therefore the second term, $K\mathrm{d}\delta T/\mathrm{d}r$, dominates, and, just as in the case of a superfluid core, we have $\delta F_{\rm r,core} \sim (K_{\rm core}T/R)(\delta T/T)|_{\rm core}$. Thus we again arrive at equation (30), i.e., the typical magnitude of δT in the crust is several orders of magnitude larger than δT in the core.

Hence for both the normal and superfluid core, to good accuracy we can take $\delta T = 0$ as our boundary condition at the crust–core boundary. With this boundary condition, we do not need to model the core, as we effectively assume that it is perfectly conducting. However, perturbed flux *is* flowing through the core.

3.3 The resulting temperature variations

Solutions of the perturbation problem (29) are shown in Fig. 8 for the quadrupole ($l = m = 2$) case,[5] for accretion rate $\dot{M} = 0.5\dot{M}_{\rm Edd}$. In Fig. 8(a) we presume that the nuclear heating varies laterally by 10 per cent, i.e., $f_{\rm nuc} = 0.1$, but take $f_{\rm comp} = 0$, so that conductivity and neutrino emissivity are unperturbed. The resulting temperature perturbations are shown in the top panel, with the solid line representing the superfluid-core case (gap energy $\Delta = 1$ MeV), while the dashed line corresponds to the case of a normal core

[5] The thermal perturbation equations do not depend on m, so our solutions are valid for any $l = 2$ perturbation.

Downloaded from https://academic.oup.com/mnras/article-abstract/319/3/902/1075833 by California Institute of Technology user on 19 May 2020

($\Delta = 0$).[6] Fig. 8(b) shows the solutions for the opposite case, where $f_{\rm nuc} = 0$ but $f_{\rm comp} = 0.1$. The bottom panels of the figures show the perturbation in the radial heat flux δF_r. The transverse flux *in the crust* is negligible in all cases, and is not shown here.

We see that the typical $\delta T/T$ for $\dot{M} = 0.5\dot{M}_{\rm Edd}$ near the bottom of the crust is roughly (0.1–0.3)f, where f is either $f_{\rm comp}$ or $f_{\rm nuc}$. Equivalently, the temperature perturbation δT is a few $\times 10^6$ K for $f_{\rm comp}$ or $f_{\rm nuc}$ of 10 per cent, with the maximum δT attained around neutron drip. The temperature perturbations tend to be larger in models with a normal core than with a superfluid core. One might have expected that the amplitude of $\delta T/T$ would be of order $f_{\rm nuc}$ or $f_{\rm comp}$. This is not the case, because the crust can radiate away some of the 'extra' flux it needs to carry by emitting neutrinos, thus reducing the lateral temperature gradient. However, this enhanced neutrino emission does not completely eliminate the lateral temperature gradient.

In Fig. 9 we survey the dependence of the temperature perturbations on the accretion rate. Most of the heat released by the nuclear reactions near neutron drip (roughly 1 MeV per accreted baryon) flows towards the core and is lost as neutrino emission either from the crust or from the core. However, a fraction of the heat flows towards the surface of the star. This flux $F(r_{\rm top})$ is plotted in the top panel of Fig. 9, scaled by the accretion flux $F_{\rm A} \approx (1/4\pi R^2)(GM\dot{M}/R)$, or $\approx 200\,{\rm MeV}/4\pi R^2/{\rm accreted\ baryon}$. The solid line denotes a model with a normal core, while the dashed line corresponds to the model with a superfluid core. In the superfluid case a smaller fraction of the heat escapes to the surface, because the crust is hotter and hence crustal bremsstrahlung is more effective at radiating the heat deposited by nuclear reactions on the spot.

The middle panel of Fig. 9 shows the magnitude of the temperature perturbations that result when either the local heating rate is perturbed by 10 per cent ($f_{\rm nuc} = 0.1$, lines marked with filled triangles) or the charge-to-mass ratio is altered, leading to lateral variations in the conductivity and neutrino emissivity ($f_{\rm comp} = 0.1$, lines marked with open circles). The typical magnitude of $\delta T/T$ is a few per cent for the models with a normal core (dashed lines) and is somewhat smaller for models with a superfluid core (solid lines). We must emphasize that our temperature perturbation calculation is linear, and hence a 20 per cent asymmetry will result in temperature perturbations that are a factor of 2 larger, so long as $\delta T/T \ll 1$.

These temperature perturbations displace the capture layers and create a quadrupole moment. However, in addition, they result in lateral variations in the flux leaving the top of the crust. The amplitude of this flux perturbation, $\delta F_r(r_{\rm top})$, is plotted in the bottom panel of Fig. 9, scaled by the accretion flux $F_{\rm A}$. The typical magnitude of the flux modulation is $\delta F_r/F_{\rm A} \approx 10^{-4}(f/0.1)$. These hot and cold spots, when moving in and out of the view of the observer due to the rotation of the neutron star, can generate a modulation in the persistent emission. Observational implications of this effect are discussed in Section 5.

The existence of lateral temperature variations depends on the continual heating of the crust. When accretion halts, thermal diffusion will slowly equalize the temperature laterally. How long will this process take?

[6] We have probably overestimated the neutrino emission suppression in a superfluid core (i.e., our model S). As Brown (2000) points out, the neutrino emissivity depends very sensitively on temperature so that even a moderate number of normal particles in the core can radiate away an appreciable fraction of the flux from nuclear reactions in the deep crust. Hence it is likely that $\delta T/T$ of model N is more representative.

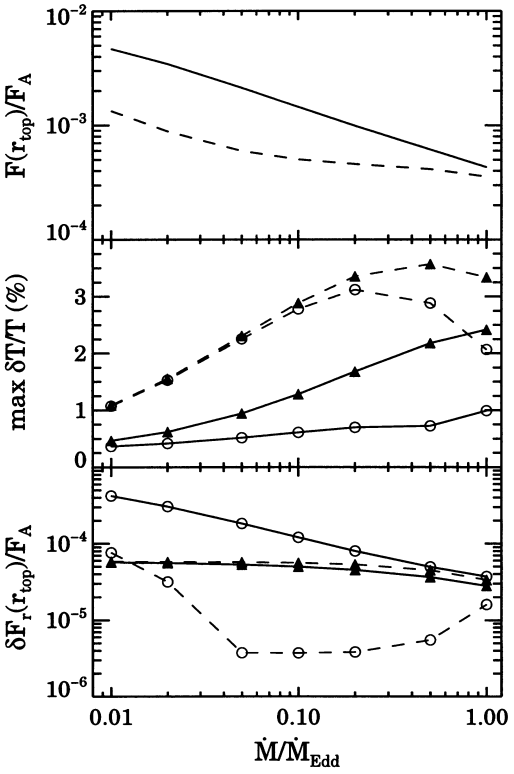

Figure 9. Top panel: the unperturbed flux emerging from the top of the crust due to the (spherically symmetric) direct heat input by the nuclear reactions around neutron drip. The flux $F(r_{\rm top})$ has been scaled by the accretion flux $F_{\rm A} = 1.4 \times 10^{25}\,{\rm erg\,cm^2\,s^{-1}}(\dot{M}/\dot{M}_{\rm Edd})$, so $F/F_{\rm A} = 10^{-3}$ corresponds to a luminosity of 200 keV per accreted baryon emerging from the top of the crust. The solid line denotes the model with a superfluid core ($\Delta = 1$ MeV), and the dashed line denotes the model with a normal core ($\Delta = 0$). Middle panel: the maximum magnitude of the crustal temperature perturbation $\delta T/T$ induced by asymmetric heat sources ($f_{\rm nuc} = 0.1$, lines marked with filled triangles) and opacity/neutrino emissivity variations ($f_{\rm comp} = 0.1$, lines marked with open circles). Solid lines are the results for the model with a superfluid core, and dashed lines correspond to the model with a normal core. These results scale linearly with $f_{\rm nuc}$ and $f_{\rm comp}$. Bottom panel: the perturbation to the flux emerging from the top of the crust due to the asymmetry in nuclear energy release ($f_{\rm nuc} = 0.1$) and Z^2/A ($f_{\rm comp} = 0.1$). The flux perturbation δF_r has been scaled by the accretion flux $F_{\rm A}$. The legend is the same as in the middle panel.

First, let us compare the transverse flux perturbation in the crust $\delta F_\perp$ to the radial one, δF_r, as one would expect that lateral heat transport could be responsible for equalizing the temperature. From equation (21), the background flux in the crust is $F \sim KT/\Delta R$, while from equation (27) the transverse flux perturbation $\delta F_\perp = K\delta T/R \sim F(\Delta R/R)(\delta T/T)$. The perturbed radial flux is the sum of two terms, both of size $\sim F(\delta T/T)$. So, for low angular order l, the perturbed transverse flux is smaller than the radial piece by a factor $\sim \Delta R/R$. Hence the transverse heat flux in the crust does not wash out the temperature perturbations. The heat is transported predominantly radially through the crust, and both radially and transversely through the core. Hence, if accretions stops, the temperature perturbation will be washed out in a thermal time at the bottom of the crust,

$$t_{\rm th} \approx 6\,{\rm yr}\left(\frac{p}{10^{32}\,{\rm erg\,cm^{-3}}}\right)^{3/4} \qquad (31)$$

(Brown, Bildsten & Rutledge 1998). The transverse temperature

Downloaded from https://academic.oup.com/mnras/article-abstract/319/3/902/1075833 by California Institute of Technology user on 19 May 2020

asymmetry will therefore persist so long as (1) accretion persists on time-scales longer than a few years, and (2) the crust has compositional asymmetries.

What does this mean for our quadrupole generation mechanism? In steadily accreting sources, we would expect the quadrupole moment not to vary in time, and hence their spin will be set by the competition of accretion with gravitational radiation torque. However, as suggested by Bildsten (1998a), transiently accreting sources with long recurrence times may be able to spin up to shorter periods, since, because of the short thermal time, the temperature variations in the deep crust and their quadrupole moments may be lower than what one would expect from just the time-averaged accretion rate.

4 THE ELASTIC DEFORMATION OF THE CRUST

In this section we derive and solve the perturbation equations that describe the elastic response of the crust to lateral composition gradients. Although our primary interest is *rotating* neutron stars with $\nu_s \approx 300\,\mathrm{Hz}$, we consider deformations of non-rotating, spherically symmetric background models. For static deformations (i.e., no Coriolis force), centrifugal terms modify our results only by order $(\nu_s/\nu_b)^2 \sim 5$ per cent, where $\nu_b \approx 1.5\,\mathrm{kHz}$ is the NS breakup frequency. A given level of temperature or composition asymmetry gives rise to 'mountains' of a certain size, where that size is only slightly modified by rotation. However, because the deformed star rotates, it emits gravitational waves.

We treat two cases: one where the lateral composition gradient is due to a wavy e^- capture boundary (and the gradient is therefore confined to a region near the layer), and another where the lateral composition gradient is uniform throughout the crust. Real neutron stars probably exhibit both types of composition gradients at some level; for small distortions, their effects should add linearly. These lateral asymmetries, treated as perturbations on a homogeneous background, cause pressure imbalances that source a crustal displacement field ξ^a. Treating the crust as an elastic solid, we solve for the ξ^a that brings the crust back to equilibrium, with the gravitational, pressure, and shear-stress forces all in balance. We then compute the density perturbation $\delta\rho$ and the resulting Q_{22}. An important underlying assumption is that the stresses are small enough that the NS crust *can* be in static equilibrium. More precisely, we assume that the crust is deforming slowly enough that the elastic part of the viscoelastic stress tensor dominates over the viscous part. If the stresses are much larger than the crust's yield stress, then this cannot be true.

The process by which deformation is built up in an NS is undoubtedly complex, involving the viscoelastic response of the crust to temperature and composition gradients that are built up over time, during which the primordial crust is replaced by accreted matter. A full understanding of crustal deformation would involve solving the time-evolution equations for all relevant aspects of the crust, from the moment accretion starts. This would involve plastic flow or breaking whenever the crustal yield strain was reached. Such a 'movie' of the crust's history is well beyond our current abilities. Instead, our solution of the perturbed hydroelastic equations essentially amounts to taking a 'snapshot' of the crust. We find that this approach gives a lot of detailed information, but necessarily we must put in some things 'by hand.'

One important thing we put in by hand is the reference state of the crust: for simplicity, we take it to be spherically symmetric. Namely, we assume that if one could somehow 'undo' the 'extra' e^- captures that cause the capture layer to be wavy, then the NS would 'bounce back' to a configuration with zero quadrupole moment. Since the NS crust may have undergone a long history of plastic flow and cracking, it is not clear how closely the real crust matches this picture. Fortunately, it is easy to see how this assumption affects our results. Assume that, in the absence of any lateral composition gradients currently driving the NS away from spherical symmetry, the star would adopt a shape with multipole moments Q_{lm}^{hist}. The superscript 'hist' refers to the fact that for 'historical reasons,' the crust has evolved to an equilibrium shape that is non-spherical. (Of course, almost all the solid objects we use in daily life have non-spherical equilibrium shape: we manufacture them that way.) Let Q_{lm}^{pert} be the piece due to the current lateral composition gradient, assuming the reference shape is spherical. Both deviations will be small, and to first order they add linearly:

$$Q_{lm}^{\mathrm{total}} = Q_{lm}^{\mathrm{hist}} + Q_{lm}^{\mathrm{pert}}. \tag{32}$$

We guess that the dominant historical forces that shaped Q_{22}^{hist} (e.g., through viscoelastic flow) are the same ones that currently shape Q_{22}^{pert}. Correspondingly, we guess that the two pieces tend to add coherently, rather than to cancel. For example, consider a spherical shell of steel, and apply a large inward force at two opposite points on the equator. At first, Q_{lm}^{total} is just Q_{lm}^{pert}, the distortion due to the existing force. However, over time the steel also relaxes somewhat, and the effect is obviously to increase the total deformation. One might then wonder how large Q_{22}^{total} could grow over time, for a fixed Q_{22}^{pert}. It is partly to address that question that we derive, in Section 6, an upper limit on Q_{22}^{total}, independent of the relative contributions of Q_{lm}^{hist} and Q_{lm}^{pert}.

In the rest of Section 4 we omit the superscript 'pert' from Q_{22}^{pert}, but hopefully it is now clear that the neutron star's total Q_{22} does have another piece, Q_{22}^{hist}.

Now let us turn to the source of Q_{22}^{pert}. As stated above, we consider two types: composition gradients due to wavy capture boundaries, and composition gradients that are radially uniform. Our model of the wavy capture boundary is as follows. We posit the existence of some Eulerian temperature perturbation $\delta T \equiv \mathrm{Re}\{\delta T(r) Y_{lm}(\theta,\phi)\}$, superimposed on a background that would otherwise have spherically symmetric composition. One possible source of such δT is the asymmetric heat flow due to laterally varying nuclear heating or conductivity (Z^2/A), as computed in Section 3. Regions where $\delta T(r)$ is positive (negative) have their e^- capture layers shifted to lower (higher) density, as discussed in Sections 1.2 and 2.1. Essentially one ends up with a crustal EOS that is angle-dependent near the capture layer, and which requires shear stresses to be in equilibrium.

The other source we consider is a (radially) uniform lateral composition gradient, $\Delta\mu_e/\mu_e \equiv \mathrm{Re}\{C Y_{lm}(\theta,\phi)\}$, for some constant C. The resulting Q_{22} will scale linearly with C; our fiducial choice is $C = 5\times10^{-3}$. The effect is again to give angular dependence to the crust's EOS, but this dependence is now small and uniform rather than large and confined to the e^- capture regions. It should be clear that we do not think that $\Delta\mu_e/\mu_e(r)$ will really be a constant, but we just consider it in an averaged sense. Our use of Lagrangian $\Delta\mu_e$ here instead of Eulerian $\delta\mu_e$ reflects the fact that we are specifying the composition gradient that *would* exist (due to accretion and/or burning asymmetries, say) if the crust did not elastically adjust.

Having explained the background solution and the sources, we now derive the crustal perturbation equations.

Downloaded from https://academic.oup.com/mnras/article-abstract/319/3/902/1075833 by California Institute of Technology user on 19 May 2020

4.1 The crustal perturbation equations

Our calculation is based on the following assumptions and approximations. We use Newtonian gravity throughout. We model the crust as an elastic solid with shear modulus μ and two-parameter EOS: $p = p(\rho, \mu_e)$, where ρ is the density, and μ_e is the electron mean molecular weight. We neglect temperature in the EOS, except in so far as it affects μ_e (see Appendix A for details). We neglect the slight overall downward flow of matter due to accretion; this is justified since the ram pressure at relevant depths is completely negligible compared to gravity or shear forces. We presume that the crust responds elastically, i.e., we do not allow the stresses to relax plastically or via cracking. The stress-energy tensor of the solid is then

$$\boldsymbol{\tau}_{ab} = -p(\rho, \mu_e)\boldsymbol{g}_{ab} + \mu\left(\nabla_a\xi_b + \nabla_b\xi_a - \tfrac{2}{3}\boldsymbol{g}_{ab}\nabla^c\xi_c\right), \tag{33}$$

where g^{ab} is the flat 3-metric, and ∇_a is its associated derivative operator. The equation of static balance is $\nabla^a\boldsymbol{\tau}_{ab} = \rho\nabla_b\Phi$, where Φ is the gravitational potential.

We carry out first-order perturbation theory with a spherically symmetric background model (constructed in Section 2) that has zero shear stress. Thus we treat ξ^a as a first-order quantity. We neglect the perturbation of the gravitational potential Φ (the Cowling approximation; but see Section 6.5 where we relax this approximation). We use δ to represent Eulerian perturbations and Δ for Lagrangian perturbations. For scalar quantities Λ, they are related by $\Delta\Lambda = \delta\Lambda + \xi^a\nabla_a\Lambda$, where ξ^a is the displacement vector of the elastic solid from its original state. Since the background model is spherically symmetric, *both* the Eulerian and Lagrangian variations of scalars are proportional to Y_{lm}, and $\Delta\Lambda(r) = \delta\Lambda(r) + \xi_r \mathrm{d}\Lambda/\mathrm{d}r$.

The Lagrangian pressure perturbation depends on which effect causes the crustal EOS to have non-trivial angular dependence. In the case of a smooth composition gradient, $\Delta\mu_e/\mu_e$, we write

$$\Delta p = \left.\frac{\partial p}{\partial\rho}\right|_{\mu_e}\Delta\rho + \left.\frac{\partial p}{\partial\mu_e}\right|_{\rho}\Delta\mu_e, \tag{34}$$

since $p = p(\rho, \mu_e)$. For the δT source term, we write

$$\Delta p = \left.\frac{\partial p}{\partial\rho}\right|_{T}\Delta\rho + \left.\frac{\partial p}{\partial\mu_e}\right|_{\rho}\Delta T = \left.\frac{\partial p}{\partial\rho}\right|_{T}\Delta\rho + \left.\frac{\partial p}{\partial\mu_e}\right|_{\rho}\left(\delta T + \xi_r\frac{\mathrm{d}T}{\mathrm{d}r}\right), \tag{35}$$

where in the second equality we used the relation between Eulerian and Lagrangian perturbations. Evaluation of the source terms and coefficients in equations (34) and (35) is discussed in detail in Appendix A. The only transformation we make here is to decompose the source terms into spherical harmonics, i.e., we write $\Delta\mu_e = \Delta\mu_e(r)Y_{lm}(\theta, \phi)$ and $\delta T = \delta T(r)Y_{lm}(\theta, \phi)$. In either case, the perturbation 'sources' a displacement vector ξ^a of the form

$$\xi^a \equiv \xi_r(r)Y_{lm}\hat{r}^a + \xi_\perp\beta^{-1}r\nabla^a Y_{lm}, \tag{36}$$

where $\hat{r}^a$ is the unit radial vector, and $\beta \equiv \sqrt{l(l+1)}$.

The perturbation equations for the crust are then[7]

$$\nabla^a\delta\tau_{ab} = \delta\rho g\hat{r}_b. \tag{37}$$

[7] These equations can also be derived by explicitly writing out the components of the stress tensor and its divergence in spherical coordinates. We found the tabulation of the components of the stress tensor in Takeuchi & Sato (1972) very useful.

Here $g(r) \equiv GM_r/r^2$ is the local gravitational acceleration of the background model, and $\delta\tau_{ab}$ is given by[8]

$$\delta\tau_{ab} = \boldsymbol{g}_{ab}Y_{lm}\delta\tau_{rr} + \boldsymbol{e}_{ab}Y_{lm}[2\mu(\xi_r/r - \partial_r\xi_r)] + \boldsymbol{f}_{ab}\delta\tau_{r\perp} + \boldsymbol{\Lambda}_{ab}2\mu\beta\xi_\perp/r, \tag{38}$$

where

$$\delta\tau_{rr} = -\delta p + \mu\left(\tfrac{4}{3}\partial_r\xi_r - \tfrac{4}{3}\xi_r/r + \tfrac{2}{3}\beta\xi_\perp/r\right), \tag{39a}$$

$$\delta\tau_{r\perp} = \mu(r\partial_r(\xi_\perp/r) + \beta\xi_\perp/r), \tag{39b}$$

and

$$\boldsymbol{e}_{ab} \equiv \boldsymbol{g}_{ab} - \hat{r}_a\hat{r}_b, \tag{40a}$$

$$\boldsymbol{f}_{ab} \equiv \beta^{-1}r(\hat{r}_a\nabla_b Y_{lm} + \hat{r}_b\nabla_a Y_{lm}), \tag{40b}$$

$$\boldsymbol{\Lambda}_{ab} \equiv \beta^{-2}r^2\nabla_a\nabla_b Y_{lm} + \boldsymbol{f}_{ab}. \tag{40c}$$

Note that there is no $\delta\mu$ term in equation (37), since in equation (33) the shear modulus μ is multiplied by terms involving ξ_a, which vanish in the background model. The Eulerian density perturbation $\delta\rho$ in equation (37) follows from the perturbed continuity equation,

$$\delta\rho = -\nabla^a(\rho\xi_a) = -\left[\frac{1}{r^2}\frac{\partial}{\partial r}(r^2\rho\xi_r) - \rho\beta\frac{\xi_\perp}{r}\right]Y_{lm}, \tag{41}$$

and the Eulerian pressure perturbation $\delta p = \Delta p + \rho g\xi_r$ in equation (39a) follows from either equation (34) or equation (35), depending on the type of perturbation imposed upon the crust.

The radial and perpendicular pieces of equation (37) yield two second-order equations for the variables ξ_r and $\xi_\perp$. Following McDermott, Van Horn & Hansen (1988), we rewrite these as four first-order equations, using variables

$$z_1 \equiv \frac{\xi_r}{r}, \qquad z_2 \equiv \frac{\Delta\tau_{rr}}{p} = \frac{\delta\tau_{rr}}{p} - z_1\frac{\mathrm{d}\ln p}{\mathrm{d}\ln r}, \tag{42}$$

$$z_3 \equiv \frac{\xi_\perp}{\beta r}, \qquad z_4 \equiv \frac{\Delta\tau_{r\perp}}{\beta p} = \frac{\delta\tau_{r\perp}}{\beta p}.$$

The resulting equations are

$$\frac{\mathrm{d}z_1}{\mathrm{d}\ln r} = -\left(1 + 2\frac{\alpha_2}{\alpha_3} - \frac{\boldsymbol{\alpha_4}}{\boldsymbol{\alpha_3}}\right)z_1 + \frac{1}{\alpha_3}z_2 + l(l+1)\frac{\alpha_2}{\alpha_3}z_3 + \frac{\mathbf{1}}{\boldsymbol{\alpha_3}}\boldsymbol{\Delta S}, \tag{43a}$$

$$\frac{\mathrm{d}z_2}{\mathrm{d}\ln r} = \left(\tilde{U}\tilde{V} - 4\tilde{V} + 12\Gamma\frac{\alpha_1}{\alpha_3} - \mathbf{4}\frac{\boldsymbol{\alpha_1\alpha_4}}{\boldsymbol{\alpha_3}}\right)z_1 + \left(\tilde{V} - 4\frac{\alpha_1}{\alpha_3}\right)z_2 + l(l+1)\left(\tilde{V} - 6\Gamma\frac{\alpha_1}{\alpha_3}\right)z_3 + l(l+1)z_4 - \mathbf{4}\frac{\boldsymbol{\alpha_1}}{\boldsymbol{\alpha_3}}\boldsymbol{\Delta S}, \tag{43b}$$

$$\frac{\mathrm{d}z_3}{\mathrm{d}\ln r} = -z_1 + \frac{1}{\alpha_1}z_4, \tag{43c}$$

[8] When not explicitly specified, all *physical* quantities are obtained by taking real parts of the corresponding complex expressions.

Downloaded from https://academic.oup.com/mnras/article-abstract/319/3/902/1075833 by California Institute of Technology user on 19 May 2020

$$\frac{\mathrm{d}z_4}{\mathrm{d}\ln r} = \left(\tilde{V} - 6\Gamma\frac{\alpha_1}{\alpha_3} + \mathbf{2}\frac{\alpha_1\alpha_4}{\alpha_3}\right)z_1 - \frac{\alpha_2}{\alpha_3}z_2 + \frac{2}{\alpha_3}\{[2l(l+1)-1]\alpha_1\alpha_2 + 2[l(l+1)-1]\alpha_1^2\}z_3 + (\tilde{V}-3)z_4 + \mathbf{2}\frac{\alpha_1}{\alpha_3}\mathbf{\Delta S}, \tag{43d}$$

where

$$\tilde{U} \equiv \frac{\mathrm{d}\ln g}{\mathrm{d}\ln r} + 2, \qquad \tilde{V} \equiv \frac{\rho g r}{p} = -\frac{\mathrm{d}\ln p}{\mathrm{d}\ln r}, \tag{44}$$

$$\alpha_1 \equiv \mu/p, \qquad \alpha_2 \equiv \Gamma - \frac{2}{3}\frac{\mu}{p}, \qquad \alpha_3 \equiv \Gamma + \frac{4}{3}\frac{\mu}{p}.$$

The terms Γ and α_4, and the source term ΔS depend on the type of perturbation. In the case where the perturbations are due to a lateral composition gradient $\Delta\mu_\mathrm{e}$, the derivatives in equation (34) are carried out at constant composition μ_e, and we have

$$\Gamma = \left.\frac{\partial\ln p}{\partial\ln\rho}\right|_{\mu_\mathrm{e}}, \qquad \alpha_4 = 0, \qquad \Delta S = \left.\frac{\partial\ln p}{\partial\ln\mu_\mathrm{e}}\right|_\rho \frac{\Delta\mu_\mathrm{e}}{\mu_\mathrm{e}}. \tag{45}$$

On the other hand, in case of the δT source term, the perturbations in equation (35) are at constant temperature, so

$$\Gamma = \left.\frac{\partial\ln p}{\partial\ln\rho}\right|_T, \qquad \alpha_4 = \left.\frac{\partial\ln p}{\partial\ln T}\right|_\rho \frac{\mathrm{d}\ln T}{\mathrm{d}\ln r}, \qquad \Delta S = \left.\frac{\partial\ln p}{\partial\ln T}\right|_\rho \frac{\delta T}{T}. \tag{46}$$

We describe how to compute the various thermodynamic derivatives in the above equations in Appendix A.

Except for the terms involving α_4 and ΔS, which we have highlighted by writing them in boldface, equations (43) are the same as the zero-frequency limit of equations 13(a)–(d) in McDermott et al. (1988). However, in the case of adiabatic pulsations considered by McDermott et al., one writes $\Delta p = (\partial p/\partial\rho)|_\mathrm{s}\Delta\rho$, where the partial derivative is taken at constant entropy. In this case, there are no source terms ΔS, no terms involving the temperature gradient $\mathrm{d}T/\mathrm{d}r$, and Γ is just the adiabatic index $\Gamma_1 \equiv (\mathrm{d}\ln p/\mathrm{d}\ln\rho)_\mathrm{s}$. The ΔS source term in equation (43) arises from the fact that our perturbations (equations 34 or 35) involve an explicit change in composition as well as a change in density. In addition, our Γ term is defined differently from McDermott et al., and depends on the type of perturbation. Consequently, our terms α_2 and α_3, defined in equation (44), are also different from McDermott et al.

Because equations (43) are just linear equations with an inhomogeneous forcing term ΔS proportional to $\Delta\mu_\mathrm{e}$ or δT, it is clear that the resulting quadrupole moment is linear in $\Delta\mu_\mathrm{e}$ or δT, respectively. For the δT perturbations, the coefficient $(\partial\ln p/\partial\ln T)|_\rho$ in ΔS vanishes except near capture boundaries, and so the total Q_{22} for the NS is just the sum of the Q_{22}s generated by each capture layer individually. In Sections 4.3 and 5 we are therefore justified in looking at solutions for a single capture layer, since multiple capture layers can be dealt with by superposition.

4.2 Boundary conditions and solution methods

The solid crust lies between a liquid ocean and a liquid core. In the liquid, $\alpha_1 = 0$ and $\alpha_2 = \alpha_3 = \Gamma$. By integrating equations (43) across the crust–ocean boundary at $r = r_\mathrm{top}$, and the crust–core boundary at $r = r_\mathrm{bot}$, it is easy to see that z_1, z_2 and z_4 (i.e., the radial displacement ξ_r, and tractions $\Delta\tau_{rr}$ and $\Delta\tau_{r\perp}$) must be continuous when going from the crust to a liquid. On the other hand, it follows from equation (43c) that z_3 (the transverse displacement $\xi_\perp$) is allowed to have an arbitrary discontinuity at r_top and r_bot. These connection conditions, however, require the knowledge of ξ_r, $\Delta\tau_{rr}$ and $\Delta\tau_{r\perp}$ in the liquid parts of the NS. We now show how to use physical considerations to remove this requirement.

For static solutions with $l \neq 0$, the Eulerian pressure perturbation $\delta p(r)Y_{lm}$ must be zero everywhere in the liquid parts of the star, since a non-zero δp would lead to a horizontal pressure gradient in the fluid $\delta p(r)\nabla_a Y_{lm}$, which would (in the absence of counterbalancing shear stresses or perturbations of the gravitational field) cause the fluid to flow. Hence, at a liquid-crust boundary, we have $\Delta\tau_{rr}(\mathrm{crust}) = -\Delta p(\mathrm{liquid}) = \rho g\xi_r$. Therefore, at r_top and r_bot, the Eulerian $\delta\tau_{rr} = 0$. Using this, along with the constraint that $\delta\tau_{r\perp}$ must vanish in the fluid (inviscid fluid cannot support shear stresses) one arrives at the following boundary conditions (in agreement with McDermott et al. 1988):

$$z_2 = \tilde{V}z_1, \qquad z_4 = 0. \tag{47}$$

Note that the above boundary conditions do not require the knowledge of displacements and tractions in the liquid parts of the star.

Equation (47) assumes that there is no density discontinuity at the solid–liquid boundary. However, at the interface between the crust and the ocean there may be a discontinuity $(\rho_\mathrm{s} - \rho_\mathrm{l})/\rho \sim 5\times10^{-5}$ (where ρ_s and ρ_l are densities of solid and liquid at the interface) arising from the latent heat of melting of the crust. There may also be a density jump of a few per cent associated with a phase transition between the inner crust and the core of the NS (Pethick & Ravenhall 1995; Pethick, Ravenhall & Lorenz 1995). When there is a density discontinuity, the boundary condition at the edge of the solid is modified to

$$z_2 = \tilde{V}\frac{\rho_\mathrm{l}}{\rho_\mathrm{s}}z_1, \qquad z_4 = 0. \tag{48}$$

Of course, equation (47) is just a special case of equation (48), where $\rho_\mathrm{s} = \rho_\mathrm{l}$ at the interface.

Thus we have a system of four ODEs with four boundary conditions (two at each boundary), with non-zero source terms in the interior region. The system can be solved in any number of standard ways. For example, one can choose the values of z_1 and z_3 at the top of the crust, compute z_2 and z_4 from the boundary conditions, then integrate to the bottom of the crust (using a Runge–Kutta-type algorithm) and calculate the residuals of the two boundary conditions there. Then one can use a two-dimensional Newton's method to find appropriate starting values z_1 and z_3. In practice, we found this method to be *unstable*. On the other hand, we find that a Henyey-type relaxation algorithm (as described in Press et al. 1992) converges very reliably. However, round-off errors can cause trouble if the relaxation mesh is not fine enough and uniform, as already noted.

Given the solutions of equations (43), the perturbed multipole moments Q_{lm} are computed in terms of the z_i variables by using equation (1),

$$Q_{lm} = l\int_{r_\mathrm{bot}}^{r_\mathrm{top}}[z_1 + (l+1)z_3]r^{l+2}\rho\,\mathrm{d}r - (r^{l+3}\rho z_1)|_{r_\mathrm{bot}}^{r_\mathrm{top}}, \tag{49}$$

where r_bot and r_top are the bottom and top of the crust, respectively. If there is a density discontinuity at the crust–core

Downloaded from https://academic.oup.com/mnras/article-abstract/319/3/902/1075833 by California Institute of Technology user on 19 May 2020

or the crust–ocean interface, then ρ in the boundary term of (49) is replaced by ρ_l. Since the calculation of the quadrupole moments involves subtracting two large numbers to get a small number, it is useful to have an independent accuracy check. An alternative expression for the quadrupole moment is derived by finding $\delta\rho$ from equation (37), integrating it using equation (1), using the boundary conditions and carrying out substantial algebra to show

$$Q_{lm} = -\int_{r_{\rm bot}}^{r_{\rm top}} \frac{1}{\tilde{V}} \left\{ l(l+1)z_4 - 2\alpha_1 \left[2\frac{\mathrm{d}z_1}{\mathrm{d}\ln r} + l(l+1)z_3 \right] + (l+4-\tilde{U})(z_2 - \tilde{V}z_1) \right\} r^{l+2}\rho\,\mathrm{d}r. \quad (50)$$

Unlike equation (49), this expression for the multipole moment remains unchanged even when there are density jumps at solid–liquid interfaces. In practice, we refine our solutions to equations (43) until Q_{lm} computed from equations (49) and (50) differ fractionally by less than 10^{-6}.

Since the crust is geometrically thin, one may wonder if accurate results may be obtained by adopting a plane-parallel approximation, i.e., neglecting non-sphericity of the crust. In this case, the radial momentum balance equation is

$$\mathrm{i}k\delta\tau_{r\perp} + \frac{\mathrm{d}}{\mathrm{d}r}\delta\tau_{rr} = \delta\rho g, \quad (51)$$

where the lateral (x) dependence of all perturbed quantities is $\mathrm{e}^{\mathrm{i}kx}$ and $k \sim \sqrt{l(l+1)}/R$ is the transverse wave number. Integrating the above equation from $r_{\rm bot}$ to $r_{\rm top}$ and using the boundary condition $\delta\tau_{rr} = 0$, we get a plane-parallel estimate for the quadrupole moment,

$$Q_{22}^{\rm pp} = R^4 \int \frac{\mathrm{i}k\delta\tau_{r\perp}}{g}\mathrm{d}r = l(l+1)R^3 \int \frac{1}{\tilde{V}} z_4 \rho r\,\mathrm{d}r. \quad (52)$$

Compare the above expression to equation (50). In the plane-parallel case, only the $\delta\tau_{r\perp}$ component of the shear stress contributes to the quadrupole moment. As it turns out, the $\delta\tau_{rr}$ component of the shear stress is much larger (see Section 4.3). In other words, the crust holds up the majority of the quadrupole moment by stretching like a spring with a weight attached to it, rather than bending like a crossbar. In the plane-parallel case, this vertical motion of the crust is fully taken into account. However, because of the artificial symmetry of equation (51), the dominant stress term does not enter in the plane-parallel expression for the quadrupole moment, equation (52). Quadrupole moments computed using the plane-parallel approximation (equation 52) underestimate the values computed using full spherical symmetry (i.e., from equations 49 or 50) by large factors ($\sim$10).

4.3 The nature of the solutions

We now describe the solutions to our crustal perturbation equations, both for the case where the capture layers are deformed due to local temperature variations δT, and for the case where the perturbations are sourced by a radially uniform composition perturbation $\Delta\mu_{\rm e}/\mu_{\rm e}$.

Figs 10, 11 and 12 show the response of the crust to a temperature perturbation $\delta T(r)\mathrm{Re}\{Y_{22}\}$ acting on shallow (threshold energy $Q = 23$ MeV), medium ($Q = 42.4$ MeV) and deep ($Q = 95$ MeV) capture layers, respectively. The background model has a normal core, and the accretion rate is $0.5\dot{M}_{\rm Edd}$. The background thermal structure is shown in Fig. 7, and $\delta T(r)$ is plotted in Fig. 8. The top two panels show the vertical (ξ_r) and horizontal ($\xi_\perp$) Lagrangian displacements of the fluid elements in the crust, as defined in equation (36). The next two panels show the Lagrangian components of the perturbed stress tensor, $\Delta\tau_{rr}$ and $\Delta\tau_{r\perp}$, defined in equation (39), while the last panel displays the negative of the source term, $-(\mathrm{d}\ln p/\mathrm{d}\ln T)_\rho \delta T$, defined in equation (46). The response of the crust is qualitatively different in these cases, as we discuss below.

For concreteness about signs, let us focus attention on an angular location in the star where $\mathrm{Re}\{Y_{22}(\theta,\phi)\}$ is positive, and consider a perturbation with positive $\delta T(r)$ at the capture layer. (Figs 10–12 are drawn to reflect this choice.) We imagine drawing, at this (θ,ϕ), a cylindrical tube that extends through the

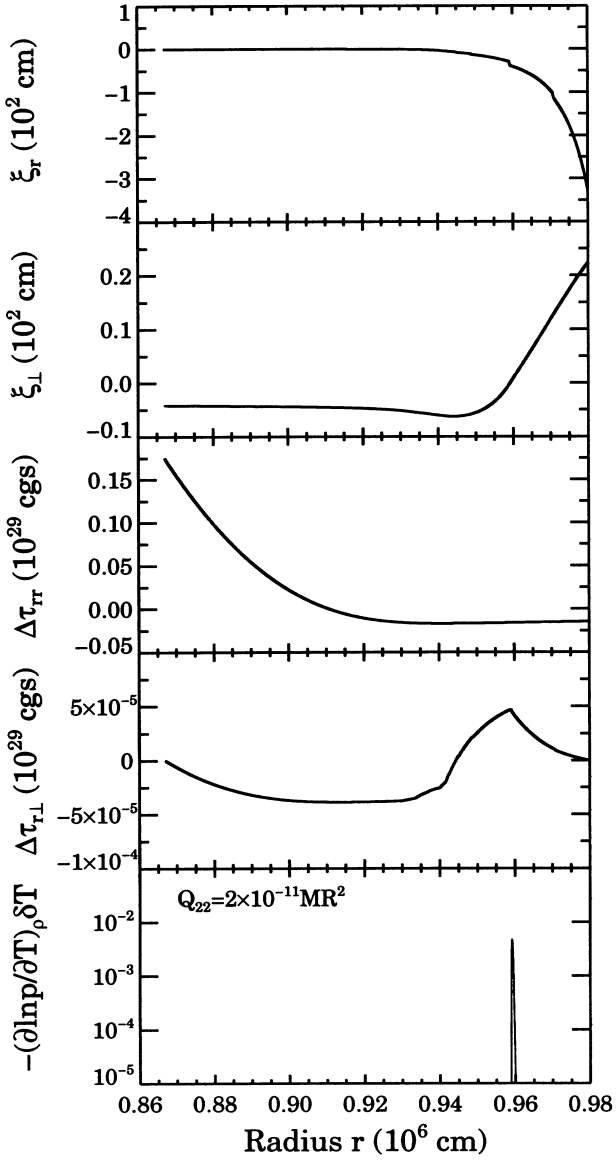

Figure 10. Response of the crust to a temperature perturbation due to an $f_{\rm nuc} = 0.1$ asymmetry of the nuclear heating rate in the crust. The background model has a normal core (gap energy $\Delta = 0$), and the accretion rate is $0.5\dot{M}_{\rm Edd}$. Only one shallow capture layer ($Q = 23$ MeV) is activated. The top two panels show vertical and horizontal Lagrangian displacements, ξ_r and $\xi_\perp$, in metres, and the two middle panels show the stresses, $\Delta\tau_{rr}$ and $\Delta\tau_{r\perp}$, in $10^{29}\,\mathrm{erg\,cm^{-3}}$. The bottom panel shows the negative of the source term, $-(\partial\ln p/\partial T)_\rho\delta T$ (see equation 46 and Appendix A).

Downloaded from https://academic.oup.com/mnras/article-abstract/319/3/902/1075833 by California Institute of Technology user on 19 May 2020

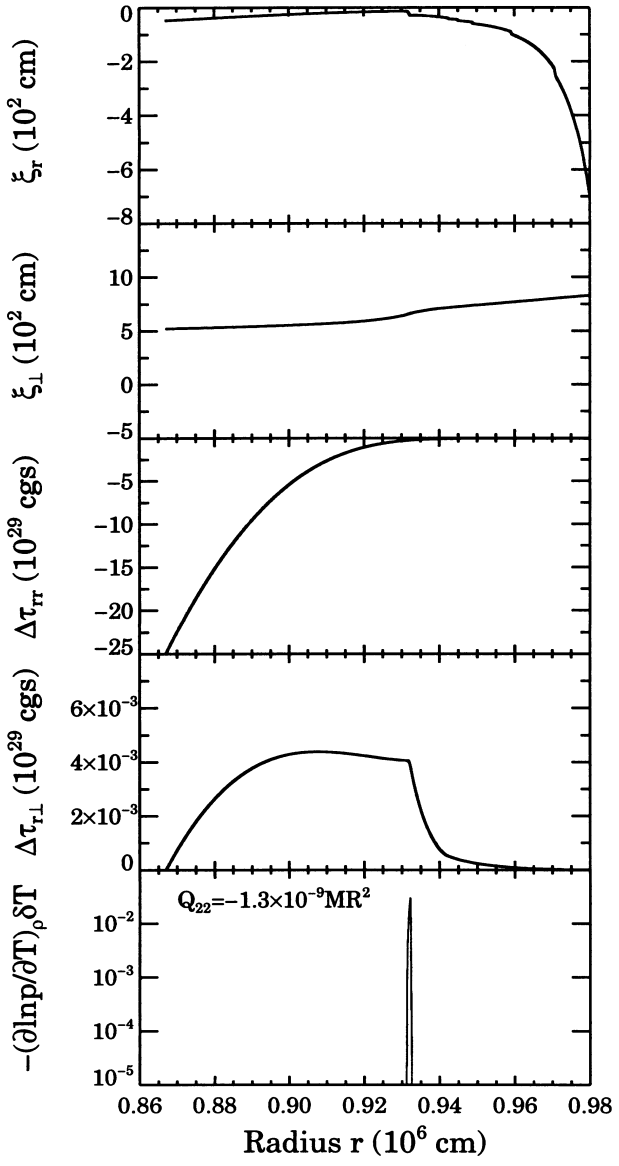

Figure 11. Same as Fig. 10, but for a displacement of a capture layer at intermediate depth, $Q = 42.4$ MeV.

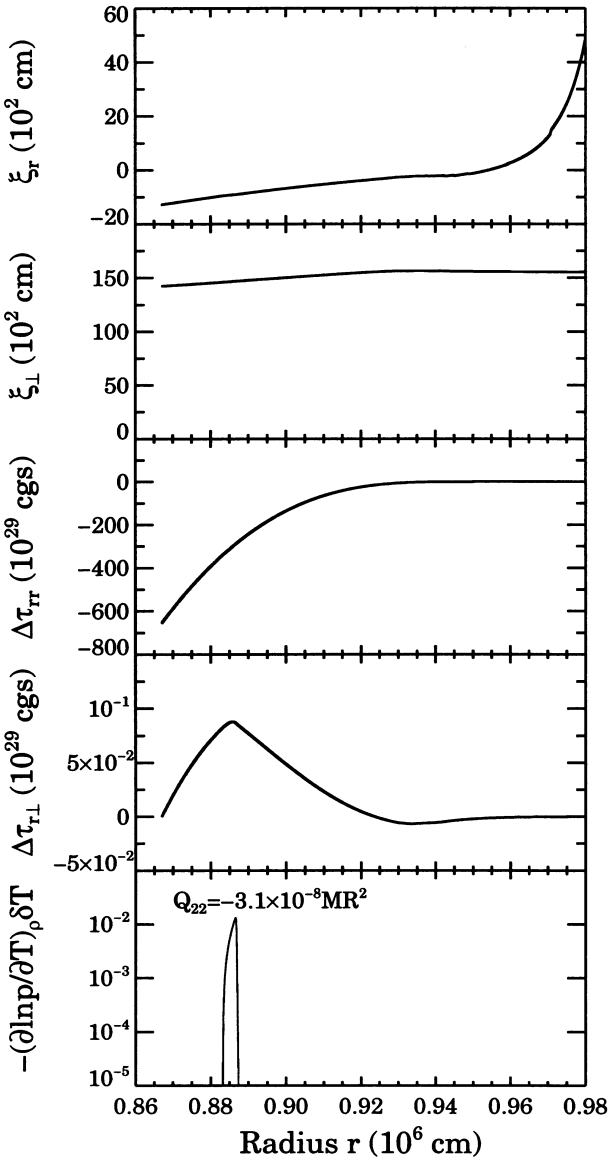

Figure 12. Same as Fig. 10, but for a deep capture layer, $Q = 95$ MeV.

crust and into the fluid on both sides. Since we take δT to be positive at the capture layer, in our tube the e^- captures occur at lower-than-average E_F, which tends to make the capture layer relatively 'underpressured' [i.e., the source term $(d\ln p/dT)_\rho\delta T$ is negative; see the bottom panels of Figs 10–12].

In Figs 10–12 the location of the capture layer, r_{lay}, is identified by a sharp 'kink' in ξ_r (for the deep capture layer shown in Fig. 12, the kink is quite small, but its location is coincident with the extremum of the source term). If the capture layer were infinitely thin, then there would be a discontinuity in ξ_r at that location. This is because we allow changes of composition (i.e., relabelling of fluid elements) at the capture boundary, and so $\xi_r(r_{lay})$ does not indicate the perturbed location of the capture layer.

The kink in ξ_r is easy to understand: $d\xi_r/dr$ is large and negative there, because the crustal matter is vertically compressed around the capture boundary. We can estimate the jump in ξ_r at the capture layer by integrating equation (43a) in a thin region around r_{lay}, where the delta-function-like source term ΔS is dominant and balances $dz_1/d\ln r$. With this approximation, we get

$$\Delta\xi_r|_{r_{lay}} \approx \Upsilon h\frac{\Delta\rho}{\rho}\frac{k_B\delta T}{Q}\frac{d\ln p}{d\ln E_F} = \Delta z_d\frac{\Delta\rho}{\rho}, \quad (53)$$

where h is the scaleheight at the capture layer with threshold energy Q, and $\Delta\rho/\rho$ is the density jump across the capture layer.

Compression of the capture boundary occurs in all solutions, regardless of the capture threshold Q. Most other qualitative features of the solution depend on whether the capture boundary occurs at relatively low density, $Q \lesssim 25$ MeV, or high density, $Q \gtrsim 40$ MeV.

Consider first the case of a deep capture layer, shown in Fig. 12. This is the most interesting case, since it generates the largest Q_{22}. To understand the solution, we find it helpful to picture the displacements as built up in a series of 'steps.' (Of course, the implied time-ordering is fictitious; the 'steps' are simply an imaginative device to guide intuition.) Due to the 'extra' e^- captures in our imaginary cylindrical tube, the capture layer starts

Downloaded from https://academic.oup.com/mnras/article-abstract/319/3/902/1075833 by California Institute of Technology user on 19 May 2020

out 'underpressured.' Step I is vertical adjustment of the crust to compress the capture layer and de-compress the crust $[\mathrm{d}(r^2\xi_r)/\mathrm{d}r > 0]$ above and below it. In effect, the crust adjusts vertically to 'share' the 'underpressure.' After step I, the entire crust in the tube is relatively underpressured. Hence, in step II, the crustal matter gets 'pushed in from the sides' at all depths. One can see this behaviour in our solution: in Fig. 12, $\xi_\perp$ is positive everywhere, so the divergence of $\xi_\perp(r)\nabla^a Y_{22}$ is negative (see equation 41). This convergence of solid matter in from the sides causes the crust to be 'thicker than average' in the tube; the bottom of the crust is pushed down and the top pushed up. Finally, step III: the bulging out of the crustal boundaries displaces the fluid in the ocean and the core, pushing it out of the tube.

In summary, for deep captures, solid (elastic) matter is pushed into the tube from the sides, while liquid in the ocean and the core is pushed out. The centre of mass of the tube also sinks somewhat. Moreover, it turns out that *more fluid goes out of the tube than solid comes in*. Both of these effects – the net loss of mass from the tube and the fact that the tube's centre of mass sinks – contribute to Q_{22} with a negative sign. Therefore, not only is the resulting Q_{22} smaller than the fiducial estimate, $Q_{\rm fid}$, but it has the opposite sign! (Recall that in the picture behind the fiducial estimate, matter simply comes in from the sides in response to the 'underpressure' of the capture layer. However, the actual response of the crust is much more complicated, and numerical solutions were crucial to reforming our intuition.)

In our deep-capture solution, ξ_r is of order $\sim$10 m and $\xi_\perp \sim$ 100 m (for accretion rate of $0.5\dot{M}_{\rm Edd}$), so the displacements are rather large. This is clearly due to the smallness of the crust's shear modulus relative to pressure. Note also that the shear stress term $\delta\tau_{r\perp}$ is sizeable over a region roughly $\sim$1 km thick. Thus, despite the fact that the capture boundaries are rather thin (several meters), the induced stresses are 'shared' by a sizeable fraction of the crust. This is important for the consistency of our approach. If we had found that all the shear stresses were concentrated near the capture layer, then they would certainly be large enough there to crack the crust, invalidating our solution. Even given that the stresses are shared by a large fraction of the crust, it is still a serious question whether the NS can sustain them; we address this question in detail in Section 6.

We consider next solutions sourced by a uniform $\Delta\mu_{\rm e}/\mu_{\rm e}$, since they are extremely similar to deep-capture solutions, as seen evident from comparing Figs 12 and 13. Again, to fix signs, take $\Delta\mu_{\rm e}/\mu_{\rm e}$ to be positive inside our imaginary tube. The perturbation corresponds to the crust inside the tube being 'a little underpressured everywhere.' Compare this to the deep-capture layer case, where the crust starts out 'very underpressured in a thin layer', but, in step I (described above), adjusts vertically to 'share the underpressure.' That is, in the deep capture layer case the crust adjusts vertically to resemble the uniform $\Delta\mu_{\rm e}/\mu_{\rm e}$ case. Of course, one can also imagine building up a smooth source term from a sum of delta-function-like sources. Since the deep capture solutions all have a similar profile, and since our equations are linear, the solution sourced by a uniform $\Delta\mu_{\rm e}/\mu_{\rm e}$ must share that profile.

We see from Fig. 10 that the behaviour for shallow capture layers is qualitatively quite different. In that case the crust above the capture layer sinks and compresses (the opposite of what we find for deep capture layers). The crust below the capture layer also sinks and compresses, but less so. Crust and fluid enter the tube above the capture layer and get pushed out of the tube below the capture layer. We find that the net effect is a positive contribution to Q_{22}, though a much smaller one than the fiducial estimate.

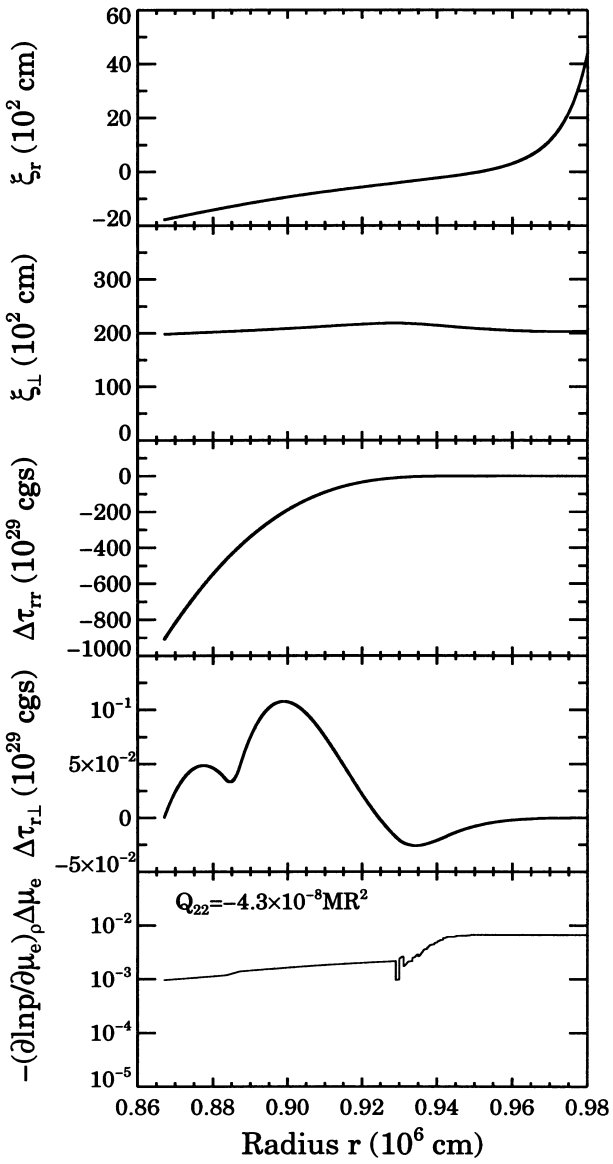

Figure 13. Response of the crust to a smooth composition variation, $\Delta\mu_{\rm e}/\mu_{\rm e} = 5\times10^{-3}$, throughout the crust. The top two panels show vertical and horizontal Lagrangian displacements, ξ_r and $\xi_\perp$, in metres, and the two middle panels show the stresses, $\Delta\tau_{rr}$ and $\Delta\tau_{r\perp}$, in $10^{29}\,\mathrm{erg\,cm^{-3}}$. The bottom panel shows the negative of the source term, $-(\partial\ln p/\partial\mu_{\rm e})_\rho\Delta\mu_{\rm e}$ (see equation 45).

We see that for fixed δT, the contribution of a capture layer to Q_{22} changes sign as one goes from shallow to deep layers. There is an intermediate regime, $Q \sim$ 25–35 MeV, where the displacements produce almost no contribution to the star's quadrupole moment. This does not mean that the effects from shallow capture layers in the neutron star will mostly cancel the effects from the deep ones; contributions to Q_{22} from deep capture layers are roughly two orders of magnitude larger than those from shallow layers, so the deep ones dominate. A complete description of how Q_{22} varies with the capture depth and other variables is presented in Section 5.

Downloaded from https://academic.oup.com/mnras/article-abstract/319/3/902/1075833 by California Institute of Technology user on 19 May 2020

5 GENERAL PROPERTIES OF QUADRUPOLES FROM CAPTURE BOUNDARIES

In this section we show our results for the NS quadrupole moment Q_{22}, and explain how Q_{22} scales with physical parameters, such as $\dot{M}$. Our results basically validate the original mechanism put forward by Bildsten (1998a): small temperature perturbations in the deep crust can easily generate the Q_{22} needed for GWs to balance accretion torque. We defer to Section 6 the question of whether the crust can actually sustain such large stresses without cracking or yielding.

5.1 The dependence of Q_{22} on the neutron star parameters

Fig. 14 shows the Q_{22} resulting from a single capture layer (at e^- capture threshold energy Q). The thermal perturbation is due to a local nuclear heating rate that is assumed to vary laterally by 10 per cent (i.e., $f_{\rm nuc} = 0.1$). Filled squares are for the background model with a superfluid core (gap energy $\Delta = 1$ MeV), and open diamonds are for the model with a normal core. The two models have the same background hydrostatic structure and accretion rate ($\dot{M} = 0.5\dot{M}_{\rm Edd}$).

Clearly, deep capture layers generate a much larger Q_{22} than shallow ones. We understand this as follows. If we ignore the vertical readjustment of the crust (as was done by Bildsten 1998a), then a local increase in temperature, δT, increases the local e^- capture rate and causes the location of the capture layer to shift upward by a distance $\Delta z_{\rm d}$, given by equation (13) (see also Fig. 3 and equation A18 in Appendix A). In particular, in the outer crust, where the pressure is supplied by degenerate relativistic electrons,

$$\Delta z_{\rm d}|_{\rm outer\ \ crust} \approx \Upsilon \frac{k_{\rm B}T}{\mu_{\rm e} m_{\rm p} g}\frac{\delta T}{T} = 30\,{\rm cm}\left(\frac{\delta T}{10^7\,{\rm K}}\right)\left(\frac{2}{\mu_{\rm e}}\right), \qquad (54)$$

where $\Upsilon \sim 10$–20 is introduced in equation (12) and defined precisely in Appendix A. When the elastic readjustment of the crust is ignored, the quadrupole is just $Q_{\rm fid} = \Delta\rho \Delta z_{\rm d} R^4$ (Bildsten 1998a; see also Fig. 2 in Section 1.3). In the outer crust, where in each capture layer only two electrons are consumed and no neutrons are emitted, the density jump is just $\Delta\rho/\rho = \Delta\mu_{\rm e}/\mu_{\rm e} = 2/Z$, so

$$Q_{\rm fid} \approx 1.3\times 10^{37}\,{\rm g\,cm^2} R_6^4 \left(\frac{\delta T}{10^7\,{\rm K}}\right)\left(\frac{Q}{30\,{\rm MeV}}\right)^3. \qquad (55)$$

In the inner crust, the capture layer is rather thick, so rather than talk of a 'jump' in density across the boundary, we define the fiducial quadrupole moment as

$$Q_{\rm fid} \equiv \int \frac{\partial \ln \rho}{\partial \ln T}\Big|_{\rm p} \frac{\delta T}{T} \rho r^{l+2}\,{\rm d}r \qquad (56)$$

$$= \Delta z_{\rm d} \int \frac{\Gamma_{\mu_{\rm e}}}{\Gamma_\rho}\frac{{\rm d}\ln \mu_{\rm e}}{{\rm d}r}\rho r^{l+2}\,{\rm d}r, \qquad (57)$$

where Γ_ρ and $\Gamma_{\mu_{\rm e}}$ are defined in Appendix A; i.e., we integrate the Lagrangian density perturbation $\Delta\rho$ under the condition of $\Delta p = 0$ and $\xi_r = 0$ (no elastic readjustment of the crust; see equation 35). In going from equation (56) to equation (57) we used equations (A10), (A14) and (A18) from Appendix A.

In the inner crust the dependence of $\Delta z_{\rm d}$ and $Q_{\rm fid}$ on depth is more complicated than in the outer crust because of the variation in number of electrons captured and neutrons emitted in each capture layer (see Fig. 3). Also, while $Q_{\rm fid}$ given by equation (56) does increase with depth for a fixed δT, because of the radial structure of the temperature perturbations for fixed $f_{\rm nuc}$ or $f_{\rm comp}$, $Q_{\rm fid}$ must decrease near the very bottom of the crust. The high thermal conductivity of the core forces $\delta T \approx 0$ at the crust–core boundary (see Fig. 8). This explains the decrease in the induced Q_{22} very close to this boundary seen in Fig. 14.

Fig. 14 shows that a *single* capture layer near the bottom of the crust generates $Q_{22} \approx 6\times 10^{37}\,{\rm g\,cm^2}$ (f/0.1), where f is either $f_{\rm nuc}$ or $f_{\rm comp}$. There will be more than one capture layer near the bottom of the crust, and so the full Q_{22} for the NS is proportionately higher. The numbers we quote will always be for a single capture layer, so this multiplicative factor must be kept in mind.

Although the scaling of the fiducial estimate, $Q_{\rm fid}$, is helpful for our understanding, it neglects an essential piece of physics. As described in Section 4.3, the crust prefers to sink in response to the shift in capture layers, and this reduces the actual quadrupole moment significantly below the fiducial estimate. In Fig. 15 we plot this 'sinking penalty', $Q_{22}/Q_{\rm fid}$, for the same model as in Fig. 14. As one can see, the penalty is quite large ($\sim$20–50) for the shallow capture layers ($Q \lesssim 40$ MeV), but is only $\sim$5–10 for the capture layers in the deep crust. The fact that the sinking penalty decreases with greater depth, while $Q_{\rm fid}$ increases, means that deep capture layers are the dominant contributors to Q_{22}. We find that transverse temperature contrasts of 10^6–10^7 K are sufficient to generate $Q_{22} \sim 10^{37}$–$10^{38}\,{\rm g\,cm^2}$. This is much smaller than the $\sim 10^8$ K contrast originally required by Bildsten (1998a) for the shallow capture layers.

In Fig. 16 we explore the effects of the magnitude of the shear modulus μ, the physical extent of the crust, and the possible density discontinuity at the crust–core interface. In order to simplify the discussion, we computed the quadrupole moments resulting from a fixed shift $\Delta z_{\rm d} = 100$ cm of the capture layers, rather than from a temperature perturbation δT that has a non-trivial radial dependence (see Appendix A for a detailed discussion). Filled squares show Q_{22} for the standard model used throughout this section. The Q_{22} values are different from

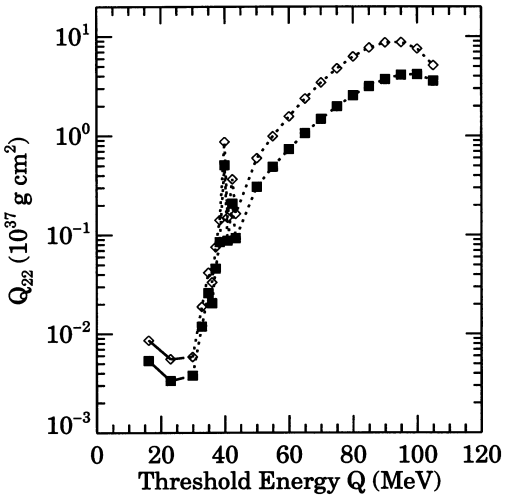

Figure 14. Quadrupole values for a single capture layer, sourced by the temperature perturbations computed as described in Section 3. The horizontal axis gives the threshold energy of the reaction. Filled squares correspond to model S (superfluid core), while open diamonds correspond to model N (normal core). The accretion rate is $0.5\dot{M}_{\rm Edd}$ in all cases. The absolute value of Q_{22} is plotted; however, the sign of it is positive where the lines are solid, and negative where they are dotted.

Downloaded from https://academic.oup.com/mnras/article-abstract/319/3/902/1075833 by California Institute of Technology user on 19 May 2020

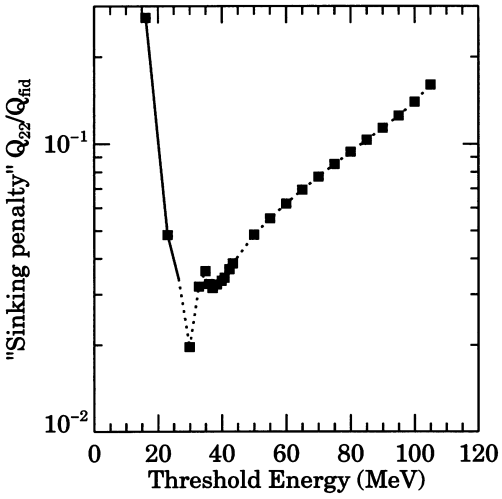

Figure 15. The 'sinking penalty' for the thermal perturbations at $0.5\dot{M}_{\rm Edd}$. The absolute value is plotted; however, the sign of it is positive where the lines are solid, and negative where they are dotted.

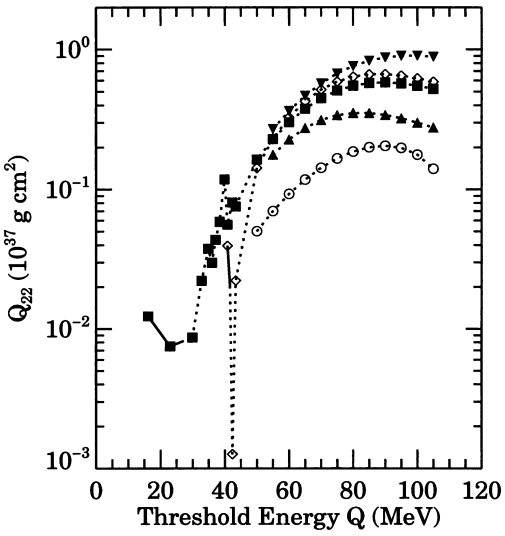

Figure 16. Quadrupole values for a single capture layer, with $\Delta z_{\rm d} = 100$ cm plotted as function of the threshold energy of the reaction. The lines marked with filled squares correspond to the full crust, while the open diamonds represent the case where the crust is melted around neutron drip. The line marked with upward-pointing triangles corresponds to the crust with the shear modulus μ artificially decreased by a factor of 2 from the value given by equation (A1), while the line marked with downward-pointing triangles corresponds to the case where μ is 2 times larger than the value from equation (A1). Finally, the line marked with open circles corresponds to the case where there is a 5 per cent density jump at the crust–core boundary (i.e., $\rho_{\rm l}/\rho_{\rm s} = 1.05$). The absolute value of Q_{22} is plotted; however, the sign of it is positive where the lines are solid, and negative where they are dotted.

those in Fig. 14, since in Fig. 16 the perturbations are normalized to yield the same vertical shift $\Delta z_{\rm d}$ of the capture layers regardless of its position in the star.

As shown by Brown (2000), at high $\dot{M}$ the energy input from crustal nuclear reactions can melt the crust near neutron drip. In this case there will be a liquid layer in the middle of the crust, and our outer elastic boundary condition needs to be applied there. The line marked with open diamonds in Fig. 16 shows Q_{22} as function

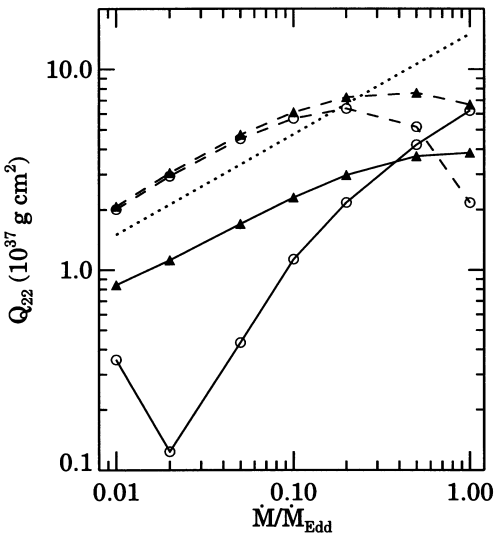

Figure 17. The quadrupole moment Q_{22} due to a single capture layer with threshold energy $Q = 95$ MeV. Solid lines denote the results for the model with a superfluid core (gap energy $\Delta = 1$ MeV), while dashed lines denote the values for the model with a normal core ($\Delta = 0$). Lines marked with open circles are for the quadrupole moment sourced by the composition perturbations, $f_{\rm comp} = 0.1$, while lines marked with filled triangles denote the quadrupoles sourced by the variation in the local heating of the crust, $f_{\rm nuc} = 0.1$. Finally, the dotted line is the relation given by equation (4), i.e., the quadrupole moment necessary for spin equilibrium at $\nu_{\rm s} = 300$ Hz as a function of $\dot{M}$.

of capture layer depth for this case. The quadrupole moment due to deep capture layers is virtually unaffected (differs by ~10 per cent) by the presence of a melted layer near neutron drip.

The lines marked with triangles survey the dependence of Q_{22} on the crust shear modulus μ. Doubling μ compared to the canonical value roughly doubles Q_{22} (the line marked with downward-pointing triangles), and halving μ (line marked with upward-pointing triangles) roughly halves Q_{22}. This is consistent with the general dependence of the quadrupole moment on the shear modulus, as derived in Section 6.

Throughout this paper we have assumed that the density is continuous across the crust–core boundary. However, this is not certain (see Pethick & Ravenhall 1995 for a review), as many models for the transition contain density jumps. Though gravitationally stable, this density discontinuity adds to the restoring force when the crust pushes down into the core. The line marked with open circles shows Q_{22} for an NS model where the liquid just inside the core is 5 per cent denser than the crust immediately above it (i.e., $\rho_{\rm l}/\rho_{\rm s} = 1.05$). In this case, the rippled surface of the crust–core boundary provides some extra restoring force that reduces Q_{22}.

5.2 Dependence of Q_{22} on accretion rate, and the overall picture

We now turn our attention to the scaling of Q_{22} with $\dot{M}$. This behaviour is important for comparing our results to the observed distribution of NS spin frequencies in LMXBs, since in our picture the close similarity in spin frequencies (all ~300 Hz) over a large range in $\dot{M}$ implies that Q_{22} scales (roughly) like $\dot{M}^{1/2}$. In Fig. 17 we show the Q_{22} induced by 10 per cent perturbation in nuclear heating ($f_{\rm nuc} = 0.1$, lines marked with filled triangles) and by

Downloaded from https://academic.oup.com/mnras/article-abstract/319/3/902/1075833 by California Institute of Technology user on 19 May 2020

10 per cent perturbations in Z^2/A ($f_{\rm comp} = 0.1$, lines marked with open circles), as a function of $\dot{M}$. Solid lines correspond to models with a superfluid core, while dashed lines indicate models with a normal core. The dotted line displays, as a function of $\dot{M}$, the quadrupole required for spin equilibrium at $\nu_{\rm s} = 300\,{\rm Hz}$ (see equation 4).

It should be clear from this figure that the Q_{22} generated by a single capture layer can easily account for the spins of the accreting neutron stars. Given that there are several capture layers in the deep crust, the required asymmetry in either the heat sources or compositions is thus proportionately lower than 10 per cent. Hence, despite the reduction in Q_{22} (below $Q_{\rm fid}$) due to the vertical readjustment of the crust, the basic mechanism of electron capture induced density jumps can indeed account for the spin rates. It is also evident from Fig. 17 that the case of superfluid core with δT sourced by lateral composition variations $f_{\rm comp}$ (solid line marked with circles) can be eliminated as a viable source of the quadrupole moment, especially at low accretion rates, as $f_{\rm comp}$ would need to be close to unity.

Remarkably, for accretion rates $\dot{M} \lesssim 0.2\dot{M}_{\rm Edd}$, Q_{22} for a constant $f_{\rm nuc}$ or $f_{\rm comp}$ scales as $\dot{M}^{1/2}$, i.e., in the same way as the required quadrupole moment, equation (4). At high accretion rates, the temperature profile in the inner crust is set by the balance of the heat input due to compression-induced nuclear reactions near neutron drip and neutrino emission from the crust and the core (Brown 2000). On the other hand, at low accretion rates, the effect of heating near neutron drip and crustal bremsstrahlung is diminished, which leads to a more direct dependence of the temperature profile on the accretion rate and the outer boundary temperature.

As we said before, the NS's total Q_{22} depends on the magnitude of the asymmetry (i.e., $f_{\rm nuc}$ or $f_{\rm comp}$) and the number of capture layers, i.e., the curves showing Q_{22} for different models in Fig. 17

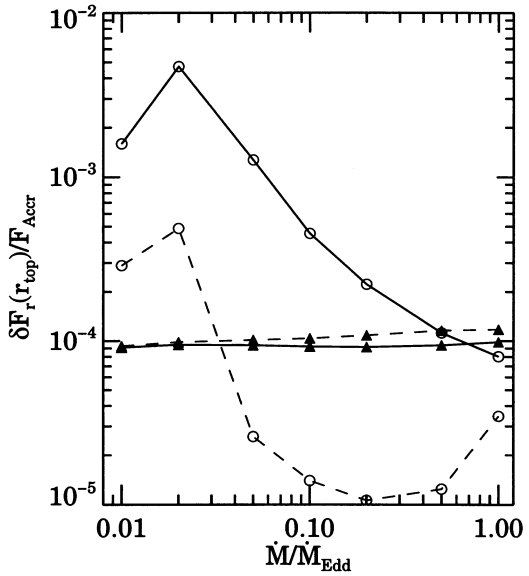

Figure 18. The amplitude of flux perturbations δF_r at the top of the crust that corresponds to a Q_{22} due to a *single* capture layer given by equation (4), i.e., a quadrupole moment that ensures equilibrium $\nu_{\rm s} = 300\,{\rm Hz}$ at a given accretion rate. The legend is same as in Fig. 17. δF_r is proportional to the number of capture layers contributing to Q_{22}, so with many capture layers in the deep crust the required δF_r is reduced accordingly. According to equation (4), $\delta F_r \propto \nu_{\rm s}^{-5/2}$, i.e., for equilibrium spin of 600 Hz the estimated δF_r is reduced by a factor of 5.

can be shifted up or down by overall factors. Despite this uncertainty in the pre-factor of $Q_{22}(\dot{M})$, our calculation has no uncertain parameters that would alter the calculated *scaling* of Q_{22} with $\dot{M}$ for an $\dot{M}$-independent $f_{\rm nuc}$ or $f_{\rm comp}$.

As discussed in Section 3.3, the thermal perturbation calculations also predict a modulation in the X-ray flux exiting the NS crust. The temperature perturbations in the deep crust that displace the capture layers also give rise to a lateral variation of the flux at the NS surface. These hot and cold spots, when moving in and out of the view of the observer due to the rotation of the NS, generate a modulation in the persistent emission.

The perturbed flux δF_r arising from either $f_{\rm nuc}$ or $f_{\rm comp}$ equal to 10 per cent was shown in Fig. 9 of Section 3.3. However, as we see in Fig. 17, a 10 per cent $f_{\rm nuc}$ or $f_{\rm comp}$ perturbation in a star with a normal core produces Q_{22} from a single capture layer that is too large at low $\dot{M}$ and too small at high $\dot{M}$. If the equilibrium spin frequency is *exactly* independent of $\dot{M}$, then for our deformed capture layer model to accord with these observations, $f_{\rm nuc}$ or $f_{\rm comp}$ must vary with $\dot{M}$.

In Fig. 18 we show δF_r, normalized by the accretion flux $F_{\rm A} \approx 200\,{\rm MeV}/4\pi R^2/{\rm accreted\ baryon}$, under the assumption that the Q_{22} due to a single capture layer at $Q = 95\,{\rm MeV}$ is exactly that needed to set $\nu_{\rm s} = 300\,{\rm Hz}$ (equation 4). In other words, we adjust $f_{\rm nuc}$ and $f_{\rm comp}$ as a function of $\dot{M}$ to get the required Q_{22}. The actual flux asymmetry in the NS is, of course, lower than that shown in Fig. 18 by the factor of (roughly) the number of deep capture layers, as additional capture layers in the deep crust will increase the quadrupole moment for the same $\delta T/T$.

The ratio $\delta F_r/F_{\rm A}$ shown in Fig. 18 presumes that accretion is steady. However, there are systems, such as NS transients, that accrete only episodically, with time-averaged accretion rates $\langle\dot{M}\rangle \lesssim 10^{-11}\,{\rm M}_\odot\,{\rm yr}^{-1}$. When accretion halts in these systems, the thermal emission from the surface should be visible directly (Brown et al. 1998). Hence, in quiescence, the modulation is $\delta F_r/F(r_{\rm top}) \sim 10^{-2}(f/10\,{\rm per\ cent})$, rather than $\delta F_r/F_{\rm A}$.

Therefore our thermal calculations lead us to predict a certain level of modulation in the X-ray luminosity of LMXBs. Can this modulation be detected? Possibly. We have not considered how the ocean would respond to such lateral flux asymmetry emerging from the crust. One could imagine transverse flows being generated from the resulting transverse temperature gradients. Presuming that the flux at the NS photosphere maintains the asymmetry of the flux at the top of the crust, it can provide a critical window on to processes in the deep crust. The bright source Sco X-1 would be a good place to start, as it has the highest count rate. The best current limit on a coherent pulse from Sco X-1 is $\lesssim$1 per cent (Vaughan et al. 1994). Our capture-layer mechanism for quadrupole moment generation might then be tested by observations that are accessible today, without having to wait 5–10 years for gravitational wave detectors to reach the requisite sensitivity. In addition to the excitement of finding a coherent pulse in the X-rays, such discovery would *substantially* reduce the parameter space that would need to be searched for the gravitational wave detection.

6 SHEAR STRENGTH OF THE CRUST AND THE MAXIMUM POSSIBLE CRUSTAL QUADRUPOLE

In the previous sections we described how lateral pressure gradients due to composition asymmetries can deform an NS

Downloaded from https://academic.oup.com/mnras/article-abstract/319/3/902/1075833 by California Institute of Technology user on 19 May 2020

crust, and computed the resulting quadrupole moments. However, there is a maximum degree of deformation that a crust can sustain, which is set by its yield or breaking strain $\bar{\sigma}_{\max}$. The yield strain places a fundamental limit on Q_{22} of an NS. Unfortunately, yield strains of even terrestrial materials, let alone NS matter, are poorly understood. In Section 6.1 we summarize the current folklore regarding $\bar{\sigma}_{\max}$.

Wavy electron capture layers are a very special way of straining the crust. However, in the absence of strong magnetic fields, a (static) neutron star's quadrupole moment must be generated by shear stresses in the crust, no matter how the stresses arise. Imagine somehow turning off the crust's shear modulus. Then the matter equations are simply the Euler equations for a perfect fluid, and then Q_{22} must be zero in static equilibrium. These considerations suggest that there should be an expression for Q_{22} that involves the shear-stress forces only. In Section 6.2 we derive such an expression, equation (64).

Equation (64) allows us to estimate the quadrupole moment that results from a 'typical' strain amplitude. It also gives us an upper limit on Q_{22}, set by the yield stress (derived in Section 6.3). Given the tremendous uncertainty in $\bar{\sigma}_{\max}$, this formula allows us to lump all our ignorance into a single parameter. Note that our expression (64) for Q_{22}, and the resulting upper limit (69), do *not* depend on several other assumptions made in the rest of this paper: that the 'non-stressed' state of the crust is spherical, that the stress–strain relation is in the linear regime, or that the perturbation is sourced by temperature or composition gradients. It applies regardless of the crust's detailed evolution, which could have undergone an arbitrary amount of creep or cracking. Of course, our formula does *not* apply when Q_{22} is generated by some force other than shear stresses, such as magnetic fields.

In Section 6.4 we use the formalism developed earlier to evaluate the strain induced in the crust by the wavy e^- capture layers or uniform composition gradients. We compare the strains to the crust's maximum strain level and discuss the implications.

Finally, since the analysis in this paper ignores the self-gravity of the perturbations, in Section 6.5 we estimate the size of the correction when self-gravity is included.

6.1 Maximum strain level for an NS crust

Throughout this paper we have made a simplifying assumption that the response of the crust to the density and pressure perturbations is purely elastic. However, the response of solids to applied stresses is more complicated than that. There are two related issues here. First, solid materials behave elastically only up to some maximum strain $\bar{\sigma}_{\max}$, beyond which they usually either crack or deform plastically. Upon relieving the stress, the solid does not return to its initial shape. Second, even at strains well below the yield strain, a solid that has been strained for a very long time tends to 'forget' its former equilibrium shape; i.e., the equilibrium shape undergoes irreversible relaxation or 'creep.' This behaviour is called viscoelastic: solids respond elastically on short time-scales, while on very long time-scales they behave more like very viscous fluids. As argued in Section 4, we expect that viscoelastic relaxation, while perhaps important to the detailed picture of 'NS mountain-building,', will not drastically change our conclusions about the likely magnitudes of NS crustal deformations. However, the question of the maximum strain that an NS crust can sustain *is* a crucial one for our work, as is the question of what happens when this strain is exceeded.

Yield strains $\bar{\sigma}_{\max}$ of even ordinary materials, let alone NS crusts, are very hard to predict theoretically. For perfect one-component crystals, simple theoretical considerations lead to $\bar{\sigma}_{\max} \sim 10^{-2} - 10^{-1}$ (Kittel 1956). However, the maximum strain of most solids is determined by the motion of dislocations and other defects. Early discussions by Smoluchowski (1970) placed $\bar{\sigma}_{\max}$ of NS crusts in the range of 10^{-2} to 10^{-5} by analogy with a variety of terrestrial materials with chemical and lattice imperfections. Ruderman (1991) puts the maximum strain in the range of 10^{-4}–5×10^{-3}, which implies a large number of cracking events in the lifetime of a spinning-down young pulsar.

Recent breakthroughs in the understanding of the soft-gamma ray repeaters as magnetars may shed some light on our problem as well. Thompson & Duncan (1995) argued that the energy release that powers these events is magnetic in nature, but that the events are triggered by 'cracking' of the crust, which accumulates strain as the magnetic field evolves. The maximum energy of such events implies (in a model-dependent way) that the maximum strain is in the 10^{-3} range. Phenomenological support for the idea that crust cracking is the origin of the bursts comes from the rather striking similarity of the power-law distribution of burst energy with that of terrestrial earthquakes (Cheng et al. 1996).

However, cracking is just one way in which the crust can relieve the applied stress. Smoluchowski & Welch (1970) argued that hot pulsar crusts might undergo large amounts of plastic or ductile deformation and not crack nearly as often, an effect more recently argued by Link, Franco & Epstein (1998) as arising from high pressures (namely, $p \gg \mu$). Indeed, terrestrial materials undergo a brittle to ductile transition when pressures become much greater than their shear modulus (Turcotte & Schubert 1982). Thus there is a large range of options, none of which we are confident to exclude.

6.2 Integral expression for Q_{22} in terms of shear stresses

We write the stress-energy tensor of the solid as

$$\boldsymbol{\tau}_{ab} = -p\boldsymbol{g}_{ab} + \boldsymbol{t}_{ab}, \tag{58}$$

where $\boldsymbol{t}_{ab}$ is the (trace-free) shear stress tensor of the crust. Consider the 'deformed' star as a spherical star plus a small perturbation, and consider $\boldsymbol{t}_{ab}$ to be a first-order quantity, so that

$$\delta\tau_{ab} = -\delta p\boldsymbol{g}_{ab} + \boldsymbol{t}_{ab}. \tag{59}$$

Equilibrium between gravity and hydro-elastic forces implies

$$\nabla^a \delta\tau_{ab} = \delta\rho g(r)\hat{r}_b, \tag{60}$$

where we have neglected the influence of the perturbation on the star's gravitational field (the Cowling approximation). We expand the perturbation in spherical harmonics:

$$\boldsymbol{t}_{ab} = t_{rr}(r)Y_{lm}\left(\hat{r}_a\hat{r}_b - \tfrac{1}{2}\boldsymbol{e}_{ab}\right) + t_{r\perp}(r)\boldsymbol{f}_{ab} + t_\Lambda(r)\left(\boldsymbol{\Lambda}_{ab} + \tfrac{1}{2}Y_{lm}\boldsymbol{e}_{ab}\right), \tag{61}$$

where $\boldsymbol{e}_{ab}$, $\boldsymbol{f}_{ab}$ and $\boldsymbol{\Lambda}_{ab}$ were defined in equation (40). The above expansion is automatically trace-free. We have left out terms in $\boldsymbol{t}_{ab}$ proportional to $(\hat{r}_a\epsilon_{bcd} + \hat{r}_b\epsilon_{acd})r^d\nabla^c Y_{lm}$ or $(\nabla_a Y_{lm}\epsilon_{bcd} + \nabla_b Y_{lm}\epsilon_{acd})r^d\nabla^c Y_{lm}$ because, having opposite parity, they decouple from the other shear stress terms and cannot generate a quadrupole moment.

Projecting equation (60) along $\hat{r}^b$, we obtain

$$\delta\rho = \frac{1}{g(r)}\left(-\frac{\mathrm{d}\delta p}{\mathrm{d}r} + \frac{\mathrm{d}t_{rr}}{\mathrm{d}r} + \frac{3}{r}t_{rr} - \frac{\beta}{r}t_{r\perp}\right). \tag{62}$$

Downloaded from https://academic.oup.com/mnras/article-abstract/319/3/902/1075833 by California Institute of Technology user on 19 May 2020

We now replace the δp term on the right-hand side of equation (62) in favour of shear stress terms by projecting equation (60) along $\nabla^b Y_{lm}$, which yields (specializing to $l = 2$)

$$\delta p(r) = -\frac{1}{2}t_{rr} + \frac{3}{\beta}t_{r\perp} - \frac{1}{3}t_\Lambda + \frac{r}{\beta}\frac{\mathrm{d}t_{r\perp}}{\mathrm{d}r}. \tag{63}$$

Using $Q_{22} \equiv \int \delta\rho r^4\,\mathrm{d}r$, and integrating by parts (using the fact that the shear stress vanishes above and below the crust (see Section 4.2), we obtain

$$Q_{22} = -\int \frac{r^3}{g}\left[\frac{3}{2}(4-\tilde{U})t_{rr} + \frac{1}{3}(6-\tilde{U})t_\Lambda + \sqrt{\frac{3}{2}}\left(8 - 3\tilde{U} + \frac{1}{3}\tilde{U}^2 - \frac{1}{3}r\frac{\mathrm{d}\tilde{U}}{\mathrm{d}r}\right)t_{r\perp}\right]\mathrm{d}r, \tag{64}$$

where $\tilde{U}$ is defined in equation (44). This expression gives the quadrupole moment of the crust, so long as it is in hydro-elastic balance. Since this expression involves only shear stresses, it also makes clear that (static) perfect fluid stars cannot have a quadrupole moment.

6.3 Maximum Q_{22} set by crustal yield strain

We now reinterpret equation (64) in terms of strains, rather than stresses, by defining $\boldsymbol{\sigma}_{ab} = \boldsymbol{t}_{ab}/\mu$, where μ is the shear modulus. We define $\bar{\sigma}$ by $\bar{\sigma}^2 = \frac{1}{2}\boldsymbol{\sigma}_{ab}\sigma^{ab}$, and we assume that the crust will yield when $\bar{\sigma} > \bar{\sigma}_{\max}$. This criterion for yielding is called the von Mises criterion (Turcotte & Schubert 1982). Different empirical criteria are sometimes adopted (such as the Tresca criterion, which depends on the difference between the maximum and minimum eigenvalues of $\boldsymbol{\sigma}_{ab}$), but for our purpose they would all give similar answers, and the von Mises criterion is easier to use.

Note that $\tilde{U} = 4\pi r^3\rho/M_r \ll 1$ in the crust, so all the coefficients of the stress components in equation (64) are positive. Therefore we can compute the upper bound on Q_{22} by making the stress components t_{rr}, $t_{r\perp}$ and t_Λ as large as possible, subject to $\boldsymbol{\sigma}_{ab}\sigma^{ab} < 2\bar{\sigma}^2_{max}$. Of course, the crustal yield strain could vary with density, but given that its value is so uncertain, we shall simply take it to be some constant, characteristic of the entire crust.

Using our expansion (61) of $\boldsymbol{t}_{ab}$, we write[9]

$$\boldsymbol{\sigma}_{ab}\sigma^{ab} = \frac{3}{2}\sigma^2_{rr}[\mathrm{Re}(Y_{lm})]^2 + \sigma^2_{r\perp}[\mathrm{Re}(\boldsymbol{f}_{ab})]^2 + \sigma^2_\Lambda\left[\mathrm{Re}\left(\boldsymbol{\Lambda}_{ab} + \frac{1}{2}Y_{lm}\boldsymbol{e}_{ab}\right)\right]^2. \tag{65}$$

For $l = m = 2$, the following identity holds among our basis tensors:

$$\frac{3}{4}[\mathrm{Re}(Y_{lm})]^2 + \frac{3}{4}[\mathrm{Re}(\boldsymbol{f}_{ab})]^2 + \frac{9}{2}\left[\mathrm{Re}\left(\boldsymbol{\Lambda}_{ab} + \frac{1}{2}Y_{lm}\boldsymbol{e}_{ab}\right)\right]^2 = \frac{15}{32\pi}. \tag{66}$$

Therefore $\bar{\sigma}$ will attain its maximum value, $\bar{\sigma}_{\max}$, at *every* point in the crust – i.e., the crust will be everywhere stressed to the maximum – if we set

$$\sigma_{rr} = \left(\frac{32\pi}{15}\right)^{1/2}\bar{\sigma}_{\max}, \tag{67a}$$

$$\sigma_{r\perp} = \left(\frac{16\pi}{5}\right)^{1/2}\bar{\sigma}_{\max}, \tag{67b}$$

$$\sigma_\Lambda = \left(\frac{96\pi}{5}\right)^{1/2}\bar{\sigma}_{\max}. \tag{67c}$$

With this substitution, all the terms in the integrand in equation (64) share a common pre-factor, $\mu r^3/g$. Moreover, since $\tilde{U} \ll 1$, the integral in equation (64) can be expressed as $Q_{22} = \gamma\bar{\sigma}_{\max}I$, where the I is the integral

$$I \equiv \int \frac{\mu r^3\,\mathrm{d}r}{g}, \tag{68}$$

which depends strongly on M, R, and the location of the crust–core boundary, while γ is a numerical pre-factor that depends very weakly on those parameters. I is approximately given by $I \approx (2/7)\langle\mu/p\rangle(p_\mathrm{b}/g)R^3\Delta R$, where p_b is the pressure at the crust–core interface, ΔR is the crust thickness, and $\langle\mu/p\rangle$ is a (suitably) weighted average of the shear modulus in the crust. At densities well above neutron drip, the shear modulus is $\mu/p \sim 10^{-3}(Z/20)^2(88/A)^{4/3}\rho_{14}^{-1/3}$, assuming the neutron fraction $X_\mathrm{n} = 0.8$. The pressure is approximately ideal degenerate neutron pressure, $p_\mathrm{n} \propto \rho^{5/3}$, and ΔR is roughly 5/2 times scale height at p_b, i.e., $\Delta R \sim (5/2)p_\mathrm{b}/\rho_\mathrm{b}g$. Hence we expect the integral I to scale as $I \propto \rho_b^2R^7M^{-2}$. By fitting to our detailed numerical calculations, we get the more precise scaling $I = 3.61\times10^{37}\,\mathrm{g\,cm^2}\,\rho_{14}^{2.07}M_{1.4}^{-1.2}R_6^{6.26}$. Collecting terms, we find

$$Q_{\max} = 1.2\times10^{38}\,\mathrm{g\,cm^2}\left(\frac{\bar{\sigma}_{\max}}{10^{-2}}\right)\frac{R_6^{6.26}}{M_{1.4}^{1.2}}\left(\frac{Z}{20}\right)^2\left(\frac{88}{A}\right)^{4/3} \times\left(\frac{1-X_\mathrm{n}}{0.2}\right)^{4/3}\left(\frac{X_\mathrm{n}}{0.8}\right)^{5/3}\left(\frac{\rho_\mathrm{b}}{2.1\times10^{14}\,\mathrm{g\,cm^{-3}}}\right)^{2.07}, \tag{69}$$

where the values of Z, A and X_n are understood to be averaged over the crust, with a weighting pre-factor pr^3/g, which is heavily biased to select the values near the bottom of the crust. In equation (69) the pre-factor and the scalings for ρ_b, M and R are from numerical calculations, while the terms in Z, A and X_n simply come from our analytical scaling formula for the shear modulus.

Equation (69) is very powerful. It shows that, so long as only elastic forces are important, the maximum quadrupole moment attainable for an NS crust is $Q_{22} \approx 10^{38}\,\mathrm{g\,cm^2}(\bar{\sigma}_{\max}/10^{-2})$, no matter how the strains arise. The exact upper limit does depend on the NS radius, however. Note that for a given NS, EOS and crust composition, the upper bound on Q_{22} is smaller for heavier neutron stars (which have smaller radii). We also emphasize that even to approach this upper limit, almost all the strain must be in the Y_{22} spherical harmonic; strain in other harmonics pushes the crust closer to the yield point without contributing to Q_{22}.

Also note that, besides providing an upper limit, our formula (64) provides an estimate of the Q_{22} that can result for a given level of strain in the crust: $Q_{22} \approx 10^{38}\,\mathrm{g\,cm^2}(\langle\sigma_{22}\rangle/10^{-2})$, where $\langle\sigma_{22}\rangle$ is some (appropriately) weighted average of the '22-piece' of the crustal strain.

Note that our formula, suitably interpreted, also holds if the crust's stress–strain relation is in the non-linear regime. In that case, we just define an 'effective' strain $\sigma^{\mathrm{eff}}_{ab}$ by $\sigma^{\mathrm{eff}}_{ab} = \boldsymbol{t}_{ab}/\mu$, where μ is the shear modulus valid in the linear regime. Then equation (69) continues to hold if we replace $\bar{\sigma}_{\max}$ by $\bar{\sigma}^{\mathrm{eff}}_{max}$, the maximum value of the effective strain.

[9] Recall that we defined all our variables to be real.

Downloaded from https://academic.oup.com/mnras/article-abstract/319/3/902/1075833 by California Institute of Technology user on 19 May 2020

6.4 Crustal strain due to electron captures

What strains are induced by wavy e^- capture layers or a uniform composition gradient? Expanding the shear tensor as functions of r times (same-parity) basis tensors built from Y_{lm}, as in equation (38), and then expressing the radial functions in terms of our variables z_i, we have

$$\sigma_{rr}(r) = \frac{4}{3}\left(\frac{\partial\xi_r}{\partial r} - \frac{\xi_r}{r}\right) + \frac{2}{3}\frac{\beta\xi_\perp}{r} = \frac{4}{3}\frac{\mathrm{d}z_1}{\mathrm{d}\ln r} + \frac{2}{3}\beta^2 z_3, \tag{70a}$$

$$\sigma_{r\perp}(r) = r\frac{\partial}{\partial r}\frac{\xi_\perp}{r} + \frac{\beta\xi_\perp}{r} = \frac{\beta^2 z_4}{\mu}, \tag{70b}$$

$$\sigma_\Lambda(r) = 2\frac{\beta\xi_\perp}{r} = 2\beta^2 z_3. \tag{70c}$$

The rr-component of strain at any point in the crust is then $\sigma_{rr}(r,\theta,\phi) = \sigma_{rr}(r)\mathrm{Re}\{Y_{lm}(\theta,\phi)\}$, and similarly for the other components. In particular, for $l = m = 2$, the maximum value of the angular factor is $(15/32\pi)^{1/2} = 0.39$ for σ_{rr}, $(5/8\pi)^{1/2} = 0.45$ for $\sigma_{r\perp}$, and $(5/48\pi)^{1/2} = 0.18$ for σ_Λ. In other words, $\max\{\sigma_\Lambda^2[\mathrm{Re}(\boldsymbol{\Lambda}_{ab} + (1/2)Y_{lm}\boldsymbol{e}_{ab})]^2\} = 5/48\pi$, and similarly for σ_{rr} and $\sigma_{r\perp}$.

Figs 19 and 20 show the components of shear strain induced by the wavy capture layers and smooth composition gradients, respectively. In Fig. 19 the temperature perturbation comes from a thermal model with $\dot{M} = 0.5\dot{M}_{\rm Edd}$, and $f_{\rm nuc} = 0.1$; the resulting temperature perturbation at the $Q = 95$ MeV capture layer is $\delta T = 9\times10^6$ K ($\delta T/T \approx 2$ per cent; see Fig. 8), and the deformation of this layer leads to $Q_{22} = 8.8\times10^{37}$ g cm^2. The magnitude of the composition gradient in Fig. 20 is $\Delta\mu_{\rm e}/\mu_{\rm e} = 5\times10^{-3}$, which results in $Q_{22} = 1.2\times10^{38}$ g cm^2. Note that for these fiducial perturbations, the resulting Q_{22} values are basically what is needed for gravitational waves to balance accretion torque in LMXBs, with $\dot{M} \approx \dot{M}_{\rm Edd}$. Of course, both the strains and the quadrupole moment scale linearly with $f_{\rm nuc}$ or $\Delta\mu_{\rm e}/\mu_{\rm e}$.

From these figures it is evident that σ_{rr} is much bigger than $\sigma_{r\perp}$ and σ_Λ. Our mechanism is thus not optimally efficient at producing Q_{22}, since the crust ends up being much more strained at the equator than at the poles. (i.e., a solution that is near the yield strain at the equator is still relatively unstrained near the poles, and so the polar regions could be 'doing more' to hold up the quadrupole.) In fact, if σ_{rr} is the dominant stress component, then equation (69) becomes $Q_{22} = 3\times10^{37}$ g cm^2 $\langle\sigma_{rr}\rangle/10^{-2})$. The strain σ_{rr} near the bottom of the crust in these two models is $\sim$ (4–5)$\times10^{-2}$, which shows that this estimate accords nicely with our numerical solutions.

The second thing to note about Figs 19 and 20 is that $\sigma_{rr} > 10^{-1}$ near the top of the crust. Thus our linear elastic model is inconsistent there, in the sense that our solutions must certainly exceed the yield strain. To us, this suggests that our assumed level of composition inhomogeneity would drive a continual plastic deformation of the crust there. Although we are therefore using the 'wrong physics' to describe the top of the crust (i.e., we should be using equations that somehow incorporate plastic deformation), we believe this will not lead to significant errors in our main results–the values of Q_{22}. This is because, for the solutions shown in Figs 19 and 20, the top of the crust contributes only a small fraction to the total Q_{22}. For example, if we repeat these calculations, but with top of the crust set at around neutron drip ($r = 9.2\times10^5$ cm), we find that Q_{22} differs by $\sim$10 per cent from the value obtained with a full crust (see Fig. 16). As long as most of the crustal mass is strained below the yield level, our results for Q_{22} are reasonably accurate.

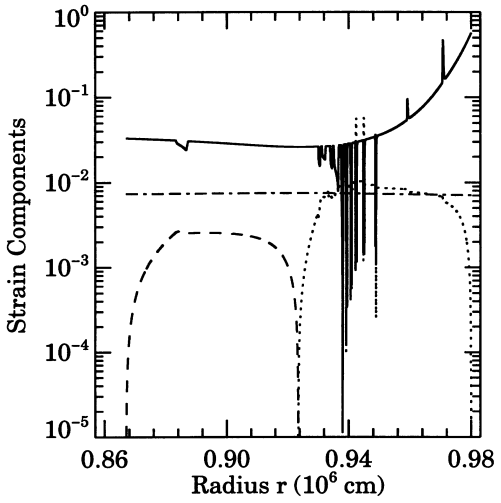

Figure 19. Angular maximum values of the shear strain components $\max_{(\theta,\phi)}\{\boldsymbol{\sigma}_{ab}\}$ as a function of the position in the crust due to the motion of a deep capture layer ($Q = 95$ MeV) in response to an $f_{\rm nuc} = 0.1$ thermal perturbation. The background model has a normal core, the accretion rate is $0.5\dot{M}_{\rm Edd}$, and the quadrupole moment is $Q_{22} = 8.8\times10^{37}$ g cm^2. The solid line denotes $(15/32\pi)^{1/2}\sigma_{rr}(r)$, the dashed line indicates $(5/8\pi)^{1/2}\sigma_{r\perp}(r)$, and the dot-dashed line shows $(5/48\pi)^{1/2}\sigma_\Lambda(r)$, where $\boldsymbol{\sigma}_{ab}(r)$ are as defined in equation (70).

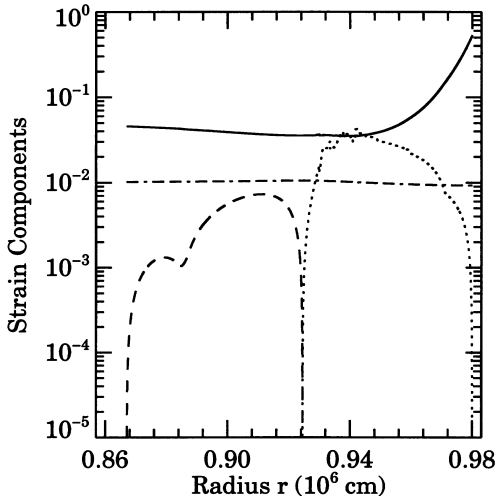

Figure 20. Same as Fig. 19, but for displacements sourced by a smooth composition gradient with $\Delta\mu_{\rm e}/\mu_{\rm e} = 5\times10^{-3}$. The quadrupole moment in this case is $Q_{22} = 1.2\times10^{38}$ g cm^2.

The fact that a smooth composition gradient induces a $Q_{22} = 1.2\times10^{38}$ g cm^2 $((\Delta\mu_{\rm e}/\mu_{\rm e})/0.5$ per cent) has interesting astrophysical implications. As is evident from Fig. 20, even such small composition gradients induce sizeable strains in the crust. Moreover, unlike the quadrupole moments produced by deformed capture layers, which would be wiped out in the time it takes to accrete the mass in a capture layer (Bildsten 1998a), if the thermal gradient is turned off, the uniform composition gradient can only be eliminated by replacing the entire crust, i.e., accreting $\sim0.05\,M_\odot$ of material. Hence, even when accretion ceases, the crust of an LMXB neutron star is likely to have a remnant

Downloaded from https://academic.oup.com/mnras/article-abstract/319/3/902/1075833 by California Institute of Technology user on 19 May 2020

quadrupole moment. In transiently accreting systems, this remnant quadrupole moment may set an upper limit on the spin frequency.

In general, it is clear that at high accretion rates ($\gtrsim 0.5\dot{M}_{\rm Edd}$), the quadrupole moment needed to balance accretion requires the crustal strain to be $\gtrsim 10^{-2}$. This is probably higher than the yield strain, so if such equilibrium prevails, it seems the entire crust must be in a state of continual plastic flow. Assuming that accretion continually deforms the entire crust by the above mechanism, the stresses are likely to stay near the yield value. This can provide a natural explanation for the similarity of spin frequencies in near-Eddington accretion rate systems. We have not attempted to model the resulting plastic flow, but that may be worth pursuing. We caution, however, that this picture of inhomogeneity-driven plastic flow is based solely on the folklore regarding yield strains of materials, as no definitive calculations of $\bar{\sigma}_{\rm max}$ exist, and estimates are typically based upon extrapolating experimental results for ordinary terrestrial materials by >10 orders of magnitude. Our approximations *have* allowed us to quantify quite clearly how large the crustal stresses must be for gravitational wave emission to be appreciable in accreting neutron stars. How the crust responds to such high stresses is a problem for future research.

Since the quadrupole moment scales linearly with the crustal strain, in lower accretion rate systems ($\lesssim 0.5\dot{M}_{\rm Edd}$), the required strains are correspondingly lower ($\sim 10^{-3}$–10^{-2}). Moreover, we showed in Section 5 (see Fig. 17), that for a fixed composition asymmetry ($f_{\rm nuc}$ or $f_{\rm comp}$) Q_{22} has exactly the right scaling with $\dot{M}$ to balance the accretion torque by mass quadrupole gravitational radiation at a fixed spin frequency, independent of the accretion rate. On the other hand, for high accretion rate systems ($\gtrsim 0.5\dot{M}_{\rm Edd}$), in order to explain the spin frequency clustering at *exactly* 300 Hz, our mechanism requires that the asymmetry in the crust ($f_{\rm nuc}$ or $f_{\rm comp}$) correlate with $\dot{M}$ in a well-defined way (see Fig. 17). Alternatively, if $f_{\rm comp}$ and $f_{\rm nuc}$ are the same as in lower accretion rate systems, then we would expect brighter LMXBs to have higher spin frequencies. Given the uncertainty in the spin frequency measurements for these sources, such a possibility cannot be ruled out at present.

6.5 Correction for self-gravity of the perturbations

In deriving the maximum quadrupole formula, equations (64) and (69), as well as in the rest of this paper, we have neglected the changes in the gravitational force due to the perturbation itself – i.e., we have neglected the deformation's self-gravity (the Cowling approximation). Very roughly, one would expect these self-gravity corrections to increase Q_{22} by a fractional amount proportional to $I_{\rm crust}/I_{\rm NS} \sim 0.1$. However, including the gravitational potential perturbation, $\delta\Phi$, allows non-zero $\delta\rho$ in the interior of the stellar core, something that was forbidden within the Cowling approximation. For perturbations with low l, the self-gravity effect turns out to be much larger than $\mathcal{O}(I_{\rm crust}/I_{\rm NS})$. We now derive a formula for Q_{22} similar to equation (64), but including the self-gravity of the deformation. However, while equation (64) was exact (within the Cowling approximation), our improved version will include the effects of self-gravity only in an approximate way.

Including Newtonian self-gravity, our expressions (58), (59) and (61) for $\boldsymbol{\tau}_{ab}$, $\delta\tau_{ab}$ and $\boldsymbol{t}_{ab}$ remain valid, but now the equilibrium $\delta\tau_{ab}$ satisfies

$$\nabla^a \delta\tau_{ab} = \delta\rho g(r)\hat{r}_b + \rho\nabla_b\delta\Phi. \tag{71}$$

Projecting equation (71) along $\hat{r}^b$, we obtain

$$\delta\rho = \frac{1}{g(r)}\left[-\frac{{\rm d}\delta p}{{\rm d}r} + \frac{{\rm d}t_{rr}}{{\rm d}r} + \frac{3}{r}t_{rr} - \frac{\beta}{r}t_{r\perp}\right] - \frac{\rho}{g}\frac{{\rm d}\delta\Phi}{{\rm d}r}. \tag{72}$$

Replacing δp in (71) by projecting equation (71) along $\nabla^b Y_{lm}$, and integrating by parts to eliminate radial derivatives of the shear terms, we obtain

$$Q_{22} = \text{rhs of (64)} + \int_0^R \frac{r^4}{g}\frac{{\rm d}\rho}{{\rm d}r}\delta\Phi\,{\rm d}r, \tag{73}$$

where the 'extra' term ' in equation (73) is an integral over the entire star, not just the crust. Deformations in the crust change the potential throughout the star, so now $\delta\rho$ is non-zero everywhere.

Equation (73) is exactly true, but not very useful without knowing $\delta\Phi(r)$. We introduce an approximation that allows us to obtain a closed-form expression for Q_{22}. We expect that for large quadrupole moments, most of the density perturbation lies near the bottom of the crust. As an approximation, then, we use the $\delta\Phi(r)$ appropriate to a thin deformed shell at radius $r_{\rm bot}$, the location of the crust–core boundary:

$$\delta\Phi(r) = -\frac{4\pi}{5}Q_{22}\begin{cases} r^2/r_{\rm bot}^5 & r < r_{\rm bot} \\ 1/r^3 & r > r_{\rm bot}. \end{cases} \tag{74}$$

Plugging equation (74) into equation (73), we obtain

$$Q_{22} \approx -(1-\mathcal{F})^{-1}\int\frac{r^3}{g}\left[\frac{3}{2}(4-\tilde{U})t_{rr} + \frac{1}{3}(6-\tilde{U})t_\Lambda + \sqrt{\frac{3}{2}}\left(8 - 3\tilde{U} + \frac{1}{3}\tilde{U}^2 - \frac{1}{3}r\frac{{\rm d}\tilde{U}}{{\rm d}r}\right)t_{r\perp}\right]{\rm d}r, \tag{75}$$

where

$$\mathcal{F} \equiv -\frac{4\pi}{5}\left[r_{\rm bot}^{-5}\int_0^{r_{\rm bot}}\frac{r^8}{m(r)}\frac{{\rm d}\rho}{{\rm d}r}{\rm d}r + \int_{r_{\rm bot}}^R \frac{r^3}{m(r)}\frac{{\rm d}\rho}{{\rm d}r}{\rm d}r\right]. \tag{76}$$

Note that $\mathcal{F}$ is manifestly positive (since ${\rm d}\rho/{\rm d}r < 0$), so the factor $(1-\mathcal{F})^{-1}$ coming from self-gravity always leads to an enhancement in Q_{22} over the value given by our formula (64). Typical values of $\mathcal{F}$ are 0.2–0.5, depending on the exact core model. Hence we expect that including self-gravity in the full calculation will enhance the resulting Q_{22} by 25–200 per cent.

7 CONCLUSIONS

We have investigated whether the accretion-driven spin-up of neutron stars in low-mass X-ray binaries (LMXBs) can be halted by gravitational wave emission due to mass quadrupole moments generated in their crusts. The quadrupole moment needed to reach this spin equilibrium is $Q_{22} \approx 10^{37}$–$10^{38}\,{\rm g\,cm^2}$ (see equation 4) for the relevant accretion rates in LMXBs, 10^{-10}–$2\times 10^{-8}\,{\rm M_\odot\,yr^{-1}}$. How to form and sustain such a large quadrupole is the main problem we addressed. We have undertaken a series of calculations that substantially extend the original idea of Bildsten (1998a) that electron capture reactions can deform the crust by large amounts. The major results of our work are as follows.

(i) By self-consistently solving the elastic equilibrium equations (Sections 4 and 5) we have found that the predominant response of the crust to a lateral density perturbation is to sink, rather than move sideways. For this reason, the quadrupole moments due to temperature-sensitive e^- captures in the *outer* crust (i.e., the case

Downloaded from https://academic.oup.com/mnras/article-abstract/319/3/902/1075833 by California Institute of Technology user on 19 May 2020

considered by Bildsten 1998a) are actually much too small to buffer the accretion torque. However, a single e^- capture layer in the deep *inner* crust can easily generate an adequate mass quadrupole. This requires lateral temperature variations in the deep crust of order $\lesssim 5$ per cent, and the realistic case of multiple electron capture layers requires a proportionately smaller temperature variation. Because of the much larger mass involved in generating Q_{22} in the inner crust, the temperature contrasts required are only $\sim 10^6$–10^7 K, rather than $\sim 10^8$ K originally envisaged by Bildsten (1998a). Alternatively, a 0.5 per cent lateral variation in the charge-to-mass ratio can generate a Q_{22} sufficient to balance the accretion torque even in the absence of a temperature gradient.

(ii) Our thermal perturbation calculations show that the temperature variations required to induce such a large quadrupole moment can easily be maintained if the compressionally induced nuclear reactions around neutron drip inject heat with about ~ 10 per cent lateral variations. Lateral variations of the same magnitude in the average Z^2/A of nuclei in the crust can also maintain a similar temperature asymmetry. This is despite the strong thermal contact with the isothermal core of the neutron star (see Section 3). However, if accretion halts or slows considerably, then these temperature variations will be wiped out in a thermal time, i.e., a few years at the crust–core interface (equation 31). In this case the e^- capture boundary deformations will be smoothed out in the time it takes to accrete the mass in a capture layer, $\sim 2.5 \times 10^6$ yr $(\dot{M}/10^{-9}\,\mathrm{M}_\odot\,\mathrm{yr}^{-1})$ near the crust–core boundary.

(iii) While it is not possible to estimate the size of the compositional or nuclear heating asymmetries a priori, the temperature variations in the deep crust lead to lateral variations in the persistent thermal flux emerging from the neutron star. Since the neutron star is spinning, a certain Q_{22} implies an amplitude of the modulation of the persistent X-ray flux (see Figs 9 and 18). Though a small effect, these periodic variations can be searched for observationally. Detection of such modulation would help tremendously in the search for gravitational wave emission.

(iv) If the size of the heating or composition asymmetry is a constant fixed fraction, then we showed that for $\dot{M} \lesssim 0.2\dot{M}_{\rm Edd}$ the scaling of Q_{22} with $\dot{M}$ is just that needed for all of these low accretion rate neutron stars to have the same spin frequency (see Fig. 17).

(v) Quadrupoles as large as this require a strain in the crust of order 10^{-3}–10^{-2} (depending on the accretion rate, with strains exceeding 10^{-2} for $\dot{M} \gtrsim 0.5\dot{M}_{\rm Edd}$; see discussion in Section 6.4), *regardless* of the detailed mechanism for generating the strain.

(vi) We have derived a general relation between the maximum quadrupole moment $Q_{\rm max}$ that a crust can support via elastic deformation and its breaking strain (see Section 6). Our relation (equations 64 and 69) is more complete than previous work and is widely applicable. In addition to determining $Q_{\rm max}$, this relation allows one to robustly estimate the quadrupole moment for a given level of strain, even in the non-linear regime, regardless of the amount of plastic flow or relaxation that the crust has undergone.

Our work has thus clarified many of the important outstanding questions for the hypothesis that gravitational wave emission due to a crustal quadrupole moment can buffer the accretion torque. We now discuss the implications of our results for the millisecond radio pulsars and for the possibility of gravitational waves from wobbling neutron stars.

Ever since the discovery of the first millisecond radio pulsar (Backer et al. 1982), observers have been looking for rapidly rotating neutron stars near the breakup limit of $\nu_{\rm b} \approx 1476\,\mathrm{Hz}\, M_{1.4}^{1/2} R_6^{-3/2}$ (see Cook, Shapiro & Teukolsky 1994 for an exhaustive survey of the breakup limits for different nuclear equations of state). However, few have been found. Even today, it is still the case that the majority of millisecond radio pulsars are spinning at 300 Hz or less. By considering the characteristic ages of those pulsars that reside in binaries, Backer (1998) concluded that most of the initial spin frequencies of the radio pulsars are near 300 Hz, consistent with the later inferences from the accreting population. In this paper we have shown that accretion-induced lateral density variations in NS crusts can indeed account for limiting the initial spins of millisecond pulsars.

However, there are a few millisecond pulsars that do spin much faster than 300 Hz (e.g., B 1937+21 and B 1957+20, which have periods of roughly 1.6 ms). For these fast pulsars, a possible explanation is that their crusts are very uniform, so that the composition asymmetry is $\ll 10$ per cent as required to generate the appropriate Q_{22}. A much more likely hypothesis is that these pulsars were spun up in transiently accreting systems with recurrence times greater than a few years, or accreting at a very slow rate. Lateral temperature variations in this regime would not persist, and hence the quadrupole moment resisting accretion would be much smaller.

We finally turn to the possibility of gravitational waves from wobbling neutron stars. Our calculation of the maximum Q_{22} sustainable by the crust can also be used to place a strong limit on the strength of such wobble radiation. An NS will 'wobble' if its angular momentum J^a is slightly misaligned from some principal axis of the crust. This phenomenon occurs in the Earth, and is called the Chandler wobble. It is a somewhat more complicated version of the torque-free precession of rigid bodies that is treated in undergraduate mechanics texts. For the sake of brevity, we will simply quote many of the relevant results from this area, and refer the reader to Munk & MacDonald (1960), Pines & Shaham (1972), Cutler & Jones in preparation, and Jones (2000) for more details.

Consider first a rotating (and hence oblate) NS, which is spinning along some principal axis of the crust. If the relaxed state of the star is spherical, then, no matter how the NS is kicked, it will not precess. However, if the crust has relaxed to the oblate state (i.e., the zero-stress state is oblate), then kicking the NS will cause precession.

Let the star's angular momentum J^a be along z^a, which is displaced (by some kick) from the principal axis of the crust n^a by angle $\theta_{\rm w}$. To a sufficient approximation, the inertia tensor of the wobbling body will be

$$I^{ab} = I_0 e^{ab} + \Delta I_\Omega \left(\hat{z}^a\hat{z}^b - \tfrac{1}{3}g^{ab}\right) + \Delta I_{\rm d}\left(\hat{n}^a\hat{n}^b - \tfrac{1}{3}g^{ab}\right). \tag{77}$$

and this 'figure' will rotate rigidly around z^a with precession frequency $\omega_{\rm p} \approx \Omega$. Thus $\Delta I_{\rm d}$ is the piece of the inertia tensor that 'follows' the principal axis of the crust. Defining $\hat{x}^a$ by $\hat{n}^a \approx \hat{z}^a + \theta_{\rm w}\hat{x}^a$, we see that $\boldsymbol{I}_{ab}$ for the wobbling star can be rewritten as

$$I^{ab} = I_0 e^{ab} + (\Delta I_\Omega + \Delta I_{\rm d})\left(\hat{z}^a\hat{z}^b - \tfrac{1}{3}g^{ab}\right) + \theta_{\rm w}\Delta I_{\rm d}(\hat{z}^a\hat{x}^b + \hat{x}^a\hat{z}^b). \tag{78}$$

Here the piece oriented along $\hat{z}^a$ is 'held up' by centrifugal force, while the piece proportional to $\theta_{\rm w}\Delta I_{\rm d}$ is 'held up' by crustal shear stresses and is responsible for the star's Q_{21} moment. A little algebra shows that

$$Q_{21} = \sqrt{\frac{15}{2\pi}}\theta_{\rm w}\Delta I_{\rm d}. \tag{79}$$

Downloaded from https://academic.oup.com/mnras/article-abstract/319/3/902/1075833 by California Institute of Technology user on 19 May 2020

The dominant gravitational wave emission is at the wobble frequency, so $\omega_{\rm gw} \approx \Omega$, and the gravitational wave luminosity is

$$L_{\rm gw}^{\rm wobble} = \frac{2}{5}(\theta_{\rm w}\Delta I_{\rm d})^2\Omega^6 = \frac{4\pi}{75}Q_{21}^2\Omega^6. \quad (80)$$

Comparing with equation (3), we see that for a fixed spin frequency Ω, $L_{\rm gw}^{l=m=2}/L_{\rm gw}^{\rm wobble} = 64(Q_{22}/Q_{21})^2$. The same ratio holds for the backreaction torques. Thus, if the accretion torque is balanced by the wobble radiation, rather than $l = m = 2$ radiation, resulting in $\nu_{\rm s} \approx 300\,{\rm Hz}$, then the required quadrupole moment is 8 times larger for the wobble case. This would require an average strain $\bar{\sigma} \approx 2.3 \times 10^{-2}$ for $\dot{M} = 10^{-9}\,{\rm M}_\odot\,{\rm yr}^{-1}$ and our fiducial NS mass and radius. Alternatively, if one fixes the gravitational wave frequency (instead of the spin frequency), and asks what is the maximum gravitational wave luminosity achievable by either $l = m = 2$ radiation or wobble radiation, we see that the limit set by crust cracking is exactly the same for the two cases [up to small corrections of order $(\Omega/\Omega_{max})^2$ and Q/MR^2] – a rather pretty result!

ACKNOWLEDGMENTS

We thank Andrew Cumming, Chris McKee and Kip Thorne for many initial discussions. Ed Brown provided much assistance with the construction and cross-checking of our thermal models. Patrick Brady shared his notes on normalizations and detectability of pulsar GW signals. D. I. Jones pointed out an error in our treatment of NS wobble, and suggested the outlines of the correct answer. GU acknowledges the Fannie and John Hertz foundation for fellowship support. This research was supported by NASA via grants NAG5-4093, NAG5-8658 and NAGW-4517, and by the National Science Foundation under Grant No. PHY94-07 194. LB is a Cottrell Scholar of the Research Corporation.

REFERENCES

Andersson N., Kokkotas K. D., Stergioulas N., 1999, ApJ, 516, 307
Backer D. C., 1998, ApJ, 493, 873
Backer D. C., Kulkarni S. R., Heiles C., Davis M. M., Goss W. M., 1982, Nat, 300, 615
Baym G., Bethe H. A., Pethick C. J., 1971, Nucl. Phys. A, 175, 225
Bhattacharya D., van den Heuvel E. P. J., 1991, Phys. Rep., 203, 1
Bildsten L., 1998a, ApJ, 501, L89
Bildsten L., 1998b, in Buccheri R., van Paradijs J., Alpas M. A., eds, The Many Faces of Neutron Stars. Kluwer Academic Publishers, Dordrecht, Boston, p. 419
Bildsten L., Cumming A., 1998, ApJ, 506, 842
Bildsten L., Cutler C., 1995, ApJ, 449, 800
Bildsten L., Ushomirsky G., 2000, ApJ, 529, L33
Blaes O., Blandford R., Madau P., Koonin S., 1990, ApJ, 363, 612
Bradshaw C. F., Fomalont E. B., Geldzahler B. J., 1999, ApJ, 512, L121
Brady P. R., Creighton T., 2000, Phys. Rev. D, 61, 14051
Brady P. R., Creighton T., Cutler C., Schutz B. F., 1998, Phys. Rev. D, 57, 1
Brown E. F., 2000, ApJ, 531, 988
Brown E. F., Bildsten L., 1998, ApJ, 496, 915
Brown E. F., Ushomirsky G., 2000, ApJ, 536, 915
Brown E. F., Bildsten L., Rutledge R. E., 1998, ApJ, 504, L95
Cheng B., Epstein R. I., Guyer R. A., Young C., 1996, Nat, 382, 518
Cook G. B., Shapiro S. L., Teukolsky S. A., 1994, ApJ, 424, 823
Haensel P., 1997, in March J. A., Lasota J. P., eds, Relativistic Gravitation and Gravitational Radiation; Proceedings of the Les Houches School of Physics 26 Sept. – 6 Oct. Cambridge Univ. Press, Cambridge, p. 129
Haensel P., Zdunik J. L., 1990a, A&A, 229, 117
Haensel P., Zdunik J. L., 1990b, A&A, 227, 431
Haensel P., Kaminker A. D., Yakovlev D. G., 1996, A&A, 314, 328
Jones D. I., 2000, PhD thesis, Univ. Cardiff
Kaminker A. D., Haensel P., 1999, Acta Physica Polonica B, 30, 1125
Kittel C., 1956, Solid State Physics. Wiley, New York
Levin Y., 1999, ApJ, 517, 328
Levin Y., Ushomirsky G., 2000, MNRAS, in press (astro-ph/0006028)
Link B., Franco L. M., Epstein R. I., 1998, ApJ, 508, 838
McDermott P. N., Van Horn H. M., Hansen C. J., 1988, ApJ, 325, 725
Miller M. C., Lamb F. K., Psaltis D., 1998, ApJ, 508, 791
Munk W. H., MacDonald G. J., 1960, The Rotation of the Earth. Cambridge Univ. Press, Cambridge
Negele J. W., Vautherin D., 1973, Nucl. Phys. A, 207, 298
Papaloizou J., Pringle J. E., 1978, MNRAS, 184, 501
Pethick C. J., Ravenhall D. G., 1995, Annu. Rev. Nucl. Part. Sci., 45, 429
Pethick C. J., Ravenhall D. G., Lorenz C. P., 1995, Nucl. Phys. A, 584, 675
Pines D., Shaham J., 1972, Phys. Earth Planet. Interiors, 6, 103
Press W. H., Teukolsky S. A., Vetterling W. T., Flannery B. P., 1992, Numerical Recipes in C. Cambridge Univ. Press, Cambridge
Rembges F., Freiburghaus C., Rauscher T., Thielemann F. K., Schatz H., Wiescher M., 1997, ApJ, 484, 412
Rembges J. F., Liebendörfer M., Rauscher T., Thielemann F. K., Schatz H., 1998, in Hillebrandt W., Muller E., eds, Proceedings of the 9th on Nuclear Astrophysics. Max-Planck-Institut für Astrophysik, Garching bei München, p. 71
Ruderman M., 1991, ApJ, 382, 587
Sato K., 1979, Prog. Theor. Physics, 62, 957
Schatz H., Bildsten L., Cumming A., Wiescher M., 1999, ApJ, 524, 1014
Shapiro S., Teukolsky S. A., 1983, Black Holes, White Dwarfs, and Neutron Stars. John Wiley & Sons, Inc., New York
Smoluchowski R., 1970, Phys. Rev. Lett., 24, 923
Smoluchowski R., Welch D., 1970, Phys. Rev. Lett., 24, 1191
Strohmayer T., Van Horn H. M., Ogata S., Iyetomi H., Ichimaru S., 1991, ApJ, 375, 679
Strohmayer T. E., Zhang W., Swank J. H., Smale A., Titarchuk L., Day C., Lee U., 1996, ApJ, 469, L9
Takeuchi H., Sato M., 1972, Methods in Computational Physics, 11, 217
Thielemann F. K., Schatz H., Rauscher T., Rembges J. F., Görres J., Wiescher M., Bildsten L., 1998, in Mezzacappa A., eds, Stellar Evolution, Stellar Explosions and Galactic Chemical Evolution, Proceedings of the 2nd Oak Ridge Symposium on Atomic and Nuclear Astrophysics, Oak Ridge, Tennessee, 2–6 December 1997. Institute of Physics Publishing
Thompson C., Duncan R. C., 1995, MNRAS, 275, 255
Turcotte D. L., Schubert G., 1982, Geodynamics: Applications of Continuum Physics to Geological Processes. Wiley, New York
van der Klis M., 1998, in Buccheri R., van Paradijs J., Alpar M. A., eds, The Many Faces of Neutron Stars. Kluwer Academic Publishers, Dordrecht, Boston, p. 337
van der Klis M., 2000, ARA&A, 38, 9005
Vaughan B. A. et al., 1994, ApJ, 435, 362
Wagoner R. V., 1984, ApJ, 278, 345
White N. E., Zhang W., 1997, ApJ, 490, L87
Yakovlev D. G., Urpin V. A., 1980, SvA, 24, 303

APPENDIX A: COEFFICIENTS AND SOURCE TERMS OF THE ELASTIC PERTURBATION EQUATIONS

In this appendix we describe how to compute the coefficients and source terms of equations (43) from the background models developed in Sections 2 and 3.

We use the shear modulus as computed by Strohmayer et al. (1991) by Monte Carlo simulations of both bcc crystals and quenched solids. Their results can be conveniently rewritten in

Downloaded from https://academic.oup.com/mnras/article-abstract/319/3/902/1075833 by California Institute of Technology user on 19 May 2020

terms of the pressure of degenerate relativistic electrons,

$$\frac{\mu}{p_e} = \frac{6\times10^{-3}}{1+0.595(173/\Gamma_{\rm Coul})^2}\left(\frac{Z}{8}\right)^{2/3}, \tag{A1}$$

where $\Gamma_{\rm Coul}$ is defined in equation (19). We neglect the slight dependence of the shear modulus on temperature. Because of the uncertainty of the charge of nuclei at the bottom of the crust, we varied the numerator of equation (A1), as described in Section 5.1. At densities higher than neutron drip, we have $\alpha_1 = (\mu/p_e)(p_e/p)$. The run of μ with pressure in the crust is shown in the top panel of Fig. A1.

In addition to the shear modulus, we require a few thermodynamic derivatives. Let us first consider the case of the perturbations generated by a smooth composition variation in the crust, i.e., $\mu_e(r,\theta,\phi) = \mu_e(r) + \Delta\mu_e(r)Y_{lm}(\theta,\phi)$. In our computations we took $\Delta\mu_e(r)/\mu_e(r) = $ constant, but the formalism applies for arbitrary variation of $\Delta\mu_e$ with depth.

In this case, we write $p = p(\rho,\mu_e)$ and Δp using equation (34). The index Γ in this case is computed at constant composition,

$$\Gamma = \Gamma_\rho \equiv \left.\frac{\partial\ln p}{\partial\ln\rho}\right|_{\mu_e} = \frac{4}{3}\frac{p_e}{p} + \left.\frac{\partial\ln p_n}{\partial\ln\rho}\right|_{X_n}\frac{p_n}{p}, \tag{A2}$$

where $p_e \propto (\rho/\mu_e)^{4/3}$ is the relativistic electron degeneracy pressure, and $p_n(\rho,X_n) = p_n(X_n\rho/m_b)$ is the neutron pressure. If the neutrons were completely degenerate, non-relativistic and non-interacting, the pre-factor of p_n/p would be 5/3. The actual run of Γ_ρ with pressure is shown by the solid line in Fig. A1.

Following equation (45), we write the source term as $\Delta S = \Gamma_{\mu_e}(\Delta\mu_e/\mu_e)$, where

$$\Gamma_{\mu_e} \equiv \left.\frac{\partial\ln p}{\partial\ln\mu_e}\right|_{\rho} = -\frac{4}{3}\frac{p_e}{p} + \left.\frac{\partial\ln p_n}{\partial\ln\mu_e}\right|_{\rho}\frac{p_n}{p}. \tag{A3}$$

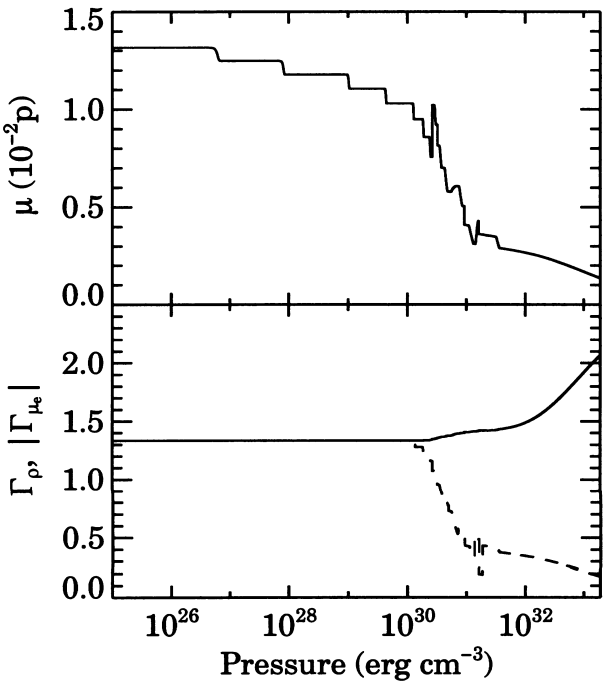

Figure A1. Top panel: The run of the shear modulus μ/p with depth. Bottom panel: The run of Γ_ρ (solid line) and $|\Gamma_{\mu_e}|$ (dashed line) with pressure in our model. Note that Γ_{μ_e} is negative, so its absolute value is plotted. For pressures $p \lesssim 10^{30}\,{\rm erg\,cm^{-3}}$ (i.e., for densities less than neutron drip) $\Gamma_\rho = |\Gamma_{\mu_e}|$.

Using the chain rule, we express the pre-factor of the p_n/p term in terms of the pre-factor of the similar term in Γ_ρ as

$$\left.\frac{\partial\ln p_n}{\partial\ln\mu_e}\right|_{\rho} = \frac{{\rm d}\ln X_n}{{\rm d}\ln\mu_e}\left.\frac{\partial\ln p_n}{\partial\ln\rho}\right|_{X_n}, \tag{A4}$$

where

$$\frac{{\rm d}\ln X_n}{{\rm d}\ln\mu_e} = -\frac{1}{X_n\mu_e}\frac{X_{n1}-X_{n2}}{1-X_{n1}}\left[\frac{Z_1}{A_1} - \frac{Z_2}{A_2}\left(\frac{1-X_{n2}}{1-X_{n1}}\right)\right]^{-1} \approx \frac{1-X_n}{X_n}, \tag{A5}$$

which follows from equations (14) and (15). Using the above formalism, one can compute the source term ΔS and the index Γ of equation (45). The source term ΔS for this case is shown in the bottom panel of Fig. 13.

Most of the discussion in this paper was concerned with the quadrupole moments generated by shifts in capture layers. For most of the calculation we have adopted the physical picture described by equation (46), i.e., that a temperature variation δT 'undoes' some electron captures on the 'cold' side of the star and induces more captures on the 'hot' side, and hence moves the capture layer vertically. This picture is physically consistent, and the formalism for deriving the source terms is described below. However, it is somewhat easier to first understand the Lagrangian $\Delta z_{\rm d}$ picture introduced in Section 1.2.

In this picture, we first imagine that the crust is infinitely rigid, and hence does not allow either vertical or horizontal elastic adjustment. We then go in and 'by hand' undo some captures on one side of the star, to a height $\Delta z_{\rm d}$ above the original capture layer, and induce some captures to the same depth on the other side of the star. The perturbed crust then looks like the sketch in Fig. 2. After this perturbation, we allow the crust to respond elastically. This perturbation is Lagrangian in the sense that we know a priori which fluid elements have had their μ_e perturbed.

We now formulate the above picture mathematically. The pressure at which the capture reaction occurs varies laterally. In a spherically symmetric star, the capture layer occurs at $r = r_c$ [i.e., (A_1, Z_1) element is, say, 50 per cent depleted at $r = r_c$]. When we put in the μ_e perturbation, the depletion occurs at $r = r_c + \Delta z_{\rm d}Y_{lm}$. It is an excellent approximation to assume that the shape of the capture layer does not change, only its position in the star. In this case, we write $\mu_e(r,\theta,\phi) \approx \tilde{\mu}_e[r - r_c - \Delta z_{\rm d}Y_{lm}(\theta,\phi)]$ and Taylor-expand to find $\Delta\mu_e/\mu_e \approx -({\rm d}\ln\mu_e/{\rm d}r)\Delta z_{\rm d}Y_{lm}$. The source terms are then

$$\Delta S \approx -\Gamma_{\mu_e}\frac{{\rm d}\ln\mu_e}{{\rm d}r}\Delta z_{\rm d}, \tag{A6}$$

where $\mu_e(r)$ is the run of electron mean molecular weight in the equilibrium model. Since $\mu_e(r)$ is constant outside the capture layers, this source term is non-zero only in the capture layers. A plot of ${\rm d}\ln\mu_e/{\rm d}\ln r$ is shown in Fig. A2. Since $\mu_e(r)$ resembles a step function with steps at the locations of the capture layers, ${\rm d}\ln\mu_e/{\rm d}\ln r$ resembles a delta function at the locations of the capture layers.

Now consider the case where the capture layers are moved around by lateral temperature variations, i.e., the case of δT-sourced perturbations. In our EOS, the dependence on temperature only comes in through μ_e, i.e., $\rho = \rho[p,\mu_e(p,T)]$. Therefore

$$\left.\frac{\partial\ln\rho}{\partial\ln p}\right|_T = \frac{1}{\Gamma_\rho} + \left.\frac{\partial\ln\rho}{\partial\ln\mu_e}\right|_{\rm p}\left.\frac{\partial\ln\mu_e}{\partial\ln p}\right|_T. \tag{A7}$$

Downloaded from https://academic.oup.com/mnras/article-abstract/319/3/902/1075833 by California Institute of Technology user on 19 May 2020

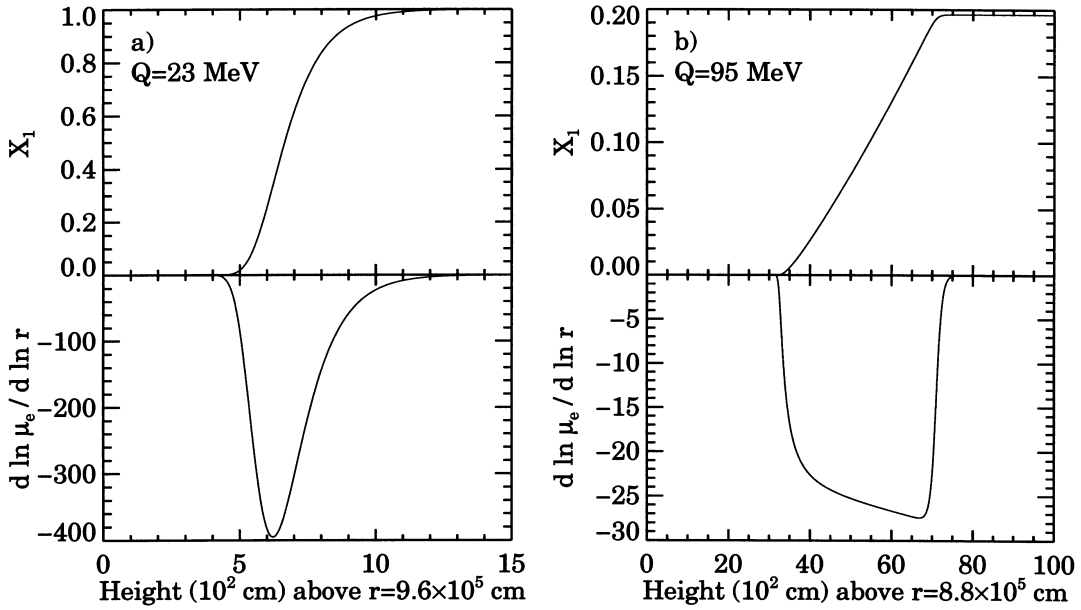

Figure A2. Left (a): The run of the mass fraction X_1 (top panel) and $\mathrm{d}\ln\mu_\mathrm{e}/\mathrm{d}\ln r$ with radius for a shallow capture layer at threshold energy $Q = 23\,\mathrm{MeV}$. Right (b): Same as (a), but for a deep capture layer at $Q = 95\,\mathrm{MeV}$.

The derivative at constant p in the second term above is displayed more conveniently by changing back to (ρ, μ_e) as independent variables,

$$\left.\frac{\partial \ln \rho}{\partial \ln \mu_\mathrm{e}}\right|_\mathrm{p} = -\frac{\Gamma_{\mu_\mathrm{e}}}{\Gamma_\rho}, \tag{A8}$$

so in the case of δT perturbations,

$$\Gamma = \Gamma_\rho \left[1 - \Gamma_{\mu_\mathrm{e}} \left.\frac{\partial \ln \mu_\mathrm{e}}{\partial \ln p}\right|_T\right]^{-1}. \tag{A9}$$

The term in square brackets is equal to 1 outside the capture layers, and hence Γ reduces to the same value as in the case of the perturbations caused by a smooth composition gradient (see Fig. A1). However, the term in the square brackets, which we compute below, is significantly smaller than 1 in the capture layers.

Using the chain rule as in equation (A7), and using equation (A8), we find that

$$\left.\frac{\partial \ln \rho}{\partial \ln T}\right|_\mathrm{p} = -\frac{\Gamma_{\mu_\mathrm{e}}}{\Gamma_\rho} \left.\frac{\partial \ln \mu_\mathrm{e}}{\partial \ln T}\right|_\mathrm{p}. \tag{A10}$$

We can now evaluate the pre-factor of the source term by switching independent variables from (ρ, T) to (p, T) to obtain

$$\left.\frac{\partial \ln p}{\partial \ln T}\right|_\rho = \Gamma_{\mu_\mathrm{e}} \left.\frac{\partial \ln \mu_\mathrm{e}}{\partial \ln T}\right|_\mathrm{p} \left[1 - \Gamma_{\mu_\mathrm{e}} \left.\frac{\partial \ln \mu_\mathrm{e}}{\partial \ln p}\right|_T\right]^{-1}. \tag{A11}$$

equations (A9) and (A11) allow us to evaluate both the source term ΔS and the index Γ (see equation 46), if we can find the partial derivatives of $\mu_\mathrm{e}(p, T)$ with respect to p and T. We now describe how to find these derivatives.

While constructing an equilibrium stellar model, we computed the dependence of μ_e on r for each capture layer. However, at least in principle, we could compute $\mu_\mathrm{e}(p, T)$ using the following approach. We combine the rate equation (17) and the equation of hydrostatic balance (18) to obtain

$$\frac{\mathrm{d}\ln X_1}{\mathrm{d}\ln p} = -\frac{p}{\dot{m} g} R_\mathrm{ec}(p, X, T), \tag{A12}$$

where $\dot{m} = \dot{M}/4\pi r^2$ is the local accretion rate. Approximating r^2 and g as constant over the capture region, we then solve equation (A12) to obtain $X_1(p, T)$, which, from equation (15), immediately gives us[10] $\mu_\mathrm{e}(p, T)$. Equation (A12) was derived assuming that the NS is in hydrostatic balance, but we shall use it to determine $\mu_\mathrm{e}(p, T)$ even in the perturbed star. This is consistent, because corrections to $\mu_\mathrm{e}(p, T)$ are due to the non-spherical perturbation itself, and so would enter our perturbation equations (43) only as higher order corrections.

In practice, rather than to first compute $\mu_\mathrm{e}(p, T)$ and then differentiate it, it is much more convenient to use a simple approximation to evaluate the derivatives of μ_e. This approximation is essentially the same as the one used to evaluate the source term in the case of Δz_d perturbations, equation (A6). We presume that the shape of the capture layer does not change as we perturb the local temperature by δT, but only its location shifts. Mathematically speaking, we write $\mu_\mathrm{e}(p, T) \approx \tilde{\mu}_\mathrm{e}[p - p_\mathrm{c}(T)]$, where p_c is the (temperature-dependent) pressure at the 'centre' of the capture region, which we define more precisely below. We use the tilde on $\tilde{\mu}_\mathrm{e}$ to distinguish this 'approximate version' from the actual function μ_e.

With this approximation,

$$\left.\frac{\partial \ln \mu_\mathrm{e}}{\partial \ln p}\right|_T = \frac{\mathrm{d}\ln \tilde{\mu}_\mathrm{e}}{\mathrm{d}\ln p} = -\frac{1}{\tilde{V}} \frac{\mathrm{d}\ln \mu_\mathrm{e}}{\mathrm{d}\ln r}, \tag{A13}$$

[10] To be more precise, μ_e is a function of p and a functional of T, since it depends not just on the T at the point but on T in the whole capture region. However, Bildsten & Cumming (1998) showed, and we confirm for the case of deep capture layers that include free neutrons, that the variation in T over the capture region is quite small. Thus we treat $T(r)$ as constant over the capture region, in which case there is no practical distinction between a function and a functional.

Downloaded from https://academic.oup.com/mnras/article-abstract/319/3/902/1075833 by California Institute of Technology user on 19 May 2020

Table A1. List of variables.

Name	Description	Section
$\dot{M}$	Mass accretion rate	1
$\nu_{\rm s}$	Spin frequency	1
B	Magnetic field	1
Q_{22}	Mass quadrupole moment	1
$\dot{M}_{\rm Edd}$	Eddington accretion rate	1
$N_{\rm a}$	Accretion torque	1.1
$\delta\rho$	Eulerian density perturbation	1.1
Q_{lm}	Mass multipole moment	1.1
$\nu_{\rm gw}$	Gravitational wave frequency	1.1
$N_{\rm gw}$	Gravitational wave torque	1.1
M	NS mass	1.1
R	NS radius	1.1
$Q_{\rm eq}$	Mass quadrupole moment needed for equilibrium between accretion and GW emission	1.1
$M_{1.4}$	NS mass in units of $1.4\,{\rm M}_\odot$	1.1
R_6	NS radius in units of 10 km	1.1
$\boldsymbol{I}_{ab}$	Mass quadrupole tensor	1.1
Ω	Spin frequency	1.1
$\bar{\sigma}$	Average shear strain	1.1
$\nu_{\rm s,eq}$	Equilibrium spin frequency	1.1
d	Source distance	1.1
$\dot{E}_{\rm gw}$	Energy loss due to GWs	1.1
$h_{\rm a}$	GW strain	1.1
$F_{\rm x}$	X-ray flux	1.1
A	Nuclear mass number	1.2
Z	Nuclear charge	1.2
δT	Lateral temperature perturbation	1.2
$\Delta z_{\rm d}$	Vertical shift of a capture layer	1.2
$\Delta\rho$	Lagrangian density perturbation	1.2
Υ	Sensitivity of e^- capture layer location to temperature	1.2
μ	Shear modulus	1.2
$k_{\rm B}$	Boltzmann constant	1.2
$\rho_{\rm nd}$	Neutron drip density	2
K	Conductivity	2
$t_{\rm comp}$	Compression time-scale	2.1
$\dot{m}$	Local accretion rate	2.1
g	Local gravitational acceleration	2.1
e	Electron charge	2.1
$m_{\rm b}$	Baryon mass	2.1
$E_{\rm F}$	Electron Fermi energy	2.1
Q	e^- capture threshold energy	2.1
ft	ft value	2.1
$R_{\rm ec}$	e^- capture rate	2.1
h	Scale height	2.1
$t_{\rm ec}$	e^- capture time-scale	2.1
X_1	Mass fraction of the e^- capture element	2.2
X_2	Mass fraction of the e^- capture product	2.2
$X_{\rm n}$	Mass fraction of free neutrons	2.2
$n_{\rm e}$	Density of electrons	2.2
$\mu_{\rm e}$	Electron mean molecular weight	2.2
$\boldsymbol{v}$	Compression flow speed	2.2
$\Delta E_{\rm F}$	Thickness of a capture layer	2.2
r	Radius	2.2
$p_{\rm e}$	Electron pressure	2.3
ρ_{11}	Density in units of $10^{11}\,{\rm g\,cm^{-3}}$	2.3
$n_{\rm n}$	Free neutron density	2.3
M_r	Mass enclosed within radius r	2.3
a	Internuclear spacing	2.3
$\Gamma_{\rm coul}$	Coulomb energy density relative to $k_{\rm B}T$	2.3
$\boldsymbol{F}$	Heat flux	2.4
F_r	Radial component of the heat flux	2.4
$\epsilon_{\rm nuc}$	Energy generation rate	2.4
ϵ_ν	Urca neutrino emissivity	2.4
ϵ	Energy gain/loss rate per gram	2.4
$E_{\rm nuc}$	Total energy released in a capture layer	2.4
Δ	Superfluid gap energy	2.4
$\rho_{\rm nuc}$	Nuclear density	2.4
$L_{\rm core}$	Energy lost from the NS core	2.4
$T_{\rm burn}$	H/He burning temperature	2.4
$f_{\rm nuc}$	Asymmetry in the nuclear energy release	3.1

Table A1 – *continued*

Name	Description	Section
$\delta E_{\rm nuc}$	Difference in total energy released in a capture layer	3.1
$n_{\rm k}$	Temperature sensitivity of the conductivity	3.1
$n_{\rm e}$	Temperature sensitivity of the neutrino emissivity	3.1
$f_{\rm comp}$	Asymmetry in conductivity	3.1
$\delta(Z^2/A)$	Difference in charge-to-mass ratio	3.1
δF^a	Flux perturbation	3.2
$\hat{r}^a$	Unit radial vector	3.2
∇^a	Derivative operator	3.2
$K_{\rm core}$	Conductivity of the core	3.2
$K_{\rm crust}$	Conductivity of the crust	3.2
$\delta F_{\rm r,core}$	Radial flux perturbation in the core	3.2
$\delta F_{\perp,\rm core}$	Transverse flux perturbation in the core	3.2
ΔR	Crust thickness	3.2
$F_{\rm A}$	Accretion flux	3.3
f	Composition or nuclear heating perturbation	3.3
$t_{\rm th}$	Thermal time	3.3
ξ^a	Displacement vector	4
$Q_{lm}^{\rm hist}$	'Historical' multipole moment	4
$Q_{lm}^{\rm pert}$	Multipole moment due to the 'current' perturbation	4
$\Delta\mu_{\rm e}$	Smooth composition gradient	4
$\boldsymbol{\tau}_{ab}$	Stress tensor	4.1
$\boldsymbol{g}_{ab}$	Metric tensor	4.1
ξ_r	Radial component of the displacement	4.1
$\xi_\perp$	Transverse component of the displacement	4.1
Φ	Gravitational potential	4.1
β	$\sqrt{l(l+1)}$	4.1
τ_{rr}, $\tau_{r\perp}$	Components of the stress tensor	4.1
$\boldsymbol{e}_{ab}$, $\boldsymbol{f}_{ab}$, $\boldsymbol{\Lambda}_{ab}$	Angular tensors	4.1
$z_1 - z_4$	Eigenfunctions of the elastic perturbation equations	4.1
$\alpha_1 - \alpha_4$	Coefficients of the elastic perturbation equations	4.1
Γ	Compressibility	4.1
ΔS	Source term	4.1
$\tilde{U}$, $\tilde{V}$	Polytrope variables	4.1
$r_{\rm top}$, $r_{\rm bot}$	Top and bottom of the crust	4.2
$\rho_{\rm s}$,$\rho_{\rm l}$	Densities of the solid and of the liquid at the crust–core boundary	4.2
$Q_{22}^{\rm pp}$	Plane-parallel approximation to the quadupole moment	4.2
$\bar{\sigma}_{\rm max}$	Breaking strain of the crust	6
$\boldsymbol{t}_{ab}$	Stress tensor (non-linear)	6.2
t_{rr}, $t_{r\perp}$, t_Λ	Components of $\boldsymbol{t}_{ab}$	6.2
$\boldsymbol{\sigma}_{ab}$	Strain tensor	6.3
$\bar{\sigma}$	Average strain	6.3
σ_{rr}, $\sigma_{r\perp}$, σ_Λ	Components of $\boldsymbol{\sigma}_{ab}$	6.3
$p_{\rm b}$	Pressure at the bottom of the crust	6.3
$\rho_{\rm b}$	Density at the bottom of the crust	6.3
$\langle\mu/p\rangle$	Average shear modulus	6.3
$\sigma_{ab}^{\rm eff}$	Effective strain	6.3
$I_{\rm crust}$	Moment of inertia of the crust	6.5
$I_{\rm NS}$	Moment of inertia of the neutron star	6.5
$\delta\Phi$	Gravitational potential perturbation	6.5
$\mathcal{F}$	Correction due to the neglect of self-gravity	6.5
J^a	Angular momentum vector	7
z^a	Direction of the rotation axis	7
n^a	Pricipal axis direction	7
$\theta_{\rm w}$	Wobble angle	7
$\boldsymbol{I}^{ab}$	NS inertia tensor	7
I_0	Spherically symmetric part of I^{ab}	7
ΔI_Ω	Oblate part of I^{ab}, for crust whose unstressed state is spherical	7
$\Delta I_\Omega + \Delta I_{\rm d}$	Oblate part of I^{ab}, for a fully relaxed crust	7
Q_{21}	$m = 1$ mass quadrupole moment	7
$\omega_{\rm p}$	Precession frequency	7
$\omega_{\rm gw}$	GW angular frequency	7
$L_{\rm gw}^{\rm wobble}$	GW luminosity due to the wobble	7
$p_{\rm c}(T)$	Pressure at the centre of the capture layer	A
$\bar{\mu}_{\rm e}$	Run of $\mu_{\rm e}$ with radius	A
Γ_ρ	Logarithmic index of pressure with density	A
$\Gamma_{\mu_{\rm e}}$	Logarithmic index of pressure with electron mean molecular weight	A

Downloaded from https://academic.oup.com/mnras/article-abstract/319/3/902/1075833 by California Institute of Technology user on 19 May 2020

where $\mu_e(r)$ is just the run of μ_e in the background model (see Fig. A2). $\tilde{V}$ is defined in equation (44) and is equal to r/h, where h is the local pressure scaleheight. In the crust $h/r \lesssim 0.1$ ($\ll 0.1$ in the outer crust). It is then evident from Fig. A2 that the term in square brackets in equation (A9) is indeed much smaller than 1 inside capture layers.

Similarly, we have

$$\left.\frac{\partial \ln \mu_e}{\partial \ln T}\right|_p = -\frac{d\ln \tilde{\mu}_e}{d\ln p}\frac{d\ln p_c}{d\ln T} = \frac{1}{\tilde{V}}\frac{d\ln \mu_e}{d\ln r}\frac{d\ln p_c}{d\ln T}. \quad \text{(A14)}$$

In the above equation, p_c is a function of T for a given capture region, and is not a function r or p.

Equation (A12) exhibits the competition between the local compression time-scale $t_{comp} = p/\dot{m}g$ and the electron capture time-scale $t_{ec} = 1/R_{ec}$. Most electron captures happen when $t_{comp} \sim t_{ec}$. We use this to *define* the centre of the capture layer, p_c:

$$\frac{p_c}{\dot{m}g} R_{ec}(E_F(p_c), T) \equiv 1. \quad \text{(A15)}$$

Differentiating the above equation with respect to T and using the capture rate (11) we find

$$\frac{d\ln p_c}{d\ln T} = \left(\frac{E_F - Q}{k_B T} - 3\right)\left[1 + \frac{E_F}{k_B T}\frac{d\ln E_F}{d\ln p}\right]^{-1}\Bigg|_{p=p_c}. \quad \text{(A16)}$$

All the terms on the right-hand side of the above equation are evaluated at $p = p_c$. To find p_c, we would have to solve the transcendental equation (A15). However, we note that the above expression enters in equation (A14) multiplied by $d\ln\mu_e/d\ln r$, which is a sharply peaked function of r. Thus we can treat the right-hand side of (A16) as a function of r and let the delta-function like shape of $d\ln\mu_e/d\ln r$ pick out the correct value of $p \approx p_c$.

Finally, to evaluate equation (A16), we need

$$\frac{d\ln E_F}{d\ln p} = \frac{1}{3}\left[\frac{1}{\Gamma_\rho} + \frac{1}{\tilde{V}}\left(\frac{\Gamma_{\mu_e}}{\Gamma_\rho} + 1\right)\frac{d\ln \mu_e}{d\ln r}\right], \quad \text{(A17)}$$

which follows from $E_F \propto (\rho/\mu_e)^{1/3}$ and a modest amount of algebra. We can now evaluate both Γ and the source term ΔS using the properties of the background model: use equations (A9) and (A13) to compute Γ, and equations (46), (A11), (A13), (A14) and (A16), as well as the local δT, to compute ΔS. The source term ΔS is plotted in the bottom panels of Figs 10–12.

Using equation (A16) we can establish a precise relation between the vertical shift Δz_d of the 'centre' of the e^- capture layer (in absence of elastic readjustment) and the local temperature perturbation δT,

$$\frac{\Delta z_d}{r} = -\frac{1}{\tilde{V}}\frac{d\ln p_c}{d\ln T}\frac{\delta T}{T}. \quad \text{(A18)}$$

This relation is plotted in the bottom panel of Fig. 3 in Section 2.1. Similarly, the change in electron Fermi energy at which most captures occur in response to a local temperature perturbation is just

$$\Delta E_F = \frac{d\ln p_c}{d\ln T}\frac{d\ln E_F}{d\ln p}\frac{E_F}{k_B T} k_B \delta T, \quad \text{(A19)}$$

or $\Delta E_F = -\Upsilon(k_B \delta T)$, where

$$\Upsilon = -\frac{d\ln p_c}{d\ln T}\frac{d\ln E_F}{d\ln p}\frac{E_F}{k_B T}. \quad \text{(A20)}$$

The function Υ is plotted in the top panel of Fig. 3 in Section 2.1. The complicated dependence of Δz_d and Υ on the capture layer depth stems from the differences in the number of electrons captured and number of neutrons emitted in each capture layer.

This paper has been typeset from a TEX/LATEX file prepared by the author.

Downloaded from https://academic.oup.com/mnras/article-abstract/319/3/902/1075833 by California Institute of Technology user on 19 May 2020